Study on the Thermodynamics of Protein Aggregation

蛋白質凝集の熱力学に関する研究

A Doctoral Thesis

by

Tatsuya Ikenoue

Submitted to the Graduate School of Science

Osaka University

February, 2016

Acknowledgement

This work is a result of many wonderful circumstances of the Institute for Protein Research, Osaka University. There are people whom I am indebted to their precious contributions and supports throughout my graduate school career. Especially, the role of several people who mentored me was key in obtaining the goal, which now is embodied in the volume of this writing.

This work has been performed under the direction of Professor Yuji Goto (Osaka University). I would like to express sincere gratitude to his guidance, discussion and advice. My deepest appreciation goes to Associate Professors Young-Ho Lee (Osaka University) whose supports, proper advices and discussion for various things have helped me very much throughout my study. I am deeply indebted to Assistant Professor Hisashi Yagi (Tottori University), Associate Professor Kazumasa Sakurai (Kinki University), and Assistant Professor Masatomo So (Osaka University) for the support and helpful advice. I would also thank Associate Professor József Kardos (Eötvös Loránd University, Budapest) for their valuable advice and experimental supports, and Professor Yasushi Kawata (Tottori University) for providing precious peptides. This work was supported by the members of the Laboratory of Protein Folding, Institute for Protein Research, Osaka University. I am deeply grateful for Dr. Yuichi Yoshimura for giving helpful advice, Dr. Mayu Suzuki for telling me about lipid membrane and its importance, and Ms. Kyoko Kigawa for the assistance of protein expression and purification.

I also acknowledge for foundation and financial support from The Research Fellowships of Japan Society for Promotion of Science for Young Scientist, and financial support from SUNBOR SCHOLARSHIP of SUNTORY Foundation for Life Science, and foundation of Project MEET (Medical Evolution Expedited Tackle) from Osaka University and Mitsubishi Tanabe Pharma Corporation.

Finally, I would like to my deepest thanks to my loving people, my family and friends, as well as God for their endless spiritual support.

池之上 達哉

Tatsuya IKENOUE

February, 2013

Table of contents

Acknowledgements……iii

Abbreviations……vii

Chapter 1. General introduction

Amyloid fibrils and its association with protein misfolding diseases……2

Amyloidogenic proteins and peptides used in this work……3

Protein aggregation escaped from protein homeostasis……5

Formation of amyloid fibrils and their structural property……6

Supersaturation and protein aggregation……8

Thermodynamics of globular protein……9

Heat and cold denaturation of globular proteins……10

Chemical denaturation……11

Calorimetry of the protein……11

Computational approach……12

Thermodynamics of amyloid fibrils……12

Chapter 2. Cold denaturation of α-synuclein amyloid fibrils

2-1. Introduction……16

2-2. Materials and Methods……18

2-3. Results

Cold Denaturation of αSN Fibrils of at 0 °C and pH 7.5……21

Two-Step Denaturation of αSN Fibrils via a Kinetic Intermediate……21

Factors Affecting the Cold Denaturation of αSN Fibrils……23

Reversible Cold Denaturation of αSN Fibrils……23

Heat Denaturation of αSN Fibrils and Their Reversibility……...……..…..…26

Stability of the Amyloid Fibrils of Various Proteins in a Wide Temperature Range and

Gdn-HCl-Assisted Cold Denaturation……..……...…27

Opposite Signs of Thermodynamic Parameters for αSN Fibrils to Those of Other Proteins……...31

2-4. Discussion……...….33

2-5. Supporting Information

Supplemental Experimental Procedures……..……....……37

Supplemental Figures……..……....……45

Supplemental Tables…….…….……48

Chapter 3. Heat of supersaturation-limited amyloid burst directly monitored by isothermal titration calorimetry

3-1. Introduction……..…….……..54

3-2. Materials and Methods……...……..……56

3-3. Results

Heat for the Formation of Amyloid Fibrils Monitored by ITC..……..……..……57

Small Amyloid Burst and Excess Heat Immediately after Salt-Titration.……..……..…..……61

Heat of Amorphous Aggregation…….…..……..……..……..64

Temperature Dependency of Aggregation Heat.……..……..…….65

Evaluation of Thermodynamic Parameters……..……...……67

3-4. Discussion……..……..…….70

3-5. Supporting Information

Supplemental Experimental Procedures……..……73

Supplemental Figures……..……75

Supplemental Tables……..……78

Chapter 4. General conclusion……..……..……81

References……..……..……84

List of Publications…….……..……94

Abbreviations

Aβ	amyloid β
αSN	α-synuclein
β2m	β2-microglobulin
ThT	thioflavin-T
JC-1	5,5',6,6'-tetrachloro-1,1',3,3'-tetraethyl-benzimidazolylcarbocyanine iodide
CD	circular dichroism
AFM	atomic force microscopy
NMR	nuclear magnetic resonance
E. Coli	*Escherichia coli*
Gdn-HCl	guanidine hydrochloride
ITC	isothermal titration calorimetry
DSC	differential scanning calorimetry
ΔG	Gibbs free energy change
ΔH	enthalpy change
ΔS	entropy change
T_m	temperature of denaturation midpoint
C_m	Gdn-HCl concentration of denaturation midpoint
ΔK_{eq}	equilibrium constant
ΔC_p	heat capacity change under constant pressure
K_D	dissociation constant
MD	molecular dynamics
NAC	non-amyloid-β component

Chapter 1. General introduction

Amyloid fibrils and its association with protein misfolding diseases

In recent year, remarkable progress of science has dramatically increased human longevity. Advances in the diagnosis and treatment of human disease reduce the burden of human diseases, and average life in many countries have risen to over 80 years. In aging society, as a result of life expectancy, we have confronted with incurable diseases which require a great deal of effort to conduct treatment. Most serious diseases in aging society, such as Alzheimer's, Parkinson's, and diabetes, are deeply associated with amyloid fibrils which are aberrant fibrous aggregates of protein. Diameters of typical mature amyloid fibrils are ~10 nm and their lengths is in the order of microns. Protein aggregation including amyloid fibrillation mainly caused by protein misfolding, and amyloid fibrillation has shown toxicity to nerve cells and cause the neurodegenerative diseases. Up to now, it is reported that amyloid fibrillation is responsible for more than 50 diseases (1) (Table 1). These misfolding-induced diseases are major threats to human health and welfare. It has been estimated that 46.8 million people in the world are living with Alzheimer's disease in 2015, and this number will double every year reaching 131.5 million in 2050 (2). There is currently no effective therapies to combat these misfolding diseases and also no reliable diagnostics in early stage of a disease, although many models of disease biomarkers to track pathophysiological processes were proposed (3).

Disease	Aggregation protein and peptide
Alzheimer's disease	Amyloid β
Spongiform encephalopathies	Prion protein or its fragments
Parkinson's disease	α-synuclein
Huntington disease	Huntingtin fragment
Familial amyloidotic polyneuropathy Senile systematic amyloidosis	Transthyretin
Haemodialysis-related amyloidosis	β_2-microglobulin
Type II diabetes	Amylin (IAPP)

Table 1. Some human diseases associated with amyloid fibril formation.

Amyloidogenic proteins and peptides used in this work

Amyloid β

Amyloid β-protein is the proteolytic product of amyloid β-protein precursor and it contains 39–43 amino acid residues (Fig. 1). Among them, amyloid β-protein 1-42 and 1-40 ($A\beta_{1-42}$ and $A\beta_{1-40}$) is considered to be the most vital factor to the onset of Alzheimer's disease (AD) due to its strong neurotoxicity and aggregation capability (4-6). Although the conformation of $A\beta_{1-42}$ is variable and uncertain (7, 8), the secondary structure of Aβ monomers in fibrils is determined by NMR spectroscopy (9, 10). $A\beta_{1-42}$ monomers in fibrils possesses a disordered hydrophilic N-terminal region (Asp1–Lys16) (11), which is also considered to be the minimal zinc-binding domain and contains two aspartates subject to protein aging, a hydrophobic β-sheet-forming region (Leu17–Ser26), a turn region (Asn27–Ala30), and another β-sheet-forming region (Ile31–Ala42) (9, 10). Based on these information, numerous studies have suggested various inhibitors of Aβ-aggregation and their inhibiting mechanisms (12, 13).

```
          10        20        30        40
DAEFR HDSGW EVHHQ KLVFF AEDVG SNKGA IIGLM VGGVV IA
```

Fig 1. The amino acid sequence of Aβ

α-synuclein

α-synuclein (αSN) is a 14.5 kDa protein expressed predominantly at the presynaptic terminals of brain neurons. The physiological function of the protein remains unknown although a role in synaptic vesicle recycling has been suggested (14). Misfolding of αSN leads to the formation of fibrillar cytoplasmic aggregates called Lewy bodies, which are a defining characteristic of Parkinson's disease (15, 16). Because the number of Lewy bodies is often poorly correlated with the severity of symptoms, controversy surrounds the issue of whether fibrils or smaller soluble oligomers are responsible for the neurotoxicity of misfolded αSN. Regardless of the mechanism of neurotoxicity, genetic evidence establishes a link between the αSN gene and Parkinson's disease. Although 90–95% cases of Parkinson's disease cases are sporadic (17), the autosomal-dominant familial mutations A30P, E46K, A53T, as well as the triplication of the wild-type αSN gene lead to early onset of the disease (18).

The amino acid sequence of αSN can be subdivided into three domains with unusual distributions

of charged residues (Fig. 2). The first 90 residues of αSN contain seven imperfect repeats of the amino acid sequence KTKEGV (19), which are important for the induction of α-helical structures in αSN and for binding to membranes containing negatively charged lipids that the protein prefers (20, 21). Residues 61-95 of αSN correspond to the hydrophobic "non-amyloid-β component" (NAC), the most aggregation-prone part of the protein. The name NAC, derives from the occurrence of this segment as a second protein component of the extracellular amyloid-β plaques found in patients with Alzheimer's disease. The mechanism by which the NAC fragment of the intracellular αSN is cleaved and comes to be associated with extracellular amyloid-β plaques is unknown. The last two KTKEGV repeats are in the NAC segment, however, due to their imperfect nature only two charged residues Lys80 and Glu83 occur in the hydrophobic region between residues 62 and 95. The last 40 amino acids of αSN contain 15 acidic residues, giving the C-terminal tail of the protein a negatively charged character at physiological pH.

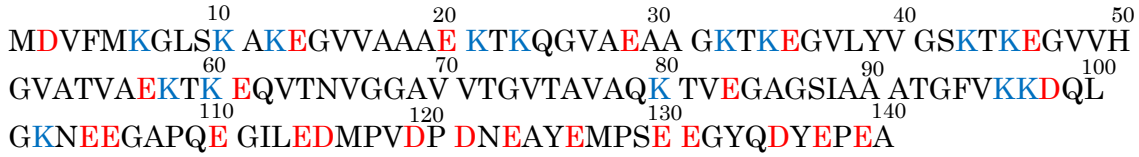

Fig. 2. The amino acid sequence of αSN

β₂-microglobulin and K3 peptide

Dialysis-related amyloidosis is a common and serious complication among patients on long term hemodialysis, in which β_2-microglobulin (β2m) forms amyloid fibrils. Native β2m, made of 99 amino acid residues, corresponds to a typical immunoglobulin domain (Fig. 3) and is a component of the type I major histocompatibility antigen. Although the increase in the concentration of β2m in blood over a long period is the most critical risk factor causing amyloidosis, the molecular details remain unknown. Recently β2m, because of its relatively small size, which makes it suitable for physicochemical studies, has been used as a target for extensive studies addressing the mechanism of amyloid fibril formation in the context of protein conformation (22-24).

In many amyloidogenic proteins, short peptides, called minimal or essential sequences, can form

amyloid fibrils by themselves. Kozhukh *et al.* previously found that a 22-residue K3 peptide, Ser20–Lys41, obtained by digestion of β2m with *Acromobacter* protease I, forms amyloid fibrils (25). The minimal sequence provides various pieces of information useful for addressing amyloid fibril formation. It is likely that the minimal sequence includes the initiation site for amyloid fibril formation of the whole molecule.

Fig. 3. The amino acid sequence of β2m

Protein folding and protein aggregation escaped from protein homeostasis

Proteins usually fold into compact three dimensional structures which play important role in intrinsic function of proteins in the living cell (i.e. gain of function) (Fig. 4). In microscopic aspects, the conformation of proteins have flexibility and can adapt their structures ranging from compact native states to largely unfolded states. During the process of folding or process of structural changes, protein molecules occasionally fail to fold into native structure and misfold. Furthermore, these misfolded proteins often form aggregates in intra- and/or extracellular space, thereby abolishing protein function (i.e. loss of function) (Fig. 4). Deposition of these aggregates in cells and tissues eventually result in serious diseases (i.e. gain of toxic function). In order to counteract protein misfolding and aggregation, cells possess various protective mechanisms to maintain protein homeostasis, which is the ability of cells to regulate the levels of proteins by means of the concentration, conformations and interactions (26-31). Once protein homeostasis becomes impaired due to environmental stress, aging, or the system escaped from protective mechanism of homeostasis, protein molecules misfold and form aberrant aggregates in living cells.

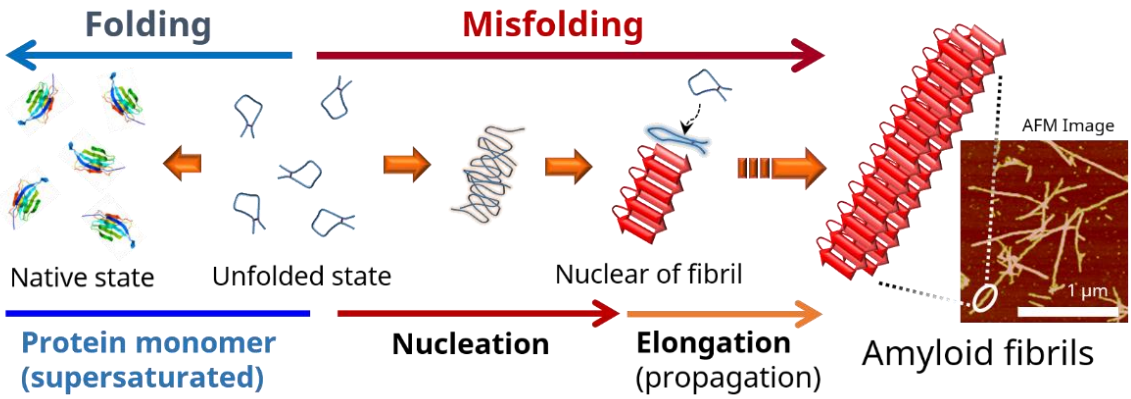

Fig. 4. Brief description of protein folding and misfolding. Protein usually fold into compact three dimensional structure which play important role in the living cell, but protein molecules occasionally fail to fold into native state and form aberrant aggregation. The typical fibril formation process has two steps consisting of nucleation step with a long lag time, and followed by a rapid elongation step that is analogous to crystallization of substances. Amyloid fibrils are formed in supersaturated monomer solutions. Once supersaturation state of protein is broken, proteins immediately form aggregates.

Formation of amyloid fibrils and the structural property

Protein homeostasis also serves as maintenance of the protein solubility which is a key to protein aggregation. Proteins can be soluble even beyond the limit of solubility due to the supersaturation in the cell. When the supersaturated state of protein is disrupted, insoluble aggregates form (i.e. salting out). Insoluble protein aggregates have shown various morphologies, ranging from three dimensional ordered crystals to disordered amorphous aggregation and different nature of the aggregation pathway. Amyloid fibrils have ordered structures which are distinguished from three dimensional crystals and amorphous aggregates because of their unique conformational properties. Amyloid fibrils are linear assemblies of proteins which are categorized to one dimensional crystals.

Generally, amyloid fibrils in living system deposit over long periods of time. In the case of globular proteins, amyloid fibrils can be prepared by manipulating conditions that destabilize the native state to completely or partially unfolded state, such as using extreme pH (23, 32), high temperature, and chemical denaturants such as urea, guanidine hydrochloride (Gdn-HCl). Accessing hydrophobic residues into solvent caused by unfolding or partially unfolding dramatically increase propensity to assemble each other and consequently forms aggregation (33, 34). A more efficient method of preparing

fibrils is adding fibril nuclei as seeds of fibril growth to eliminate a nucleation phase which has long lag time (35).

On the other hand, many intrinsically disordered proteins or peptides that are known to be involved in the most common misfolding diseases, such as amyloid-β peptide in Alzheimer's disease (36), α-synuclein in Parkinson's disease (15), and amylin in type II diabetes (37), are also prone to aggregate in physiological condition although many of them tend to maintain the high level of solubility through the highly abundant charged and polar residues. Dynamic fluctuations may enable to access partially folded states and these states are particularly prone to aggregate (38). In the living system, partially folded states may be required for functional reasons (39, 40).

Protein aggregation, however, has often been an obstacle to studying the structure, function, and physical properties of proteins because of their too large size to apply spectroscopy although elucidating their structure is very important to understand the mechanism and develop strategies to conduct treatment of misfolding diseases. Furthermore, polymorphism of amyloid fibrils of various proteins has been reported and, unfortunately, these heterogenic properties often disturb precise and accurate evaluation of biological and biophysical natures of amyloid fibrils. Although polymorphic formation of amyloid fibrils is likely to be controlled by the solution condition such as pH, temperature, and cosolvent, preparing homogeneous fibrils are not virtually easy because of similar physicochemical and mechanical stability of amyloid fibrils. The maturation process of amyloid fibrils from kinetic to thermodynamic controls may be present and key for the polymorphic property of amyloid fibrils.

Interestingly, using dipeptides, multi-step phase transition process underlying supramolecular assembly was recently observed (41). The real-time observation showed that early formed spherical amorphous aggregates converted step by step to more ordered structures over time; first step is conversion to fibrils and finally converted into a thermodynamically most stable form of crystal-like tube. This behavior is analogous to Ostwald's ripening, which is a kinetically driven self-assembly process; conversion from less structured states to more structured states through the internal rearrangement and recrystallization of structures (42-44). Importantly, similar behavior of this phase transition has been also observed in the living cells (45-48).

In spite of these difficulties on structural study, great efforts allow us to know characteristics of

structures of protein aggregates at the level of atoms and molecules (see *Chapter 2. Table S4* for example). Many structural studies have revealed that amyloid fibrils are consist of cross-β structural motifs, in which individual β-strands lie perpendicular to the fibril axis with the β-sheets stacked in the parallel direction to produce protofilaments (49, 50). The protofilaments associate laterally and form amyloid fibrils with hierarchical structures. Because of the main chain dominant structure mainly constructed by a number of hydrogen-bond and the hydrophobic effect between monomers, amyloid fibrils exhibit high stability against outer stress and they are considered to show lower free energy states than those of natively folded state (51, 52). Although the study on thermodynamics of amyloid fibrils is essential for various scientific field including protein science, biophysics, and medical science, our understanding of the detailed thermodynamics of amyloid fibrillation is still unclear and very limited information is available. Thermodynamic features of protein aggregation and structural aspects are also very important from therapeutic perspective as these properties are physiologically and medically key for disaggregation and clearance of aggregates *in vivo*.

Supersaturation and protein aggregation

Solubility and supersaturation are the most important thermodynamic factors in protein aggregation. Supersaturation is a mixed concept of thermodynamics with kinetics and its detailed mechanism on protein aggregation still remains unclear. Although the metastability of supersaturation should be also considered, when the degree of supersaturation elevated by increasing protein concentrations or decreasing the solubility, the driving force of aggregation seems to be stronger which may be linked to shortening of a lag time and increased an elongation rate. Careful experimental kinetic studies improved our understanding on how amyloid fibrils are formed based on the theory and formalism of chemical kinetics (53, 54). Accordingly, it is highly useful to address the supersaturated state by using the two subconcepts: one is the degree of supersaturation and the other is the metastability of supersaturation.

The degree of supersaturation (σ) continues to increase with elevations in protein concentrations and is predictable based on its definition; $\sigma = (c - c_{eq}) / c_{eq}$, where c is the protein concentration given and c_{eq} is the critical concentration of proteins. On the other hand, the metastability of supersaturation for productive nucleation, which corresponds to a kinetic energy barrier, is maximal just above the

solubility limit and decreases with higher protein concentrations. The higher metastability of supersaturation with a low degree of supersaturation maintains kinetically-trapped soluble states, while the lower metastability with a high degree of supersaturation leads to amorphous aggregation including partially structured aggregates. Since much higher protein concentration produces only amorphous aggregates although it is easy to form protein aggregates, the probability of productive nucleation is maximal at a balanced metastability and degree of supersaturation. Therefore, both degree and metastability of supersaturation play a key role in determining the pathway of protein aggregation. It should be noted that the interplay between kinetics and thermodynamics involved in supersaturation determines the behaviors of protein aggregation. At concentration in living cell, the native state of protein may not always show global free energy minima, in other words, soluble native protein is in a metastable state that is separated from solid amyloid fibril state by high kinetic barriers.

Thermodynamics of globular protein

The free energy landscape of protein folding and misfolding is still important to provide insight into the conformational properties with a direct indicator of the reaction coordinate. Thus, the free energy landscape of a proteins offers the possibility of describing molecular behavior, conformational stability, and the mechanism of protein misfolding and aggregation. Therefore it provides the tool for rational therapeutic strategies. This free energy depends on the enthalpy-entropy interplay, $\Delta G = \Delta H - T\Delta S$, where ΔG is the change in Gibbs free energy and the change in enthalpy and entropy are represented by ΔH and ΔS, respectively. It is widely invoked as a descriptive principle in thermodynamic analyses of protein folding and intermolecular interaction. It is already well known that enthalpic components provide insights into molecular and atomic interactions such as hydrogen bonding and van der Waals interactions, whereas entropic components reveal the degree of freedom of molecules such as conformational flexibility of the polypeptide chain and translational freedom of water molecules in surrounding environments of protein surfaces which cause hydrophobic interactions of proteins. It should be noted that water which surrounds protein surface becomes free on protein folding or protein interactions with other molecules.

A number of thermodynamic studies on protein folding have been extensively performed and well

established. The typical way is to access the thermodynamics of protein folding using the two-state transition model between unfolded and folded states. Based on this model, the conformational stability of folded proteins has been widely investigated by denaturation experiments through adding chemical denaturants (55-58) and changing pH (55, 59), temperature (60-63), and pressure (64-67).The various spectroscopy including fluorescence, circular dichroism (CD), Fourier transform infrared spectroscopy (FTIR), and nuclear magnetic resonance (NMR) and calorimetry such as differential scanning calorimetry (DSC) has been used for monitoring structural changes of folded states.

Heat and cold denaturation of globular proteins

Thermal denaturation of globular proteins is known as a conventional way to evaluate the conformational stability. As temperature in protein solution increased, most soluble proteins denature below the boiling point due to increases in conformational entropy (i.e., heat denaturation). Assuming the two-state unfolding model, temperature of denaturation midpoint T_m where both folded and unfolded protein are equally populated at equilibrium is obtained from thermal assay with structural analysis such as CD spectrometry. At the denaturation midpoint, the equilibrium constant ΔK_{eq} is equal to one ($\Delta K_{eq} = 1$) which produces ΔG of zero ($\Delta G = 0$) based on the relation of $\Delta G = -RT\ln K_{eq}$. It is also possible that the analysis based on the van't Hoff equation, $\frac{d \ln K_{eq}}{d(1/T)} = -\frac{\Delta H_{vHoff}}{R}$, provides a series of thermodynamic parameters of unfolding of globular proteins.

It is also well known that all proteins undergo cold-induced denaturation and cold and heat denaturation of proteins are predicted using the Gibbs-Helmolz equation. Although the molecular mechanism of cold denaturation is still in debates, cold denaturation can be explained by a thermodynamic aspect of water, that is, the temperature dependence of the hydration of nonpolar residues (68). On the other hand, there is only limited information on conformational stability of protein aggregates including amyloid fibrils over a wide temperature range. Therefore, I came up with heat and cold denaturation of amyloid fibrils in chapter 2.

Chemical denaturation

Chemical denaturation of folded proteins with chaotrope-like compounds such as urea and guanidine hydrochloride (GdnHCl) is useful to determine theΔG value. The free energy difference and population of folded and unfolded states depend on the concentration of denaturant ([D]) and both values are used for this equation, $\Delta G = \Delta G_0 + m[D]$, where m is the constant of proportionality which represents cooperativity of unfolding. Fitting the denaturation curve described in fraction of folded protein as a function of [D] reveals the values of ΔG_0 and m. This approach is applicable to amyloid fibrillation by regarding this reaction as two-state model between soluble monomers state and β-structured amyloid fibrils state.

Calorimetry

Calorimetry is one of the most powerful approaches to investigate the stability of protein which can directly determine the thermodynamic parameter, ΔH, the change in heat capacity (ΔC_p), ΔS, and ΔG. Differential scanning calorimetry (DSC) and isothermal titration calorimetry (ITC) are techniques for the high-sensitive measurement of reaction heat by changing temperature with fixed solvent conditions and changing solvent conditions with fixed temperature, respectively. DSC is usually used to study the thermally induced denaturation of native proteins by directly measuring accompanying heat of unfolding, ΔH and to produce ΔC_p from the temperature-dependence of ΔH. The net value of ΔH is the change in heat mainly stemming from the disruption of intramolecular interactions (69). Other thermodynamic parameters, ΔS and ΔG are available by using T_m obtained from DSC measurement; transition entropy is determined by equation $\Delta S = \Delta H/T$. In many cases, DSC performed not only for studying structural stability of single protein, but also applicable for studying intermolecular interaction such as protein-protein, protein-ligand, and protein-lipid interaction, which can also contribute to drug screening. In the DSC measurements, heat-induced unfolding has been recognized to be occasionally followed by an irreversible process that induces aggregation although protein aggregation usually has not been a target of calorimetry. In this work, I focused on this aggregation heat to understand the thermodynamics of protein aggregation including amyloid fibrils in chapter 3.

On the one hand, ITC also accurately detect the heat of the reaction in the ITC cell with continuous

stirring. ITC has been recognized as a direct and quantitative method for wide variety of intermolecular interactions and provides a series of thermodynamic parameters, the dissociation constant (K_D), ΔH, and binding stoichiometry (n). Other thermodynamic parameters, ΔS and ΔG are available by using the relationship $\Delta G = -RT\ln K_a = \Delta H - T\Delta S$. The value of ΔC_p is available from the temperature dependence of ΔH explained by Kirchhoff's relation $\partial \Delta H / \partial T = \Delta C_p$. To understand the heat capacity changes is very important because the sign and magnitude of ΔC_p reflect (de)hydration and the change in the accessible surface area. Hydration effects are proportional to the buried accessible surface area of polar and nonpolar residues. Hence, ΔC_p provides insightful information on the extent of exposed surface area following the conformational conversion or binding reaction.

Computational approach

Combination of experimental measurements with computational methods has expanded the more detailed molecular mechanism of protein folding and intermolecular interactions. Molecular dynamics (MD) simulation is a powerful way to study biomolecules at atomic resolution. Moreover, combination with NMR spectroscopy has shown to characterize the structures and the free energy landscape, which is a fundamental quantity in a statistical mechanics description of protein including disordered peptide (8, 70-75). The NMR chemical shifts are used as structural restraints, and the resulting free energy landscape obey the Boltzmann distribution corresponding to the force field used in simulations. Taken together, the MD simulation-based approach may help us to understand general thermodynamics of proteins including amyloidogenic proteins.

Thermodynamics of amyloid fibrils

Although advanced method and technology have improved the understanding on thermodynamics of proteins, many questions remain open regarding protein aggregation including amyloid fibrils and amorphous aggregates. Previously, Kardos *et al.* and Narimoto *et al.* examined conformational stability of amyloid fibrils formed from several amyloidogenic proteins and peptides against outer stress of chemical denaturant and heat. They demonstrated that amyloid fibrils are also denatured by outer stresses (76, 77).

In this work, I address further insights into thermodynamic properties of amyloid fibrillation by defining the difference in stability between the monomeric and fibrillar forms of a series of polypeptides (Table 1), ranging from short peptides (e.g., amyloid-β) to full-length proteins responsible for human diseases (e.g., α-synuclein and β_2-microglobulin), in terms of consideration of different characteristics in the sequence and structure of the monomeric state. In chapter 2, I show the systematic investigation on the thermal stability of various amyloid fibrils using temperature-induced dissociation. Interestingly, α-synuclein amyloid fibrils undergo cold denaturation. I proposed a unique thermodynamic property of amyloid fibrils in comparison with soluble globular protein. In chapter 3, I describe a novel methodology to directly measure the thermodynamic parameters of protein aggregation including amyloid fibril using calorimetry. By using ITC, I clearly showed that observation of heat of protein aggregation is possible for supersaturation-limited spontaneous fibrillation**,** and even for amorphous aggregations. Furthermore, based on the thermodynamic parameters obtained by ITC, I was also able to characterize conformational states of globular proteins, amyloid fibrils, and amorphous aggregates.

Chapter 2. Cold denaturation of α-synuclein amyloid fibrils

2-1. Introduction

Proteins natively folded under physiological conditions have evolved to maintain marginal stability and high solubility by dominantly burying hydrophobic residues and hydrogen-bonded peptide groups in cores while exposing hydrophilic residues to polar solvents. Breaking protein homeostasis by unregulated quality control often leads to protein misfolding and insoluble aggregates such as crystal-like amyloid fibrils or glassy amorphous aggregates (78, 79).

Amyloid fibrils have been extensively studied over the last decade due to their importance in serious pathologies such as Alzheimer's disease (AD) and Parkinson's disease (PD) (80-88), normal biological functions (82, 89), and nanomaterials (90). Denatured monomers, over the critical concentration of solubility, self-assemble to amyloid fibrils through a long lag phase for nucleation and a subsequent rapid elongation phase (82, 84, 91). This nucleation-growth mechanism is similar to that of the crystallization, which indicated that supersaturation or metastability limits the phase transition (79).

Various approaches such as X-ray crystallography (92), solution/solid-state NMR spectroscopy (91, 93), and computer-based simulations (94) have revealed the detailed structures of amyloid fibrils. The hierarchical conformations of typical mature amyloid fibrils consist of a bundle of protofilaments composed of a few β-sheet layers, in which each polypeptide chain typically assumes a U-shaped β-strand-loop-β-strand topology (91, 93, 94). Importantly, each β-sheet layer is sustained by intermolecular hydrogen bonds between the backbones of adjacent monomers as well as hydrophobic interactions between the β-sheet layers (82, 88, 91, 93-95).

Most proteins have been shown to accommodate amyloid-forming regions (96) and disease-unrelated proteins were shown to polymerize to fibrils (82, 97-99). Therefore, these common properties, regardless of the distinct amino acid sequence of constituent monomers, have suggested that the main-chain dominated formation of amyloid fibrils may be the generic nature of polypeptide chains (97, 100-102). This concept has indicated that the fundamental features of intermolecular protein misfolding are distinct from intramolecular protein folding achieved by the optimized packing of side chains.

Although the molecular mechanisms of fibrillation are becoming increasingly clear, few studies have described the disaggregation of amyloid fibrils with alternating environmental conditions using pH

(89, 95, 99, 103), heat (76), pressure (87), or chemical denaturants (77, 83). Kardos *et al.* previously showed the thermal denaturation of fibrils of β2-microglobulin (β_2m), responsible for dialysis-related amyloidosis, and its fragment and α-synuclein (αSN), a causative protein of PD (76). It has been shown that αSN fibrils (85, 86) and PDZ domain fibrils (98) disaggregated to oligomers and monomers at -15 °C and to soluble species at room temperature, respectively. However, to date, there has been no available systematic study on the cold and heat denaturation of amyloid fibrils from microscopic and macroscopic viewpoints. Considering the extensive interest in the conformation of αSN fibrils and oligomers (45, 80, 81, 85-87), it is critical to clarify the conformational stability of αSN fibrils. Here, I provided the complete characterization of the conformational transitions of αSN amyloid fibrils over a wide range of temperatures (0-110 °C), and described cold and heat denaturation and their molecular origins and mechanisms. These results contrast the thermodynamic mechanisms stabilizing the native and amyloid structures of proteins.

2-2. Materials and Methods

Reagents. Thioflavin T (ThT) and 5,5',6,6'-tetrachloro-1,1',3,3'-tetraethyl-benzimidazolylcarbocyanine iodide (JC-1) were purchased from Wako Pure Chemical Industries Ltd (Osaka, Japan) and Sigma-Aldrich Cooperation (St. Louis, MO), respectively. All other reagents were obtained from Nacalai Tesque (Kyoto, Japan).

Preparation of Proteins. The recombinant full-length human αSN and β_2m and the two αSN mutants, αSN_{103} and αSN_{118}, were expressed in *Escherichia coli* strain BL21 (DE3) and BLR (DE3) (Novagen, Madison, WI), respectively, and were purified as described (76, 104-106). The K3 peptide was obtained by the digestion of β_2m with *Acromobacter* protease I. The NAC peptide of αSN (NAC_{76-96}) and $A\beta_{1-40}$ peptide were purchased from Peptide Institute Inc. (Osaka, Japan). $A\beta_{1-42}$ was expressed and purified as described in *SI Materials and Methods*. Insulin was purchased from Wako Pure Chemical Industries Ltd (Osaka, Japan).

Preparation of Fibrils. Seed-dependent fibrillation of all proteins and peptides was made using 1-2% (weight/weight) seed fibrils formed spontaneously from monomers, and by ultrasonication with the cycles of 1-min sonication and 9-min quiescence under the desired solvent conditions at 37 °C. Full-length αSN fibrils were also elongated using stirring by a magnetic bar without sonication. The water bath-type ultrasonic transmitter with a temperature controller (ELESTEIN SP070- PG-M, Elekon, Tokyo) was used at an ultrasonic frequency of 17–20 kHz and power output of 350 watts. Amyloid fibril formation of αSN at 1.45 mg ml^{-1} in 20 mM sodium phosphate buffer (pH 7.5) containing 100 mM NaCl at 37 °C was monitored using ThT fluorescence (Fig. 1*A*; Fig. S1*A* and see *SI Materials and Methods*). Although spontaneous fibrillation did not occur even after 2 days without agitation (104), ultrasonication accelerated nucleation to produce fibrils with a lag phase of 10 h. The fragmentation of preformed fibrils and subsequent secondary nucleation may have also been enhanced by ultrasonication. Adding preformed fibrils as seeds to monomers under ultrasonication resulted in disappearance of the lag phase. Seeding under ultrasonication was more effective than seeding under stirring by a magnetic bar at 600

rpm, which indicated that the fragmentation of preformed fibrils occurred more frequently by ultrasonication than by stirring. The formation of fibrils was confirmed by far-UV CD (Fig. S1*A* and see *SI Materials and Methods*) and AFM (Fig. 1*C* and *D* and see *SI Materials and Methods*). The CD spectrum of αSN monomers and fibrils indicated a typical random coil with a minimum at ~210 nm and a β-sheet-rich conformation with a minimum at ~218 nm, respectively (Fig. S1*A*). AFM revealed morphologically different mature fibrils depending on the types of agitation. αSN fibrils formed by seeding under stirring ranged from submicrometer lengths to several micrometers with diameters of 7–11 nm (Fig. 1*C*). Ultrasonication generated homogeneous short fibrils with submicron lengths and diameters of 7–10 nm (Fig. 1*D*), which demonstrated the ultrasonication-dependent intensive fragmentation of fibrils. Amyloid fibrils were assumed to be in equilibrium with monomers, although fibrillation was often accompanied by the formation of oligomers and amorphous aggregates. Therefore, I examined the molecular species that remained soluble after the formation of αSN fibrils at pH 7.5 and 37 °C using far-UV CD and UV absorption spectroscopies and ultracentrifugation (215,000*g* for 2 h) (Fig. 1*G* and *H*; Fig. S1). The concentration of αSN in the supernatants after the formation of fibrils with 10 μM αSN was ~0.5 μM. The far-UV CD spectrum of the supernatant was consistent with that of the monomers (Fig. S1), which indicated that ~5% monomers remained in the solution. The details on the fibril formation of $A\beta_{1\text{-}40}$ and $A\beta_{1\text{-}42}$ are given in *SI Materials and Methods*.

Denaturation of Fibrils at the Various Temperatures. The far-UV CD spectra of fibril solutions prepared at various protein concentrations (1-10 μM) at 37 °C were obtained after incubation in the 0-110 °C range using a cell with 1 or 10 mm path lengths. The time-dependent cold denaturation of full-length αSN fibrils at 0, 10, 15, or 25 °C was observed by the CD at 220 nm. Data were fit using the following double exponential function.

$$y = y_0 + A_1 e^{-k_1 t} + A_2 e^{-k_2 t} \quad (1),$$

where y_0 is the signal at infinite time, k_1 and k_2 are rate constants, A_1 and A_2 signify the amplitudes of

the two phases, and *t* indicates the incubation time. Thermal denaturation at 50, 60, 70, 80, 90, 100, and 110 °C was monitored by CD at 220 nm. Combined with Gdn-HCl denaturation as described below, the apparent melting temperature (T_m) and *m*-values were determined by a regression analysis using a nonlinear least squares fitting of all sets of data to the sigmoidal equation under the assumption of a two-state transition between fibrils (F) and monomers (U).

$$S = \frac{(S_F + m_F T) + (S_U + m_U T) e^{-(\Delta H(1-T/T_m) - \Delta C_p((T_m - T) + T\ln(T/T_m)))/RT}}{1 + e^{-(\Delta H(1-T/T_m) - \Delta C_p((T_m - T) + T\ln(T/T_m)))/RT}} \quad (2)$$

where *S* is the signal intensity monitored by CD or ThT fluorescence, S_F and S_U are those of fibrils and monomers, respectively, and *T*, T_m, and *R* indicate temperature, the midpoint temperature of denaturation, and gas constant, respectively. ΔH and ΔC_p were incorporated in the equation. The initial and final baseline was described by $S_F + m_F T$ and $S_U + m_U T$, respectively. ThT assay was further conducted using fibril samples before and after cold/heat treatments as described above.

2-3. Results

Cold Denaturation of αSN Fibrils of at 0 °C and pH 7.5. The two types of mature αSN fibrils were prepared using the distinct agitations at pH 7.5 and 37 °C (see Materials and Methods). The formation and conformational properties of fibrils were confirmed by ThT fluorescence (Fig. 1*A*), far-UV CD (Fig. S1*A*) and atomic force microscopy (AFM) (Fig. 1*C* and *D*). Ultrasonication generated homogeneous shorter fibrils than the fibrils formed with stirring (Fig. 1*C* and *D*).

The temperature was decreased from 37 °C to 0 °C and conformational changes of αSN fibrils were monitored using far-UV circular dichroism (CD) (Fig. 1*B*). The intensity at ~218 nm decreased with incubation. The spectrum after a 10-h incubation was essentially the same as that of the monomers at 0 °C. Cold-denatured fibrils showed no ThT or JC-1 fluorescence at 485 nm or at 540 nm, respectively (Fig. 1*G*), and no large molecules were present in AFM images (Fig. 1*F*), indicating their complete denaturation to monomers. The molecular species and their amounts before and after cold denaturation at 0 °C were further examined using UV absorption, CD and analytical ultracentrifugation (Fig. 1*G* and *H*; Fig. S1). The results indicated that ~5% of monomeric αSN remained after fibril formation and the predominant species after cold denaturation were monomers (see *SI Materials and Methods*).

Two-Step Denaturation of αSN Fibrils via a Kinetic Intermediate. In order to explore the process of cold denaturation, the time course of changes in the CD signal at 220 nm was followed at pH 7.4 and 0 °C (Fig. 2*A*). The amplitude decreased and was saturated at ~10 h, which indicated the end of cold denaturation. Time-dependent CD signals fit well with a double exponential function (see Materials and Methods) with the rate constants of fast (k_1) and slow (k_2) phases. The average k_1 and k_2 values for short fibrils prepared using ultrasonication were 5.29 ± 0.75 h^{-1} and 0.70 ± 0.04 h^{-1}, respectively, with similar relative amplitudes (Table S1). These results suggest a three-state mechanism with an intermediate state.

The intermediate state of cold denaturation was characterized using JC-1 fluorescence and AFM images. The JC-1 fluorescence spectra revealed a kinetic intermediate αSN based on the characteristic emissions (107) (Fig. 2*B* and see *SI Materials and Methods*). AFM images were taken at different time

points during cold denaturation (Fig. 1*D-F*). The heights of fibrils (5-8 nm) at 10 h and 10 °C were lower than those of cold-untreated fibrils (7-10 nm), which supported the accumulation of a kinetic intermediate in which mature fibrils frayed into protofilaments.

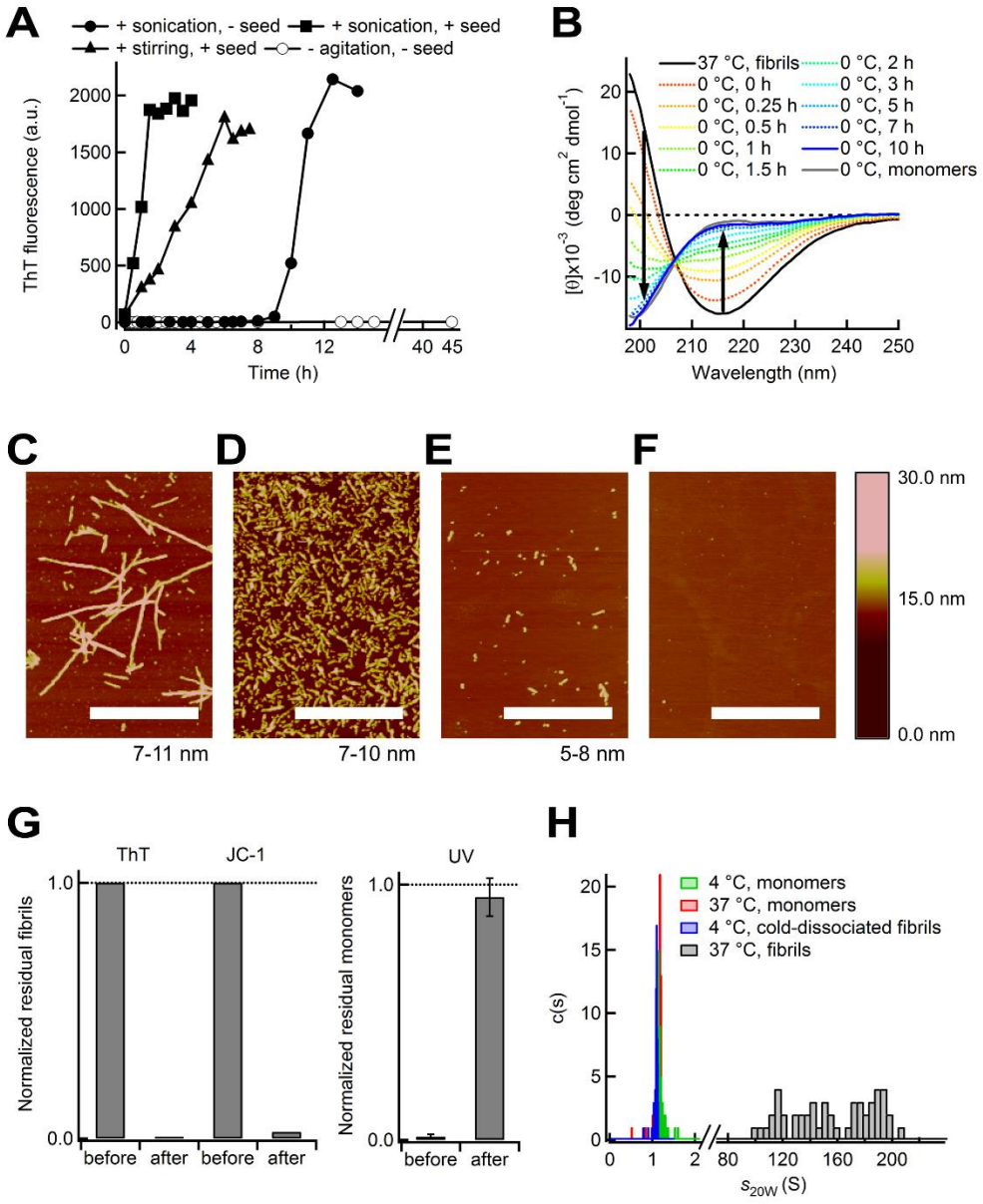

Fig. 1. Cold Denaturation of αSN Fibrils at 0 ºC. (A) αSN fibrillation at pH 7.4 at 37 ºC monitored by ThT fluorescence with and without fibril seeds under ultrasonication. (B) Denaturation of αSN fibrils, formed at 37 ºC, monitored at 0 ºC by far-UV CD. The spectra of fibrils before (black) and after the cold treatment for 10 h (blue) are displayed. The spectrum of monomers at 0 ºC (gray) is shown. The dissociation process is displayed by dotted curves and guided by arrows. (C-F) AFM images of αSN fibrils. Fibrils formed using stirring (C) or sonication (D). Fibrils after the cold treatment for 6 h at 10 ºC (E) and for 14 h at 0 ºC (F). Scale bars indicate 1 μm and average heights

are exhibited at the right. (G) Amounts of fibrils and monomers before and after the cold treatment at 0 ºC for 14 h determined using the ThT and JC-1 (107) fluorescence and UV absorption. (H) Fractions of molecular species against the S values ($s_{20,w}$). See also Fig. S1.

Factors Affecting the Cold Denaturation of αSN Fibrils. Physicochemical factors that may impinge on the kinetics of cold denaturation were investigated to obtain further insight into the mechanism of cold denaturation. The longer αSN fibrils, produced by seeding under stirring, also cold-denatured at 0 °C through biphasic processes (Figs. 1*C* and 2*A*). However, the rates of cold denaturation were slower for both the fast and slow phases than for the short fibrils: the average k_1 and k_2 values were 1.00 ± 0.13 h^{-1} and 0.16 ± 0.02 h^{-1}, respectively (Table S1). These results suggest that cold denaturation mainly occurs from the ends of fibrils and that ultrasonication increased the number of active sites of denaturation.

Cold denaturation was delayed when the concentrations of sodium chloride and αSN increased from 100 to 300 mM and from 10 to 100 μM, respectively (Fig. 2*C* and Table S1). On the other hand, the addition of guanidine hydrochloride (Gdn-HCl) accelerated cold denaturation (Fig. 2*D* and Table S1). Thus, cold denaturation is an additional factor that determines the stability of fibrils, which are dependent on solvent conditions and αSN concentrations. Cold denaturation was slower at 15 °C than at 0 °C in an opposite way to the Arrhenius equation (Fig. 2*E* and Table S1). Cold denaturation was not observed at 25 °C due to a large increase in fibril stability.

Reversible Cold Denaturation of αSN Fibrils. The reversibility of the cold denaturation of αSN fibrils was verified by adjusting the temperature. After 10 h of cold denaturation at 0 °C, in which the CD intensity at 220 nm reached a minimum, the temperature was increased to 37 ºC (Fig. 2*F*). The CD signal was gradually restored to its original intensity, indicating the regeneration of fibrils with high reversibility, in which a small amount of remaining fibrils worked as seeds. High reversibility was even observed for αSN solutions incubated at 0 ºC and 26 h, in which cold denaturation was apparently completed, which suggests that the completion of cold denaturation is difficult.

During fibril regeneration at 37 ºC, I again reduced the temperature to 0 ºC. Although regenerated fibrils again exhibited cold denaturation, the denaturation rate appeared to be decelerated. As the cycle of heating and cooling was repeated, reversibility declined with an apparent resistance to cold denaturation. This may have happened due to an adaptation to cold denaturation and/or the formation of irreversible aggregates of fibrils. Increasing the incubation temperature from 37 to 50 ºC enhanced cold resistance. Almost the same patterns of reversibility were verified using ThT intensities at 485 nm (Fig. 2*G*) and JC-1 at 540 nm (Fig. 2*H*).

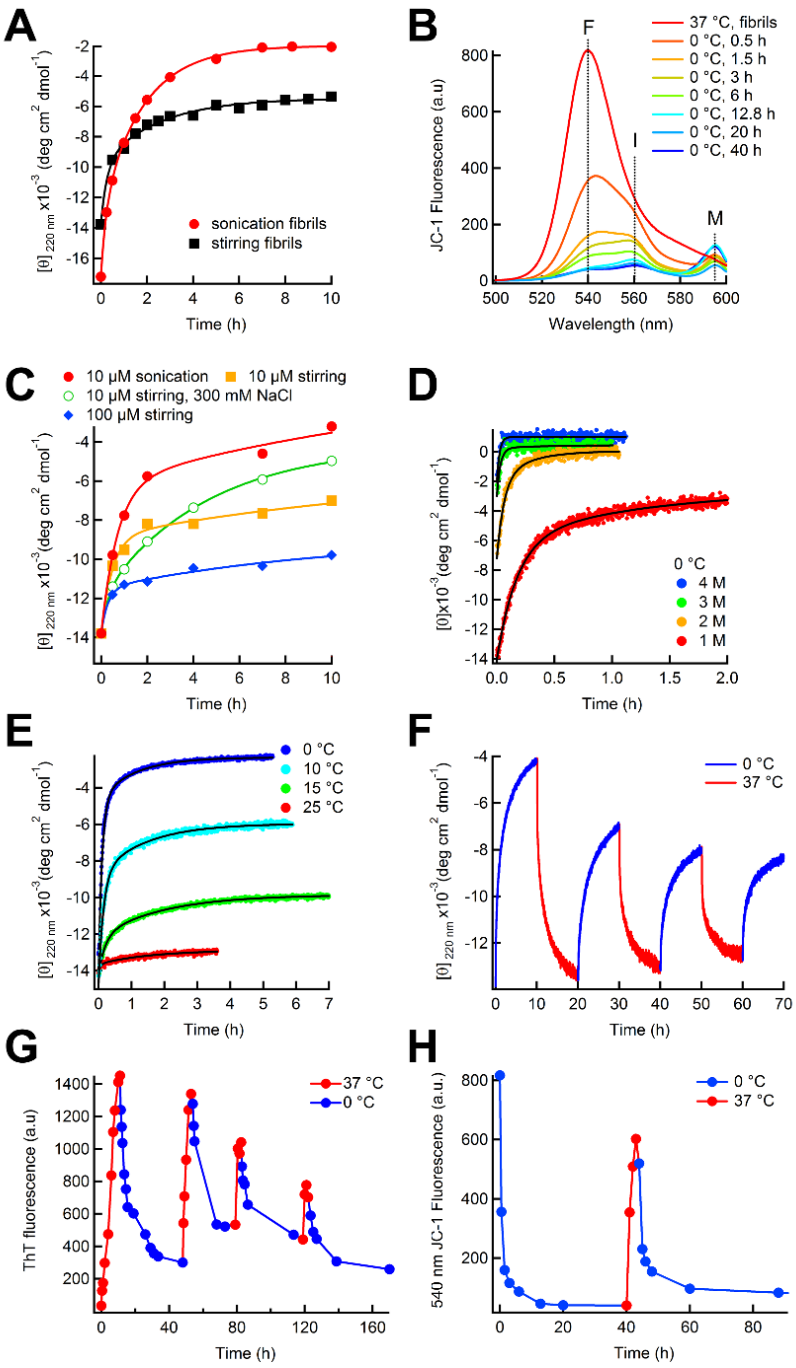

Fig. 2. Kinetics and Reversibility of the Cold Denaturation of αSN Fibrils. (A) Time-dependent conformational changes in αSN fibrils prepared with sonication (•) or stirring (■) monitored by CD at 220 nm at 0 ºC. (B) The JC-1 fluorescence spectrum was also used to monitor the conformational transition at 0 ºC. "F", "I", and "M" indicate mature fibrils, intermediate fibrils, and monomers, respectively. (C) The cold denaturation of fibrils at different salt or protein concentrations at 5 ºC monitored by CD at 220 nm. (D and E) The cold denaturation of fibrils without (D) and with various Gdn-HCl concentrations (E) at 0 ºC monitored by CD at 220 nm. Fitted curves are shown by continuous lines. (F-H) Reversibility of cold denaturation in the repeated cycles of cooling at 0 ºC (blue) and heating at 37 ºC (red) monitored by CD at 220 nm (F), ThT fluorescence (G), or JC-1 fluorescence (H). See also Table S1.

Heat Denaturation of αSN Fibrils and Their Reversibility. To obtain a more comprehensive understanding, the thermal responses of αSN fibrils over a wide temperature range were investigated. The time courses of conformational changes were monitored by far-UV CD at various temperatures from 37 to 110 ºC (Fig. 3). CD intensities at 220 nm increased rapidly and saturated to an equilibrium point within 0.2 h (Fig. 3*A*), which demonstrated that thermal denaturation was much faster than cold denaturation. The CD spectra following incubation at individual temperatures revealed the temperature-dependent heat denaturation of fibrils (Fig. 3*B*). The CD signal decreased with an increase in temperature and the spectrum at 110 ºC was indistinguishable from that of monomers at 110 ºC. These results indicated that the cross-β structure of αSN fibrils was destructed and depolymerized to monomers by heat, which is consistent with the finding of previous study (76).

The reversibility of heat denaturation was examined. The CD intensity at 220 nm was traced from 37 ºC to a desired temperature, i.e. 70, 80, 90, 100, or 110 ºC (Fig. 3*C*). The profiles of heat scans revealed a cooperative transition independent of the final temperature of heating. Fibrils began to melt from ~60 ºC and the recovery of intensity after cooling to 37 ºC depended on the final heating temperature. Although reversibility from heating to 70 ºC was ~100%, heating to 110 ºC almost completely abolished reversibility even after a 26-h incubation at 37 ºC without fibril seeds (Fig. 3; Fig. S2*A*). The addition of seeds (1% weight/weight) to the solutions subjected to heating to 110 ºC partly restored the CD intensity (Fig. S2*B*). I confirmed that an 8-h incubation at 37 ºC after heating to 100 ºC completely regenerated the fibrils even without seeds (Fig. S2*C*). Taken together, thermal treatment over 100 ºC decreased reversibility due to the complete melting of fibril seeds and/or the partial formation of irreversible aggregates. However, scanning up to 100 ºC secured reversibility by retaining fibrillation-competent monomers and fibril seeds.

Interestingly, when the denaturation of fibrils was monitored by differential scanning calorimetry (DSC), the heat capacity exhibited a negative peak and no reversibility was observed after heating to 125 ºC (Fig. 3*D*). The negative peak was opposite to the typical positive heat capacity peak accompanied by the unfolding of globular proteins (108), which suggested a positive enthalpy change in αSN fibril formation.

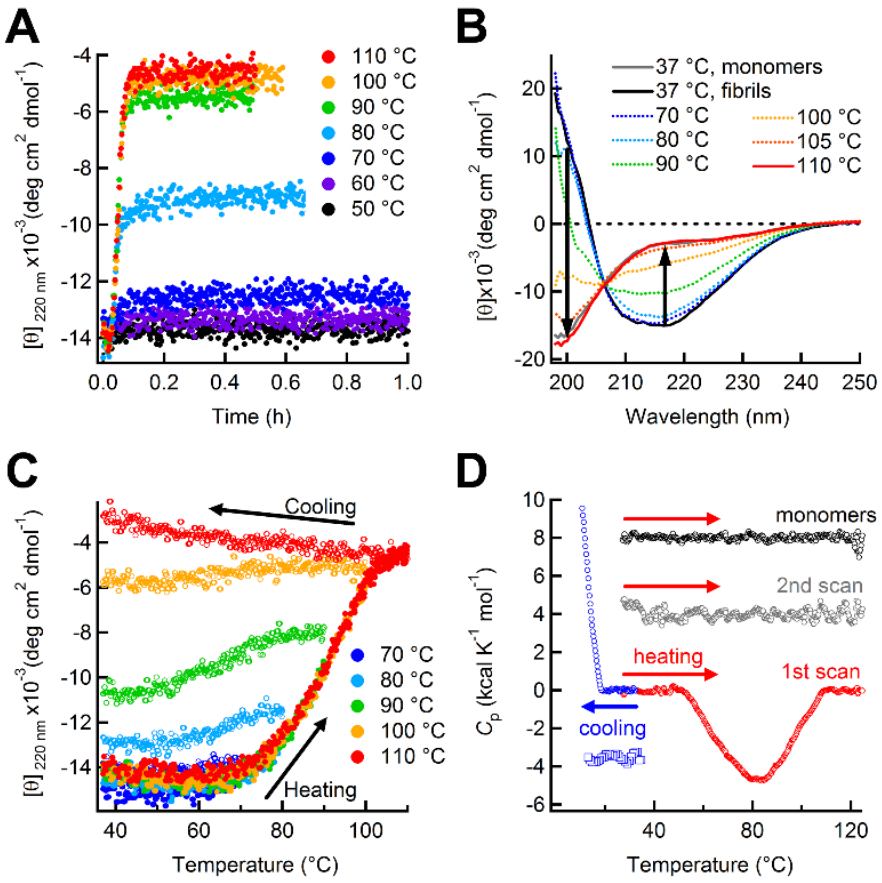

Fig. 3. Heat Denaturation of αSN Fibrils at Various Temperatures. (A) The kinetics of the thermal denaturation of αSN fibrils in the temperature range of 50 to 110 ºC monitored by CD at 220 nm. (B) CD spectra of αSN fibrils at 37 ºC after the heat treatment at 70, 80, 90, 100, 105, or 110 ºC. The transition process is displayed by dotted lines and guided by arrows. (C and D) The heat denaturation of fibrils observed by CD (C) or DSC (D) at a heating/cooling rate of 10 ºC min^{-1} and 1 ºC min^{-1}, respectively. The arrows indicate the direction of scanning. (C) The final temperature of each thermal scan was 70, 80, 90, 100, or 110 ºC. (D) The C_p curves of αSN fibrils (o) and monomers (o) and of the second heat scan of αSN fibrils (o) from 35 ºC to 125 ºC. The DSC thermograms of αSN (o) and β_2m fibrils (□) upon cooling from 37 to 10 ºC. See also Fig. S2 and Table S2.

Stability of the Amyloid Fibrils of Various Proteins in a Wide Temperature Range and Gdn-HCl-Assisted Cold Denaturation. To extract the general features of the temperature responses of amyloid fibrils, fibrils of various amyloidogenic proteins under different solvent conditions were investigated. The amyloidogenic polypeptides utilized were full-length αSN (Fig. 4*A* and *B*), the two C-terminus-truncated αSN mutants, $αSN_{118}$ (Met1 to Val118) and $αSN_{103}$ (Met1 to Asn103) (Fig. 4*B*), the

NAC peptide of αSN (Ala76 to Lys96), NAC_{76-96} (Fig. 4*B*), full-length β_2m and its K3 fragment (Ser20 to Lys41) (Fig. 4*C*), amyloid β_{1-42} ($A\beta_{1-42}$) and amyloid β_{1-40} ($A\beta_{1-40}$) peptides (Fig. 4*D*), and insulin (Fig. 4*D*). The thermal denaturation profiles of all the fibrils explored here were expressed as a fraction of the fibrils remaining at a given temperature. The melting temperatures (T_m) of all fibrils based on thermal denaturation profiles were summarized in Table S2 (see Materials and Methods)

The thermal stability curve of αSN fibrils at ~0.15 mg ml^{-1} and pH 7.5 from 0 to 110 ºC was first constructed based on the CD intensity (Fig. 4*A*). A bell-shaped curve explained the temperature-dependent conformational stability of amyloid fibrils in a two-state transition between fibrils and monomers. Fibrils were stable between ~25 and ~60 ºC, however, there were unstable below ~25 ºC and above ~60 ºC. The apparent midpoints at which 50% of fibrils depolymerized were 12 and 91 °C for cold and heat denaturation, respectively. Although the curve was symmetrical, signals at high temperature regions (60-100 ºC) fluctuated due to the formation of aggregates and/or fibril association.

Bell-shaped symmetric stability curves were also obtained for αSN_{118}, αSN_{103}, and NAC_{76-96} fibrils formed at 37 ºC and pH 7.5 (Fig. 4*B*). After incubation at 0 °C, fractions of the remaining fibrils were ~0.1 (αSN_{118}), ~0.15 (αSN_{103}), and ~0.25 (NAC_{76-96}), indicating the cold denaturation of fibrils. At 90 ºC, αSN_{118} and NAC_{76-96} fibrils were almost denatured by heat, whereas ~30% of αSN_{103} fibrils remained.

The decrease in pH to 2.5 extended the stable region of αSN fibrils toward lower and higher temperatures (Fig. 4*B*). No cold denaturation was observed at 0 ºC, although the thermal denaturation was still observed. Similar findings were also observed for αSN_{103} and αSN_{118} fibrils at pH 2.5 (Fig. 4*B*).

Although mature β_2m fibrils started to melt at ~90 ºC, showing notable tolerance for heat denaturation, no cold denaturation was observed at 0 ºC (Fig. 4*C*). K3 fibrils also denatured at high temperatures, however, they were not denatured at 0 ºC (Fig. 4*C*). Interestingly, thin and curved immature β_2m fibrils showed cold denaturation with ~15% of fibrils remaining at 0 ºC, although their heat denaturation was similar to that of K3 fibrils (Fig. 4*C*). The three types of fibrils of $A\beta_{1-42}$ and $A\beta_{1-40}$ peptides under different conditions exhibited almost complete heat denaturation at 100 ºC, but no cold denaturation at 0 ºC (Fig. 4*D*). Although the heat denaturation of insulin fibrils at pH 2.5 started at ~40 ºC, they were still stable at 0 ºC (Fig. 4*D*).

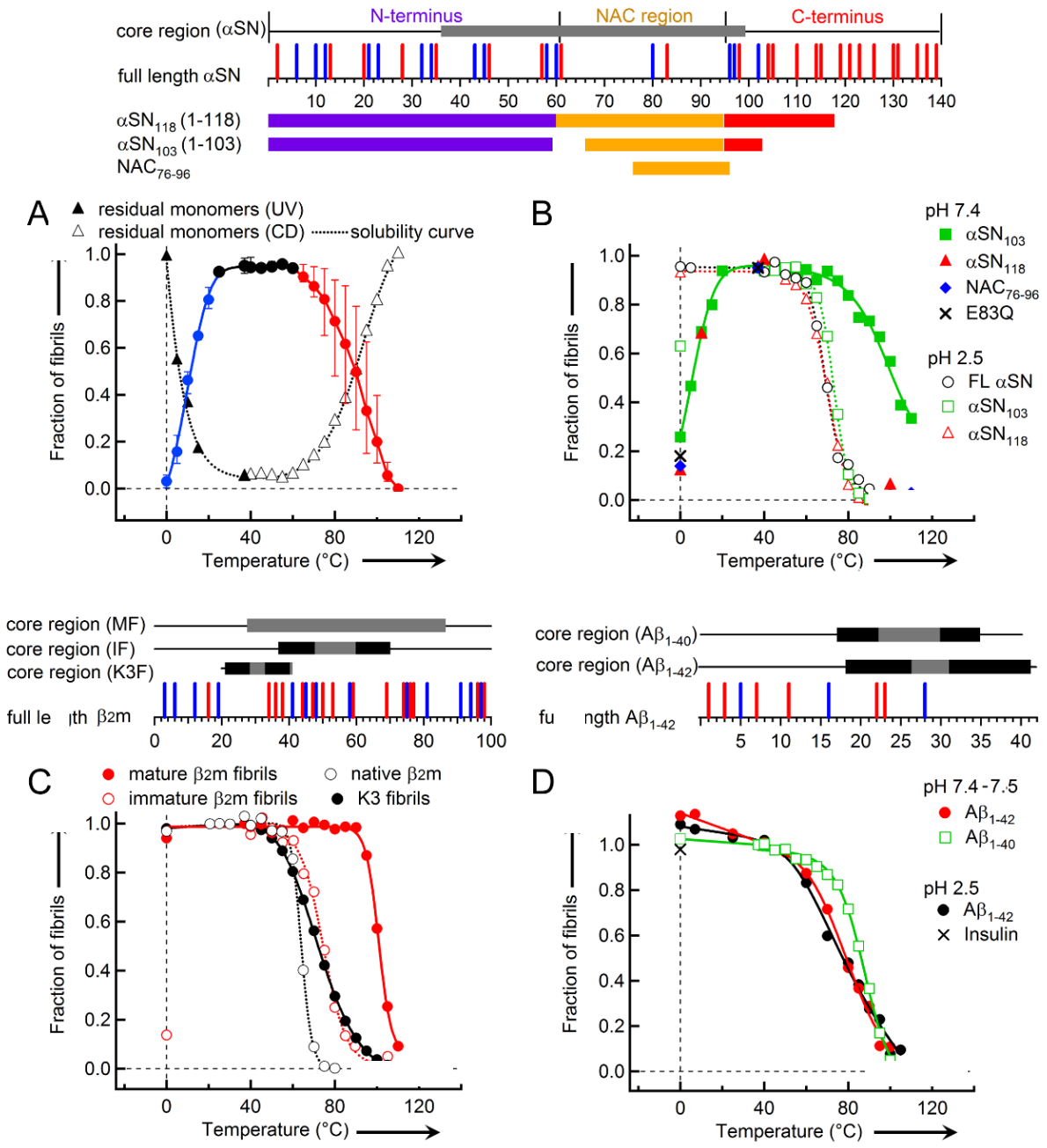

Fig. 4. Cold and Heat Denaturation of Various Fibrils over a Wide Range of Temperatures. (A) Temperature-dependent fractions of fibrils of full-length αSN at pH 7.5. The unstable temperature regions of fibrils against cold (●) and heat (●) and the stable region (●). The solubility curve of αSN was obtained using concentrations of residual monomers assayed by UV-visible (▲) or CD (△) spectra. (B) Stability curves of full-length αSN (○), $αSN_{103}$ (□), and $αSN_{118}$ (△) at pH 2.5 as well as $αSN_{103}$ (■), $αSN_{118}$ (▲), and NAC_{76-96} (♦) at pH 7.5. The amphipathic N-terminal (magenta), hydrophobic NAC (yellow), and hydrophilic C-terminal regions (red) of αSN are depicted at the top. (C) The remaining mature (MF) (●) and immature fibrils (IF) (○) of $β_2$m and the K3 fibrils (●) plotted against temperature. Fractions of native $β_2$m monomers (○) are also shown. (D)

Fractions of $A\beta_{1\text{-}42}$ fibrils at pH 7.5 (●) and 2.5 (●), $A\beta_{1\text{-}40}$ fibrils at pH 7.4 (□), and insulin fibrils (X) plotted against temperature. The negatively- and positively-charged residues of corresponding monomers at neutral pH are shown by red and blue bars, respectively. Core regions and β-strands in fibrils (Table S4) are signified by gray and black rectangles, respectively. All continuous lines were for an eye guide. (see also Fig. 5 and Table S4)

Then, the effects of Gdn-HCl on the stability of fibrils at different temperatures were examined to address the relationship between the chemical, cold, and heat stabilities of fibrils (see *SI Materials and Methods*). Using either CD or ThT fluorescence, ten different fibrils were observed to denature completely at the high concentration of Gdn-HCl (Fig. 5). Lowering the temperature to 0 ºC enhanced Gdn-HCl-induced denaturation of αSN fibrils formed at pH 2.5 and $A\beta_{1\text{-}42}$/$A\beta_{1\text{-}40}$ fibrils with decreasing the apparent midpoint Gdn-HCl concentration (C_m). These results indicate that the effects of Gdn-HCl and low temperature are additive with both destabilizing amyloid fibrils.

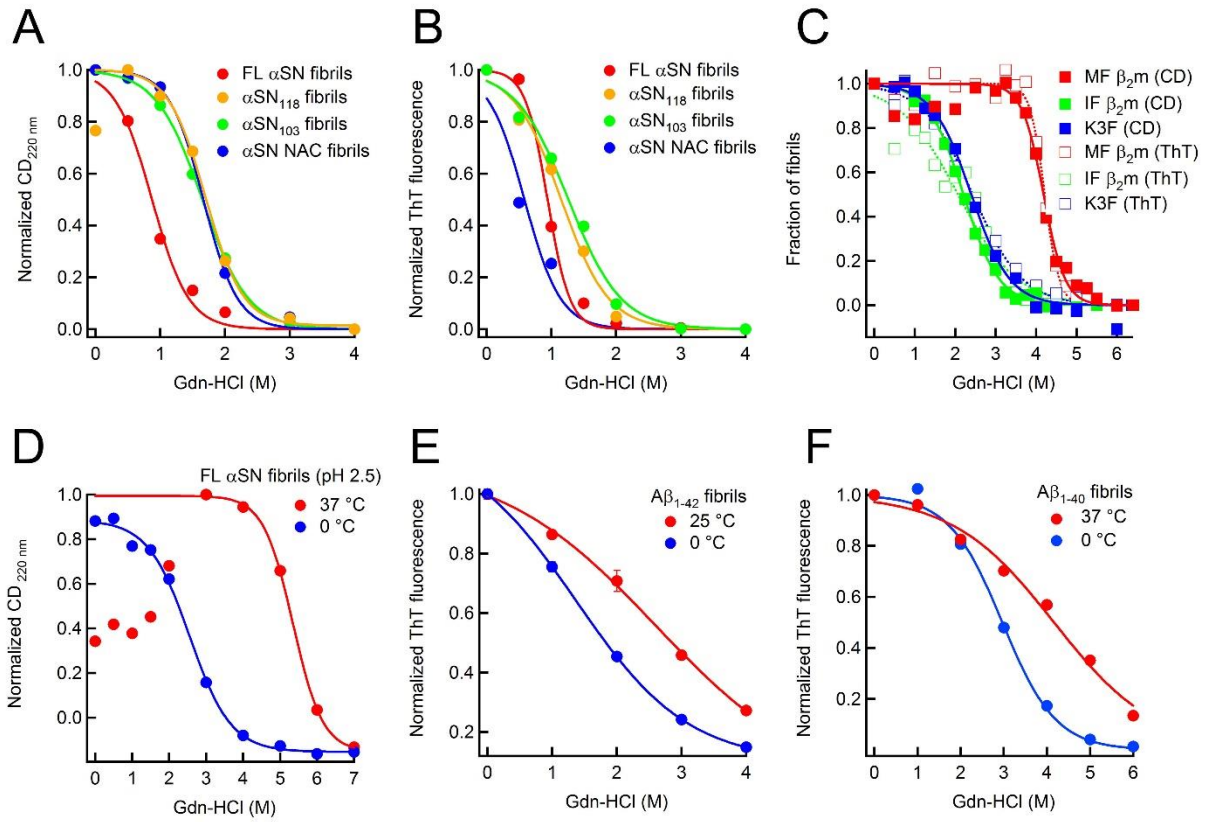

Fig. 5. Gdn-HCl-assisted Cold Denaturation of Various Fibrils. (A and B) Gdn-HCl denaturation of full-length αSN (FL αSN) (●), its mutants, αSN_{118} (●) and αSN_{103} (●), and a fragment ($NAC_{76\text{-}96}$)

(•) formed at pH 7.5, monitored by CD (A) or ThT fluorescence (B). (C) Gdn-HCl denaturation of two types of β_2m fibrils, mature fibrils (MF β_2m) (red) and immature fibrils (IF β_2m) (green) at acidic pH, and mature K3 fibrils (K3F) at pH 6.5 (blue), estimated using the CD (filled rectangle) and ThT intensities (open rectangle). (D) Gdn-HCl denaturation of FL αSN fibrils at pH 2.5 and at 37 (•) or 0 ºC (•) monitored by CD at 220 nm. (E and F) Gdn-HCl denaturation of $A\beta_{1-42}$ (E) and $A\beta_{1-40}$ fibrils (F) at various temperatures monitored by the ThT fluorescence intensity. The CD at 220 nm and ThT fluorescence at 485 nm were used to estimate the fractions of residual fibrils. All fitted results are shown by continuous lines.

Opposite Signs of Thermodynamic Parameters for αSN Fibrils to Those of Other Proteins. The thermodynamic parameters of fibril extension, which provides important information on the mechanism of fibrillation, were characterized using calorimetry. The seed-dependent growth of K3 fibrils was accompanied by the release of heat in accordance with previous results for β_2m fibril elongation (Fig. 6*A* and see *SI Materials and Methods*) (105). Seed-dependent $A\beta_{1-40}$ fibrillation also occurred exothermically. Interestingly, αSN fibril extension was accompanied by heat absorption. The apparent values of the enthalpy change (ΔH) for K3, β_2m, $A\beta_{1-40}$, and αSN fibril growth (pH 7.5) were -10.2, -28.5, -36.8, and +8.8 kcal mol^{-1} at 37 ºC, respectively (Table S3). The positive value of ΔH for the αSN fibrillation was consistent with the negative heat capacity peak observed upon heat denaturation by DSC (Fig. 3*D*). From the temperature dependence of ΔH, the change in heat capacity (ΔC_p) was shown to be 0.35 kcal mol^{-1} K^{-1} (Fig. 6*B*). This value was positive while those of the fibrillation and folding of β_2m were -1.14 and -1.34 kcal mol^{-1} K^{-1}, respectively (Table S3). The decrease in pH from 7.4 to 2.5 inversed the signature of ΔH and ΔC_p for the αSN fibril growth (Fig. 6*B*). The predicted ΔC_p values for protein folding of globular proteins was -1.56 K^{-1} for β_2m and that for αSN was -2.3 kcal mol^{-1} K^{-1} on the assumption that aSN, an intrinsically disordered protein, folds. This result showed that the empirical relationship on the basis of protein folding did not necessarily apply to protein misfolding. The inverse sign of ΔH and ΔC_p raised questions about energetic contributions to the stability of αSN fibrils inferred from other fibrils and protein folding.

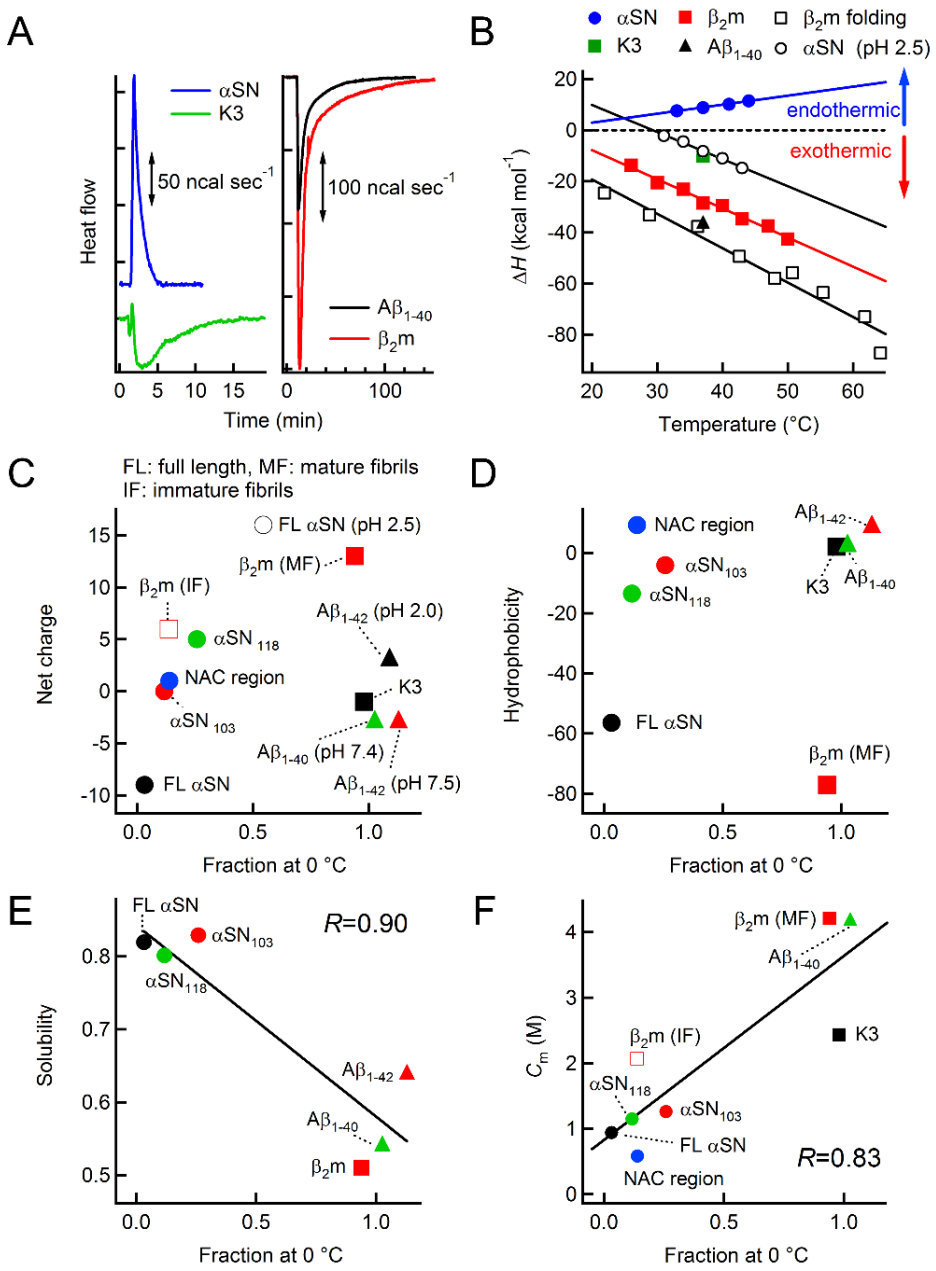

Fig. 6. Calorimetric Characterization of Fibril Extension and Correlations between Cold Denaturation and Physicochemical Properties. (A) Fibril elongations at 37 ºC observed using isothermal titration calorimetry for full-length αSN (blue), K3 (green), β$_2$m (red), and Aβ$_{1-40}$ (black). (B) Temperature-dependent changes in ΔH for the fibril growth of αSN at pH 7.5 (●) and 2.5 (o), and β$_2$m (■) and folding of β$_2$m (□). Values were also plotted for K3 (■) and Aβ$_{1-40}$ (▲) at 37 ºC. (C and D) Net charge (C) and hydrophobicity (D) of amyloidogenic monomers plotted against the fractions of remaining fibrils at 0 ºC (see Supplemental Experimental Procedures). ″FL″, ″MF″, and ″IF″ indicate ″full-length″, ″mature amyloid fibril″, and ″immature amyloid fibril″, respectively. (E and F) Solubility (E) of amyloidogenic monomers as well as C_m values of various amyloid fibrils (F) plotted against the fractions of remaining fibrils at 0 ºC. A correlation coefficient R value is shown.

2-4. Discussion

All of the fourteen fibrils examined here exhibited heat denaturation as well as Gdn-HCl denaturation. The T_m, C_m, and m values obtained were in similar ranges to those of globular proteins (Figs. 4-6, Table S2) (109). which suggests that the stabilities of amyloid fibrils are not very different from those of globular proteins (77, 110).

Based on the results obtained here, I addressed the molecular origin of the cold denaturation of αSN fibrils. Cold denaturation of fibrils formed by charge-deleted mutants (αSN_{103} and αSN_{108}) and hydrophobic NAC peptide at pH 7.4 raised a possible role for the charged residues at pH 7.4 (K43(+), K45(+), E46(-), H50(+), E57(-), K58(+), K60(+), E61(-), K80(+), E83(-), K96(+), K97(+), and D98(-)) buried in fibril cores (Fig. 4B, Table S4) without forming fully-satisfied electrostatic networks. Accordingly, full-length αSN fibrils were prepared at pH 2.5 at which negatively-charged residues are protonated. No significant cold denaturation was observed when full-length αSN, αSN_{103}, and αSN_{108} fibrils formed at pH 2.5 were incubated at 0 °C.

Therefore, the unfavorable burial of the negative charges in cores at neutral pH may be responsible for the cold denaturation of αSN fibrils because electrostatic repulsion becomes stronger with a decrease in temperature due to the increases in the dielectric constant (111) and in hydrophobic hydration (112). This view can be further supported by the findings that charge repulsion following the pH changes unfolds amyloid fibrils (89, 95, 99, 103) and even a single charge buried in a hydrophobic core readily dissociates fibrils (113). High packing density and hydrophobic burial with complementary pairs of buried polar groups are key ingredients of protein stability (114).

Most importantly, the positive values of ΔH and ΔC_p observed for αSN fibrils by ITC and DSC were opposite to those of protein folding and other cases of protein misfolding reactions (105, 108, 109, 112), arguing strongly for the burial of charges as evidenced by the positive ΔC_p value following dehydration of charged residues (115, 116). Such adverse changes of ΔH and ΔC_p were also detected in DNA-protein (117), nucleotide-protein (118), lipid bilayer-protein (119), and the anion-protein binding (120) systems as well as and DNA condensation (121) in which charges were buried upon complexation. The recent study also indicated that the unstable glucagon fibrils formed with large positive ΔH and ΔC_p

values was attributed to the possible unfavorable burial of polar and/or charged residues (122).

However, fibrils of αSN mutant (E83Q) showed cold denaturation at pH 7.4 (Fig. 4B), which suggested that the charge burial of E83 did not occur in forming fibrils or that buried charges formed satisfactory electrostatic networks. Alternatively, it may suggest the involvement of an additional factor in the cold denaturation of αSN fibrils. Although the unfavorable burial of a negative charge among E46, E57, E61, and D98 in the cores may have been responsible for the cold denaturation of αSN fibrils, cold denatruation of immature β_2m fibrils and Gdn-HCl-promoted cold denaturation of $A\beta_{1\text{-}40}$/$A\beta_{1\text{-}42}$ fibrils and αSN fibrils at pH 2.5 suggest that cold denaturation is common phenomenon to amyloid fibrils even in the absence of unique burial of charged groups as shown with a high positive correlation (R=0.83 and p<0.01) between the fraction of fibrils at 0 °C and the C_m value of the Gdn-HCl-induced denaturation (Fig. 6F).

The lack of significant correlations between the fraction of fibrils at 0 °C and net charge, hydrophobicity, or ΔH suggests that there are currently no clear mechanisms to explain the cold denaturation of fibrils based on protein (un)folding (Figs. 6C and D, Fig. S3A). Nevertheless, a strong negative correlation between the fraction of fibrils at 0 °C and protein solubility (R=-0.9 and p<0.015) (Fig. 6E) implies that fibrils with a propensity to cold-denature are those with intrinsically high solubility. When proteins with intrinsically high solubility form fibrils at ambient temperatures by overcoming solubility and taking advantage of the main-chain dominated architecture, they are more likely to be disassembled at low temperatures. Such amyloid fibrils may be detected by the decreased or positive ΔH value together with the positive ΔC_p value of fibrillation (Figs. S3A and B).

The overall process for the thermal responses of αSN fibrils was drawn schematically in Fig. 7. Mature αSN fibrils are stable (20-60 °C), as the temperature decreases below 20 °C, fibrils begin to denature to monomers through a thin fibrillar intermediate, which may be formed by the dissociation of mature fibrils without axial fibril breakage. Dissociation of mature prion protein fibrils by charge repulsion into protofilaments may reflect similar lateral dissociation behavior of mature αSN fibrils (103). The driving force for the cold denaturation of αSN fibrils is the entropy-driven salvation of residues from the interior of fibrils based on amyloid-specific thermodynamics of the enthalpic penalty

of endothermic reaction and increase in heat capacity. On the other hand, heat denaturation was observed for all the fibrils examined. The thermodynamic driving force of depolymerization at high temperatures may be conformational entropy, similar to the unfolding of globular proteins at high temperatures.

Finally, in contrast to solid formation above the critical concentration, increases in solubility below the critical concentration dissociate solid states (84, 88). Accordingly, the conformational stability of amyloid fibrils can be defined by solubility (76, 77, 84, 88, 105, 110), which is the amount of remaining soluble monomers in equilibrium with fibrils. This provides a simple, but understandable concept that fibril stability can be determined by the thermodynamic solubility of monomers without considering complicated mechanisms. Mature αSN fibrils formed at pH 7.5 showed a unique U-shaped solubility curve in the temperature range of 0 to 110 °C, which was an exact inverse pattern of the stability of αSN fibrils (Fig. 4*A*). I consider that the cold denaturation phenomena observed here were also coupled with the increased solubility at low temperatures.

Combining the viewpoints of solubility, crystalline amyloid fibrils, and glass-like amorphous aggregates, we can further understanding of the thermodynamic mechanism of protein fibrillation. Furthermore, my results also provide biological implications for αSN protein homeostasis. The disaggregation and clearance of αSN aggregates should be easier to achieve than those of Aβ, β_2m, and insulin fibrils taking advantage of the marked propensity for cold-denaturation of αSN fibrils even near the physiological temperatures. However, cold adaptation may impede efficient αSN protein homeostasis.

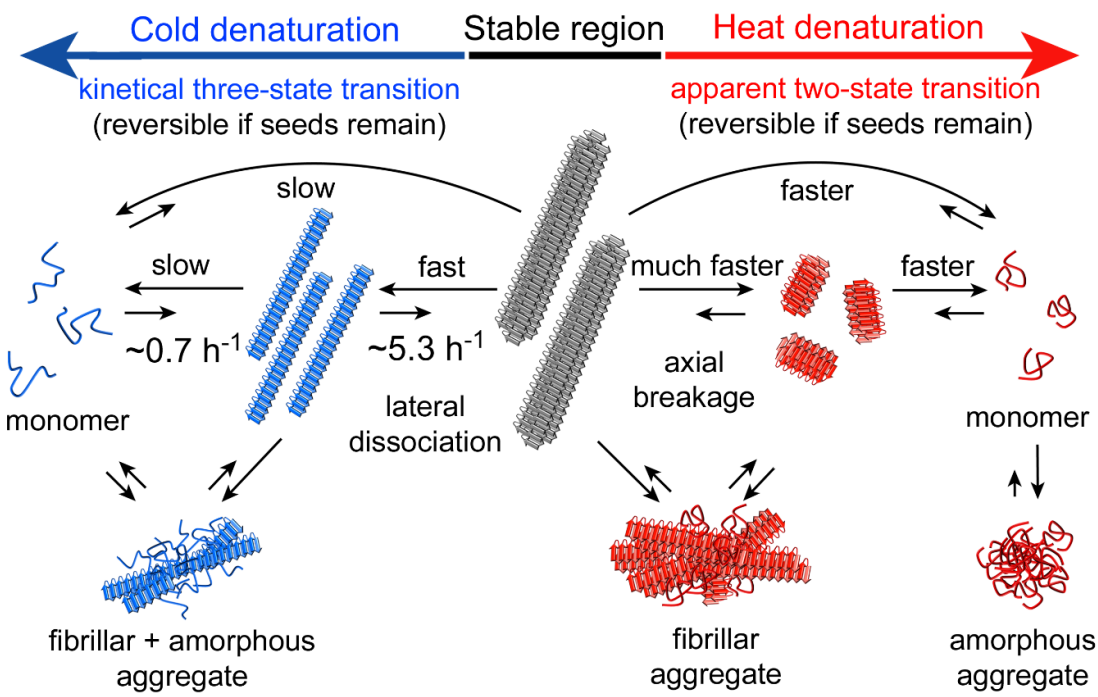

Fig. 7. Schematic Mechanism of the Cold and Heat Denaturation of αSN Fibrils. Upon a decrease in temperature, stable fibrils (gray) dissociate to monomers (blue curve) via a kinetic intermediate with a thin fibrillar conformation (blue). The direct detachment of monomers from fibril ends, indicated by dashed lines, occurs. Fibrils and monomers under high temperatures are represented by red. At elevated temperatures, the dissociation of monomers from fibril ends also takes place, which is further amplified by fibril breakage. The formation of fibrillar and amorphous aggregates at low and high temperatures is also shown. The rate constants at 0 °C are given below the arrows.

2-5. Supporting Information

Supplemental Experimental Procedures

Residual Monomers in αSN Fibril Solutions before and after Cold/Heat Treatments. Sample solutions of fresh full-length αSN fibrils formed at 37 °C and of fibrils incubated for 15 h at 0 °C were ultracentrifuged at 60,000 rpm for 2 h at 37 or 4 °C, respectively. The concentration of soluble proteins in supernatants was determined by UV absorbance at 280 nm with an extinction coefficient of 5,960 M^{-1} cm^{-1} (104, 106). The far-UV CD spectra of the remaining soluble proteins were identical to those of monomers, which indicated that the remaining species were in monomers. The precipitated fraction was estimated by subtracting the concentration of soluble monomers from the total concentration. Alternatively, the CD intensity at 220 nm was used for estimating fractions of the residual fibrils and monomers based on the intensity of fibrils at 37 °C and of monomers at each temperature examined. The molecular species and their amounts after cold denaturation at 0 °C were further examined using UV absorption spectroscopy (Figs. 1G and S1). UV absorption spectra detected ~95% soluble proteins in the supernatant after ultracentrifugation at 215,000*g* (Fig. 1G). The overall pattern of the far-UV CD spectrum of the supernatant was similar to that of the monomers (Figs. S1G and S1H). The homogeneity of fibril solutions was also investigated using sedimentation velocity analysis with analytical ultracentrifugation (Fig. 1H and S1). The sedimentation coefficient ($s_{20,w}$) of αSN monomers at 0 and 37 °C, obtained using the apparent partial specific volume (Fig. S1F and see also Supplemental Experimental Procedures), was ~1.2 S, which indicated that the unfolded αSN was monomeric (Fig. 1H). A series of sedimentation curves at 37 °C were traceable, signifying that fragmented fibrils by ultrasonication were sufficiently populated to be analyzed. The $s_{20,w}$ values at 37 °C were distributed from 100 to 200 S, which corresponded to various sizes of amyloid fibrils. However, ~5% of αSN molecules did not sediment at 8,000*g* (Fig. S1D), which coincided with the amount of residual monomers. Fibrillar solutions, subjected to the cold treatment at 0 °C for 17 h, exhibited similar $s_{20,w}$ values to monomer solutions, which suggested that the predominant species after cold denaturation were monomers.

Sedimentation Velocity with Analytical Ultracentrifugation. Sedimentation velocity measurements were performed on αSN monomers and fibrils at 4 and 37 °C using a Beckman-Coulter Optima XL-I analytical ultracentrifuge (Fullerton, CA, USA) equipped with an An-60 rotor and two- or six-channel charcoal-filled Epon cells. The samples were first centrifuged at 3,000 rpm (700*g*) for 5 min to stabilize the temperature, and after precentrifugation, the rotor speed was increased to 10,000–20,000 rpm (7,830–31,310*g*) and absorbance data at 220 nm were collected at intervals of 10–20 min. A radial increment of 0.003 cm was set to the continuous scanning mode. The protein concentrations were adjusted to absorbance values of 0.8-1.2. The sedimentation coefficients, corrected to s_{20W} in standard solvent conditions where the density and velocity of pure water at 4 and 37 °C was considered, were obtained from the data by the van Holde–Weischet method with the software UltraScan 9.9 (www.ultrascan.uthscsa.edu), using the partial specific volume of amyloid fibrils determined in previous study (102).

High Precision Density Measurements. Density of monomeric αSN was made using a vibrating tube density meter (DMA5000, Anton Paar, Austria) with a precision of 1×10^{-6} g ml^{-1}, and the polypeptide concentration was between 0.2 and 1.6 mg ml^{-1}. The adjustments with water and air were performed following every single set of measurements, and almost no deviation of water density before and after a series of density measurements was confirmed. The plotted density of αSN monomers against protein concentrations was fitted using equation to obtain the apparent specific volume (ν_{app}) (102),

$$\rho = \left(1 - \nu_{app}\rho_0\right)c + \rho_0 \quad (1)$$

where ρ and ρ_0 are the densities of the solution and solvent, respectively, and c is the concentration of αSN in g m^{-1}.

A Kinetic Intermediate αSN Fibrils during Cold Denaturation by JC-1. The cold denaturation process was observed using JC-1 fluorescence. The JC-1 fluorophore was previously shown to distinguish the two types of fibrils and monomers of αSN with fluorescence emissions at 540, 560, and 595 nm, respectively (107). The intensity at 540 nm, representing mature αSN fibrils, decreased as cold denaturation proceeded (Fig. 2B). The intensity at 560 nm increased and subsequently decreased, while the intensity at 595 nm, representing monomers, increased. Therefore, the molecular species that engaged in the intensity at 540 nm and accumulated maximally at ~3 h could be a kinetic intermediate.

Gdn-HCl-assisted Cold Denaturation of Amyloid Fibrils. The Gdn-HCl-dependent denaturation of a series of fibrils under pH and temperature conditions in which fibrils were stable in the absence of Gdn-HCl were examined. The concentrations of monomers in fibrillar states were as follows: full length αSN, 50 μM (0.72 mg ml^{-1}); $αSN_{118}$, 50 μM (0.60 mg ml^{-1}); $αSN_{103}$, 50 μM (0.52 mg ml^{-1}); NAC_{76-96}, 312 μM (0.70 mg ml^{-1}); $β_2m$, 50 μM (0.59 mg ml^{-1}); K3, 50 μM (0.12 mg ml^{-1}); $Aβ_{1-42}$, 50 μM (0.22 mg ml^{-1}); $Aβ_{1-42}$, 50 μM (0.22 mg ml^{-1}). Denaturation was monitored by CD at 220 nm and ThT fluorescence (Fig. 5). Full-length αSN, $αSN_{118}$, $αSN_{103}$, and NAC_{76-96} fibrils at pH 7.5 and 37 ºC were observed to denature completely at 3.0 M Gdn-HCl using either CD or ThT fluorescence (Figs. 5A and 5B). Transitions monitored using ThT fluorescence were preceded by those monitored using CD, which implied that structures responsible for ThT binding were destructed prior to β-sheet melting. In the case of $β_2m$-related fibrils, immature $β_2m$ and mature K3 fibrils showed denaturation curves similar to that of αSN-related fibrils (Fig. 5C). Mature $β_2m$ fibrils were highly stable against Gdn-HCl, exhibiting high cooperativity, as well as heat denaturation. αSN fibrils formed at pH 2.5 and $Aβ_{1-42}$ and $Aβ_{1-40}$ fibrils formed at pH 7.5 were further investigated at 0, 25, and 37 ºC (Figs. 5D-5F). αSN fibrils formed at pH 2.5 and 37 ºC showed a slightly higher resistance to Gdn-HCl than that of fibrils formed at pH 7.5 and 37 ºC (Fig. 5D). However, lowering the temperature from 37 to 0 ºC enhanced Gdn-HCl-induced denaturation. Lowering the temperature from 25 ºC to 0 ºC (Fig. 5E), which was also observed for $Aβ_{1-40}$ fibrils (Fig. 5F). The apparent midpoint (C_m) and *m*-values of denaturation were determined

by fitting the observed results to the following sigmoidal equation assuming a two-state transition mechanism between fibrils (F) and soluble proteins (U) (77).

$$S = \frac{(U_0+U_S c)+(F_0+F_S c)e^{-(-C_m m+mc)/RT}}{1+e^{-(-C_m m+mc)/RT}} \quad (3)$$

where c is the concentration of Gdn-HCl. The initial and final baselines are described by $U_0 + U_S c$ and $F_0 + F_S c$, respectively. The kinetics of the Gdn-HCl-induced denaturation of fibrils were analyzed by fitting the amplitude at 220 nm to equation (1).

Isothermal Titration Calorimetry (ITC). ITC measurements for the elongation of full-length αSN, K3, and $A\beta_{1\text{-}40}$ fibrils were performed with a VP-ITC instrument (GE Healthcare, MA, USA). αSN monomers at 300 μM in the injection syringe were titrated to αSN fibrils at 50 μM in the cell at 31, 33, 37, 39, 41, and 43 °C. Five titrations of 5 μl in total were spaced at intervals of 7,200 s at a stirring of 611 rpm. K3 monomers at 135 μM were also injected in 10 μl aliquots to seed fibrils at 20 μg ml^{-1} in the cell at pH 2.5 in the presence of 50 mM NaCl at 37 °C. A single injection of 50 μl $A\beta_{1\text{-}40}$ seed fibrils at 55 μM in the syringe to $A\beta_{1\text{-}40}$ monomers at 8 μM in the cell was conducted in 50 mM sodium phosphate, 100 mM NaCl, pH 7.5 at 37 °C. ΔH values were calculated using peak areas after subtracting the heat of dilution and baseline correction. The ΔC_p value was obtained from the relationship of $\partial \Delta H / \partial T$.

Differential Scanning Calorimetry (DSC). DSC measurements of the fibrils and monomers of αSN and β_2m fibrils at 0.1 mg ml^{-1} were performed with a VP-DSC calorimeter (GE Healthcare, MA, USA). Scanning between 37 and 120 °C was applied to αSN in the monomeric and fibrillar states at a scan rate of 1 °C min^{-1} for thermal denaturation. Cooling of fresh αSN fibrils from 37 to 5 °C was conducted with a distinct scan rate considering the slow kinetics of cold denaturation: from 37 to 10 °C with a scan rate of 1 °C min^{-1}.

Thermal Stability of Native β_2m Monitored by DSC and CD. The thermal stability of native β_2m was measured by DSC and CD. In the case of DSC, 0.2 mg ml^{-1} β_2m in 50 mM sodium phosphate buffer (pH 7.0) containing 100 mM NaCl was scanned at a rate of 1 °C min^{-1}. After baseline fitting and subtraction, the native fraction as the function of temperature was calculated from the area of the heat transition curve of unfolding integrated up to the respective temperature in relation to the entire calorimetric enthalpy of unfolding (ΔH_{cal}): $F_N(T) = 1 - \Delta H(T) / \Delta H_{cal}$. In the case of CD spectroscopy, the thermal denaturation of β_2m was measured at a concentration of 0.06 mg ml^{-1} in 20 mM sodium phosphate (pH 7.0) at 220 nm in a 5 mm quartz cell using a heating rate of 30 °C h^{-1}. The native fraction was calculated by assuming a two-state transition:

$$F_N(T) = (f_{CD}(T) - f_{CD,D}) / (f_{CD,N} - f_{CD,D}) \quad (2)$$

where f_{CD}(T) is the recorded CD amplitude at temperature T, and $f_{CD,N}$ and $f_{CD,D}$ are values for the native and unfolded states at temperature T calculated from linear extrapolation from the pre-transition and post-transition parts of the unfolding profile. The thermal unfolding of native β_2m was fairly reversible (80-90%), which was verified by second scans after cooling back the samples.

Calculating the Changes in Heat Capacity using Statistical Analysis

The heat capacity change (ΔC_p) for globular proteins can be predicted by using the number of amino acid residues (Num) of the protein of interest and the changes in accessible surface area (ΔASA) based on the following relationships (109).

$$\Delta ASA\ (\text{Å}^2) = -907 + 93 \times \text{Num} \quad (3)$$

$$\Delta C_p\ (\text{cal mol}^{-1}\ \text{K}^{-1}) = -119 + 0.20 \times \Delta ASA\ (\text{Å}^2\ \text{molecule}^{-1}) \quad (4)$$

Prediction of the Various Physicochemical Properties. Hydrophobicity of proteins used here was calculated using the data suggested by Kyte and Doolittle (http://www.vivo.colostate.edu/molkit/hydropathy/scales.html) (123). Solubility was calculated using SOLpro (http://scratch.proteomics.ics.uci.edu/) (124).

Recombinant Expression of $A\beta_{1-42}$. $A\beta_{1-42}$ was expressed recombinantly in *E. coli*. The DNA sequence encoding the human $A\beta_{1-42}$ peptide was artificially constructed using codons preferred by *E. coli* to reach a good expression level. An extra Met residue was inroduced to the N-terminal of the peptide and the construction was equipped with NdeI and BamHI restriction sites at the 5' and 3' ends of the DNA construct. The construct was ordered from Integrated Gene Techologies (Germany), as a synthetic gene in a pZErO-2 vector and was subcloned into pAED4 vector (125). The protein expression using the pAED4 plasmid was carried out in *E. coli* BL21 (DE3) pLysS strain (Novagen, Inc., Madison, WI), using 1 mM IPTG for induction. The peptide accumulated in inclusion bodies in the cells. The peptide was purified physically based on its polymerization ability, similar to the purification of compounds or proteins by crystallization and recrystallization. In the monomeric form, the non-soluble contamination could be removed by centrifugation, then, by growing fibrils, the peptide could be separated from non-polymerizing material again by centrifugation. After monomerization of the peptide, the process could be repeated. In more details, the purified inclusion bodies were dissolved in 20 mM NaOH. Non-soluble fraction was removed by spinning down at 50,000*g* for 30 min. The pH of the supernatant was then set to 2 adding HCl, spun down again at 4 °C for 30 min at 40,000*g* and amyloid fibrils from the supernatant were grown for 24 h at 37 °C. The fibrils were collected by centrifugation at 40,000*g* for 2 h, resuspended in water and spun down repeatedly. Finally the pellet was lyophilized. Lyophilized Aβ was dissolved in 100% hexafluoroisopropanol for monomerization (6 h at room temperature), froze in liquid N_2 and lyophilized again. According to my results, the polymerization of this recombinant $A\beta_{1-42}$ peptide was found to be similar to that of synthetic $A\beta_{1-42}$ peptide. There are some advantages of my purification method, such as the purified material contained no trifluoroacetic acid remnants.

Fluorescence Assay. The formation and depolymerization of fibrils were monitored by a fluorometric assay with ThT at 37 °C. Excitation and emission wavelengths were 445 and 485 nm, respectively. 5 μl aliquots were taken from each reaction tube and mixed with 1.0 ml of 5 μM ThT in 50 mM glycine-NaOH buffer (pH 8.5). The cold denaturation of αSN fibrils at 0 °C and refibrillation at 37 °C were also monitored by JC-1 fluorescence. JC-1 fluorescence spectra were collected between 500 and 600 nm with an excitation at 490 nm in the presence of 0.23 μM JC-1. The fluorescence spectra of ThT and JC-1 were measured using a F7000 fluorescence spectrophotometer (Hitachi, Japan).

Circular Dichroism Spectroscopy Measurements. Far-UV CD spectra of proteins and peptides in soluble and insoluble states were measured with a J-820 spectropolarimeter (Jasco, Japan) using a cell with a light path of 0.1, 1 or 10 mm at the desired solvent conditions. Individual fibril solutions were diluted to 0.1 mg ml^{-1} for CD measurements. The solutions were constantly stirred at 1,000 rpm using a magnetic bar in the 10 mm cell (2 ml) to remove an artifact from the precipitation of fibrils. The CD signals between 195 and 250 nm were expressed as mean residue ellipticity [θ] (deg cm^2 $dmol^{-1}$). Temperature regulation was carried out using a PTC-423L Peltier-unit (Jasco, Japan).

Atomic Force Microscopy (AFM) Measurements. AFM images were obtained using a Digital Instruments Nanoscope IIIa scanning microscope (Veeco, Santa. Barbara, CA). A 10 μl sample solution of 10 μM proteins was spotted onto freshly cleaved mica and left on the surface for 1 min. The surface was washed twice by 10 μl water and then blown off with compressed air. The scanning tip was a Si microcantilever and the scan rate was 1.0 Hz. The average height of the fibrils was estimated based on the peak height values measured.

Fibril Formation of $A\beta_{1-40}$ and $A\beta_{1-42}$. Lyophilized recombinant $A\beta_{1-42}$ peptide was dissolved in 20 mM NaOH at a concentration of 3 mg ml^{-1} and used as a monomer stock for experiments. Fibril stocks were grown at 1 mg ml^{-1} concentration at 37 °C, 24 h, in a shaker bath either at pH 7.5 in 10 mM Na-phosphate buffer by neutralizing the NaOH content with appropriate amont of HCl or at pH 2.0 adjusted by HCl. Synthetic $A\beta_{1-40}$ peptide (Peptide Research Institute, Japan) was dissolved at 1 mM

concentration in 0.1% ammonia solution on ice. Polymerization was carried out at 1 mg ml^{-1} concentration in 10 mM Na-phosphate, 50 mM NaCl at pH 7.4 overnight at 37 °C in a sonicated bath (ELESTEIN SP070- PG-M, Elekon, Tokyo) using cycles of 1 min sonication followed by 9 min quiescence.

Supplemental Figures

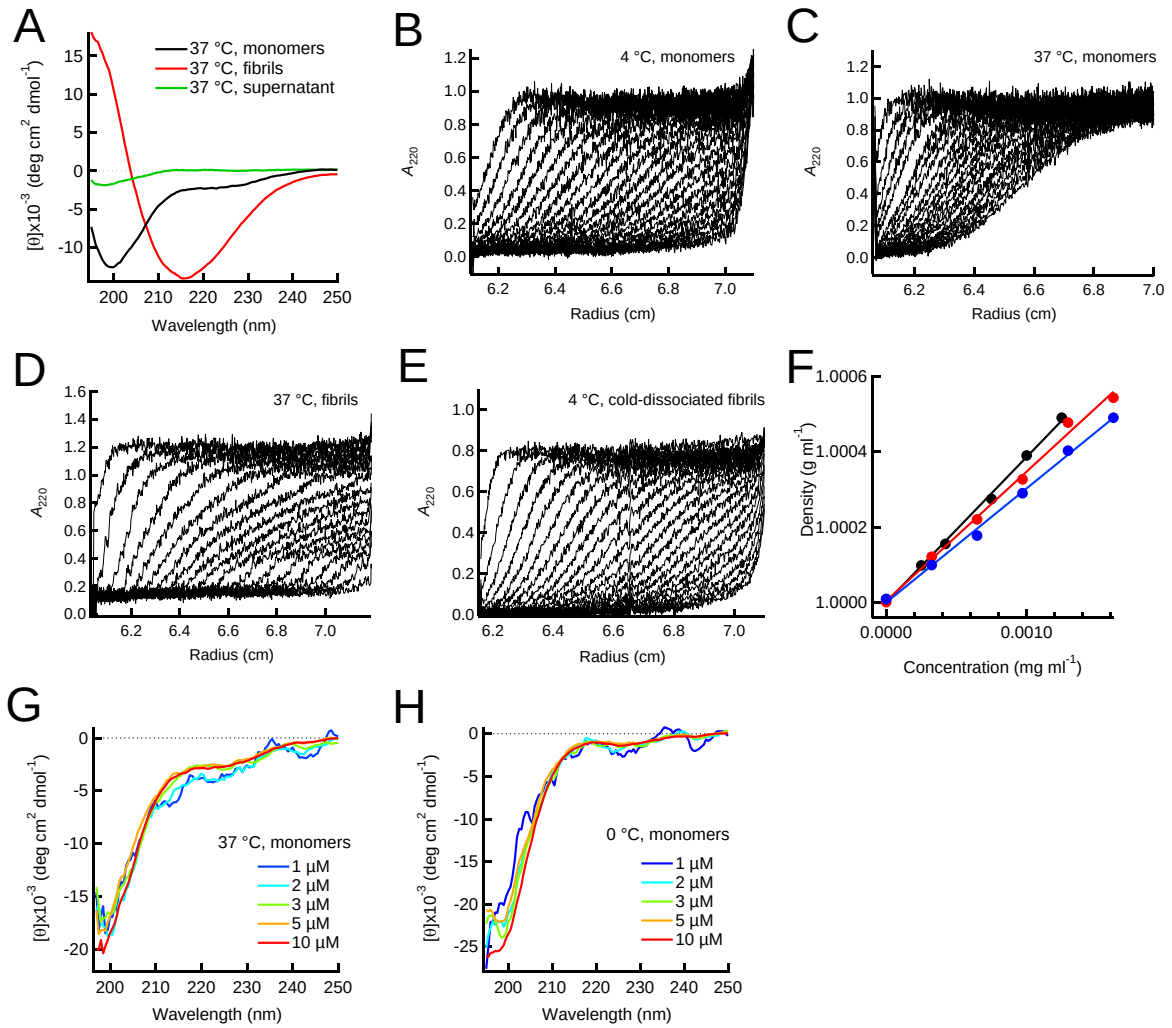

Fig. S1. Fibril Formation and Residual Monomers of αSN at pH 7.5. Far-UV CD spectra of αSN monomers (black), fibrils (red) formed in the presence of fibril seeds under sonication, and the supernatant after ultracentrifugation of the fibril solution (green). (B-E) Sedimentation velocity measurements conducted for αSN monomers at 4 (282,000*g*) (B) and 37 °C (237,000*g*) (C) and for fibril solutions at 37 (7,830*g*) (D) and 4 °C (282,000*g*) after an incubation of 17 h at 0 °C (E). (F) Density of αSN monomers plotted against protein concentrations. The three data sets conducted independently are shown by different colors. The straight lines indicate the linear fitting (see Supplemental Experimental Procedures). (G and H) Far-UV CD spectra of monomers at 37 (G) and 0 °C (H) at various protein concentrations.

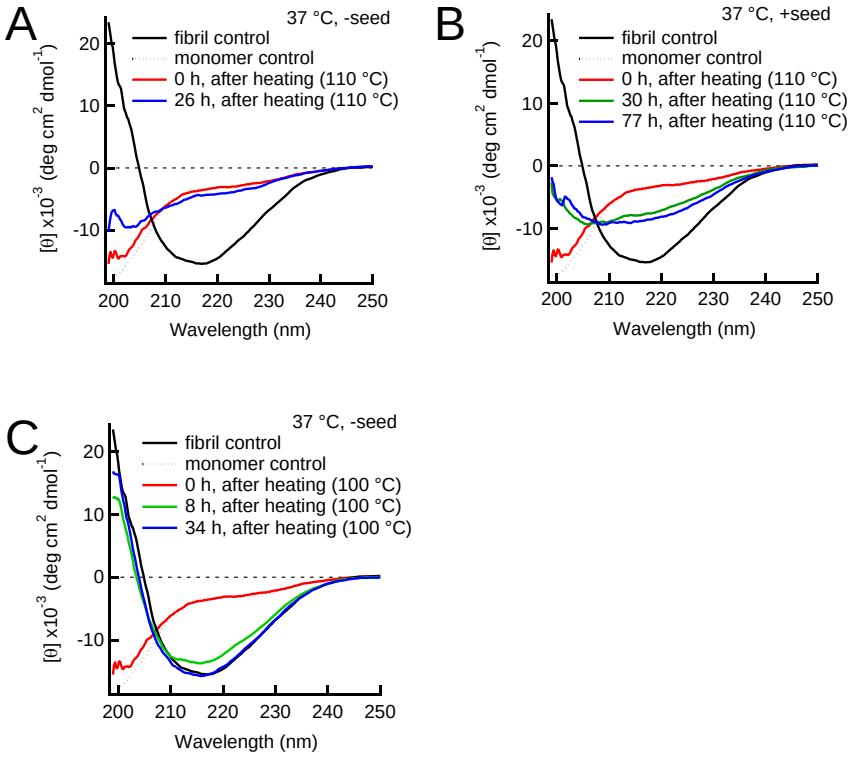

Fig. S2. Reversibility of the Heat Denaturation of αSN Fibrils. (A-C) Reversibility after the heat scan to 110 (A and B) and 100 °C (C). Far-UV CD spectra of fibrils at 37 °C before (black solid) and after (red, green, and blue solid) the heat treatment. The spectrum of monomers at 37 °C (black dotted) is shown. To observe the reformation of fibrils, samples subjected to the heat treatment were incubated at 37 °C for various periods in the absence (A and C) and presence (B) of fibril seeds.

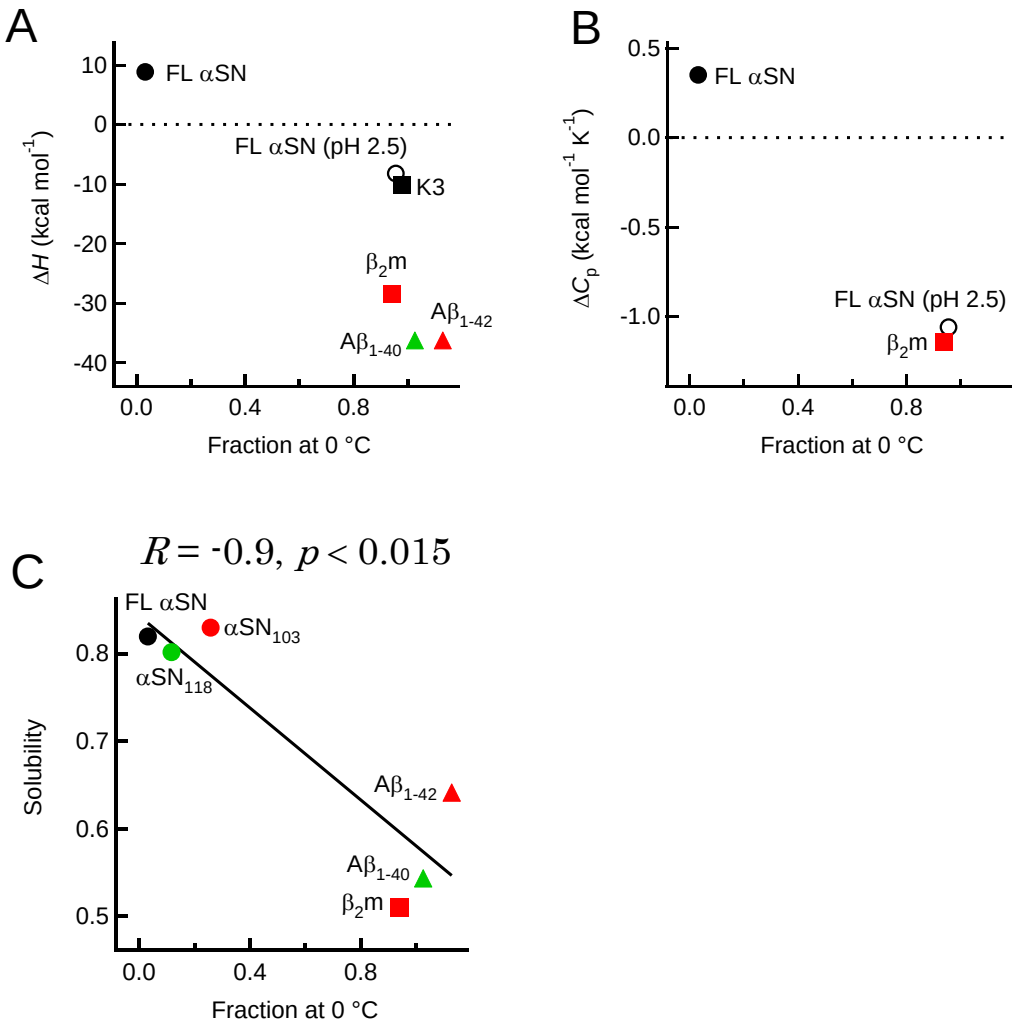

Fig. S3. Correlation of the Cold Denaturation of Fibrils with Thermodynamic and Physicochemical Factors. (A and B) The ΔH (A) and ΔC_p (B) values for fibril extension, directly measured by ITC, were plotted against the remaining fraction of fibrils at 0 °C. (C) The "solubility" of amyloidogenic monomers, calculated using SOLpro (http://scratch.proteomics.ics.uci.edu/explanation.html#SOLpro) (124), was plotted against the remaining fraction of fibrils at 0 °C. A correlation coefficient (R) and p value are shown.

Supplemental Tables

Table S1. Kinetics of cold denaturation of 10 μM αSN at 100 mM NaCl under various conditions.

Condition of denaturation	Temp(˚C)	k_1 (h^{-1})	A_1	k_2 (h^{-1})	A_2
Sonication*	0	5.29±0.75	-2680±240	0.70±0.04	-5270±210
Stirring*		1.00±0.13	-2590±250	0.16±0.02	-2710±220
Sonication**	5	1.42****	-7600±670	0.06****	-5670±1220
Stirring**		2.08****	-4910±370	0.07****	-3450±760
100 μM αSN***		3.39±1.72	-2290±480	0.10±0.17	-2600±2160
300 mM NaCl***		3.45±1.31	-1900±330	0.22±0.03	-7750±230
Temperature dependence	0	9.51±0.14	-9580±70	0.93±0.03	-2340±50
	10	6.69±0.13	-6020±60	0.70±0.02	-2800±40
	15	4.90±0.13	-2030±30	0.51±0.01	-2310±20
	25	15.26±2.87	-440±40	0.62±0.05	-760±20
Gdn-HCl 1 M	0	5.72±0.20	-8000±230	0.79±0.15	-3490±90
Gdn-HCl 2 M		15.97±1.22	-5340±360	3.67±0.69	-1920±360
Gdn-HCl 3 M		32.73±2.94	-3240±140	2.37±3.15	-210±70
Gdn-HCl 4 M		44****	-2780****	42****	-270****

*Fibrils formed under distinct agitation.

**Sonication or stirring treatment during cold denaturation.

***Cold denaturation of 100 μM αSN at 100 mM NaCl and 10 μM αSN at 300 mM NaCl.

****Meaningless error values too small or large are omitted.

Table S2. Various parameters of heat and chemical denaturations of fibrils.

	Heat Denaturation		Gdn-HCl Denaturation		
Precursor protein/peptide	T_m* (˚C) CD	C_m* (M) ThT	*m* value* (kJ mol^{-1} M^{-1}) ThT	C_m* (M) CD	*m* value* (kJ mol^{-1} M^{-1}) CD
FL αSN (pH 7.5) **	90.7±0.1	0.87	9.08	0.94	15.07
$αSN_{103}$	97.3±0.1	1.65	7.26	1.26	6.34
$αSN_{118}$	65.8±0.1	1.90	15.71	1.15	7.03
NAC_{76-96}	63.7±1.5	1.67	9.76	0.58	9.25
MF $β_2$m**	99.7±1.5	4.19	9.69	4.21	14.33
IF $β_2$m**	72.9±0.2	2.21	5.86	2.07	3.52
K3	72.7±0.5	2.40	5.44	2.43	4.20
$Aβ_{1-42}$ (pH 7.5)	-***	2.61	2.12	-***	-***
$Aβ_{1-40}$ (pH 7.4)	86.7±0.1	4.17	2.19	-***	-***
FL αSN (pH2.5) **	71.5±0.4	-***	-***	-***	-***
FL αSN 300 mM NaCl ****	73.0±0.1	-***	-***	-***	-***
Native $β_2$m	64.2†	-***	-***	2.0†	13.20†

*Data obtained by far-UV CD spectra or ThT assay.

**″FL″, ″MF″, ″IF″ indicate a full-length protein, mature fibrils, immature fibrils, respectively.

***″-″ indicates that the measurements were not performed or non applicable.

****αSN fibrils prepared in the presence of 300 mM NaCl.

†Data was taken from previous study (105), (77).

Table S3. Thermodynamic parameters of fibril extension obtained by ITC.

Temperature	ΔH (kcal mol^{-1})	Temperature	ΔH (kcal mol^{-1})
αSN		β_2m**	
33 ˚C	7.6	26 ˚C	-13.7
37 ˚C	8.8	30 ˚C	-20.6
41 ˚C	10.2	34 ˚C	-23.1
44 ˚C	11.5	37 ˚C	-28.5 (-41.8***)
ΔC_p = +0.35 kcal mol^{-1} K^{-1} (-2.3 kcal mol^{-1} K^{-1})*		40 ˚C	-29.5
		43 ˚C	-34.7
αSN (pH 2.5)		47 ˚C	-37.4
31 ˚C	-2.21	50 ˚C	-42.5
34 °C	-4.98	ΔC_p = -1.14 kcal mol^{-1} K^{-1} (-1.34 kcal mol^{-1} K^{-1})*** (-1.56 kcal mol^{-1} K^{-1})*	
37 °C	-8.21		
40 °C	-11.23		
43 °C	-14.80	Aβ$_{1-40}$	
ΔC_p= -1.06 kcal mol^{-1} K^{-1}		37 ˚C	-36.8
		K3	
		37 ˚C	-10.2

*The data taken from previous study (105).

**The ΔH and ΔC_p value of folding reaction of native β_2m taken from (105).

***The values were calculated using statistical relations (see Supplementary Section S7).

Table S4. Core regions of various amyloid fibrils.

Protein or peptide	Reference	Core region	Method
αSN fibrils	(126)	39–101	H/D exchange with MS*
	(127)	35–96 30–110	H/D exchange with NMR** solid-state NMR
	(128)	32-102	Proteolysis
	(106)	76-96	Proteolysis
	(129)	38–95	solid-state NMR
	(130)	39-98	solid-state NMR
	(131)	38-97	solid-state NMR
	(132)	38-96	solid-state NMR
	(133)	35-100	EPR***
Mature β2m fibril	(134)	27–86	MAS NMR****
	(135)	21-87	H/D exchange with NMR**
Immature β2m fibril	(135)	37-47 and 60-70	H/D exchange with NMR**
K3 fibrils	(136)	21-28 and 33-40	solid-state NMR
$A\beta_{1-42}$ fibrils	(9)	18-26 and 31-42	H/D exchange with NMR**
$A\beta_{1-40}$ fibrils	(10)	11-22 and 30-39	solid-state NMR

*Hydrogen-deuterium exchange method with mass spectrometry.

**Hydrogen-deuterium exchange method with solution-state NMR spectroscopy.

***Electron paramagnetic resonance spectroscopy.

****Magic angle spinning NMR spectroscopy.

Chapter 3. Heat of supersaturation-limited amyloid burst directly monitored by isothermal titration calorimetry

3-1. Introduction

Aggregation has often been an obstacle to studying the structure, function, and physical properties of proteins. However, a large number of aggregates associated with serious diseases**,** including Alzheimer's, Parkinson's, and prion diseases (1, 137) promoted the challenge of studying protein misfolding and aggregation. Researchers succeeded in distinguishing amyloid fibrils and oligomers from other amorphous aggregates and characterized the ordered structures present in amyloid fibrils or oligomers, which led to the development of the field of amyloid structural biology (32, 82, 92, 138-140). These advances have been attributed to various methodologies that are also useful for studying the structural properties of globular proteins. Even X-ray crystallography has become a powerful approach for studying amyloid microcrystals (92) or oligomers (141). The atomic details of amyloid fibrils are becoming increasingly clearer, and a cross-β structure was shown to be the main structural component of fibrils (92, 139, 140). Although tightly packed core regions of amyloid fibrils have been reported, the overall structures were shown to be dominated by common cross-β structures, which supported the argument for the main-chain dominated architecture in contrast to the side-chain dominated architecture of globular native states (101, 102, 142).

These structural studies have been complemented by a series of efforts to clarify the mechanism for the formation of amyloid fibrils (i.e., amyloid fibrillation). The presence of a long lag time in spontaneous fibrillation and rapid fibrillation by the addition of preformed fibrils represent a similarity with the supersaturation-limited crystallization of substances (35, 84, 143-146). I have revisited "supersaturation" and argued its critical role for amyloid fibrillation (79, 145, 146). The role of supersaturation in neurodegenerative diseases at the proteome level has been reported recently (147).

On the other hand, calorimetry, one of the most powerful methods used to study the thermodynamic properties of globular proteins (108, 148-150), has not played a significant role in understanding protein aggregation. The aggregation of proteins following heat denaturation as monitored by differential scanning calorimetry is an infamous example demonstrating how aggregation can prevent exact analyses (151, 152). To date, few studies have investigated protein aggregation including amyloid fibrils with calorimetry (105, 122, 153-156). Previous study on the exothermic heat effects accompanying fibril

growth was achieved by monitoring the seed-dependent elongation of fibrils formed by β2m, a protein responsible for dialysis-related amyloidosis, using ITC (105).

In the present study using β2m, I succeeded in characterizing the total heat of spontaneous fibrillation and amorphous aggregation. An analysis of the heat burst associated with fibrillation or amorphous aggregation under various temperatures clarified their thermodynamic properties. The results obtained enabled the calorimetric characterization of amyloid fibrils and amorphous aggregates relative to that of the native globular structures, which opens a new field for the calorimetric study of protein aggregates.

3-2. Materials and Methods

Assays of Amyloid Fibrils. Expression and purification of human β2m was described in *SI Text*. The formation of fibrils and amorphous aggregates was characterized by various methods including ThT fluorescence, AFM, CD, and enzyme-linked immunosorbent assays. The details are described in *SI Text*.

ITC Measurements. ITC measurements for the spontaneous fibrillization of β2m at 0.3–6.7 mg ml^{-1} dissolved in 10 mM HCl solution (pH 2.5) were performed with a VP-ITC instrument (GE Healthcare, MA, USA) at the desired temperatures (31-43 °C). The consecutive injections of 20 μl of the 10 mM HCl solution containing 1 M NaCl in the syringe into the β2m solution in the cell were conducted following a 60 min-initial delay for complete equilibration. To minimize the heat effects caused by the difference in temperature, the consecutive injections were required because the temperature of the solution inside injection syringe was not controlled except 20 μl in the needle. The first titration of 2 μl was adopted to minimize the influence of residual bubbles and imperfect solution filling the syringe. Nine salt titrations in total, spaced at intervals of 900 s, were performed with a duration of 4 s for the first titration and 40 s for the others to reach the final NaCl concentration of 100 mM. Changes in the heat flow in μcal s^{-1} were monitored in real time with 10 μcal s^{-1} of reference power. The reaction cell was continuously stirred at 600 rpm. Lag time was defined by a period between the time starting the measurement under stirring and the time of major heat effect occurred as shown in Fig. 3*A*. To examine the effects of the stirring speed on fibrillation, the stirring speed was changed from 200 to 1000 rpm. To monitor amorphous aggregation, 3.5 mg ml^{-1} of β2m in 10 mM HCl solution without salt was inversely titrated into 10 mM HCl solution containing 1.0 M NaCl at the desired temperatures (31-43 °C). The parameters for ITC measurements except for shortening the initial delay to 30 min were identical to those used for fibril formation. The total heat effects, which were shown to be equal to the ΔH values, were calculated using peak areas after subtracting the heat of dilution and baseline corrections.

3-3. Results

Heat for the Formation of Amyloid Fibrils Monitored by ITC. At pH 2.5, acid-denatured β2m formed amyloid fibrils in the presence of moderate concentrations of NaCl. As defined by the conformation phase diagram, fibril formation is dependent on protein and NaCl concentrations (Fig. 1) (79, 157). Spontaneous fibrillation was previously shown to be facilitated by various kinds of agitations such as stirring with a magnetic bar (158, 159) or ultrasonication (79, 160-163), leading to a burst phase of fibrillation after a lag phase. Under the conditions of persistent metastability of supersaturation, it is likely that these agitations may create seed-competent conformations. For instance, during air-water interface-dependent protein aggregation a template-competent conformation is formed (163).

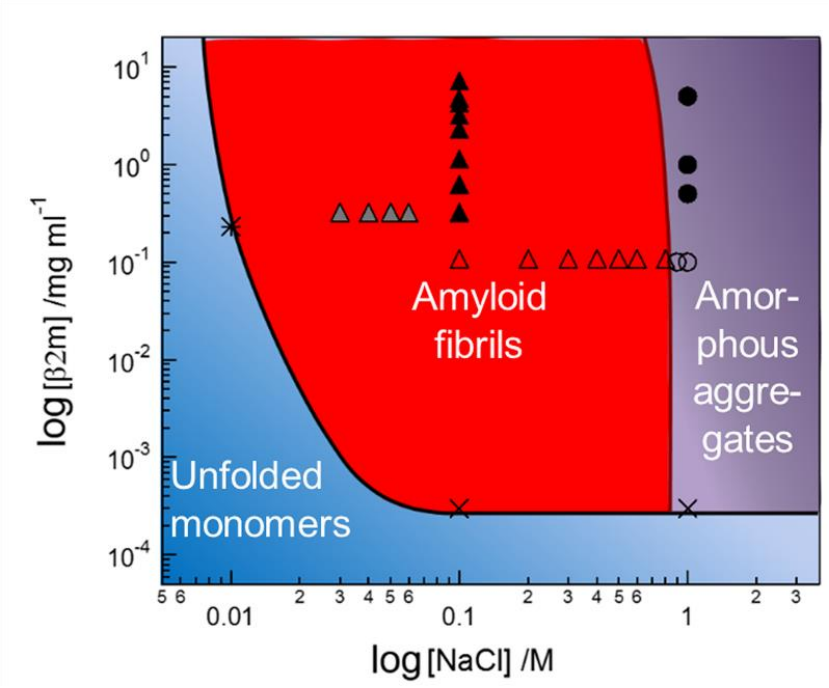

Fig. 1. Conformation phase diagram of β2m at 37 °C and pH 2.5. The regions of unfolded monomers (blue), amyloid fibrils (red), and amorphous aggregates (magenta) are shown. Conformational states were determined in this study (▲, ●, X) and also in previous studies (gray triangle △, ○, ∗)(79, 157). Lines are boundaries between the phases. The boundary between the unfolded soluble states and amyloid fibrils defines the critical concentration, which is equal to the equilibrium solubility of unfolded monomers. The critical concentrations from this study (X) and previous study (∗)(157).

In my studies, I used the ITC instrument to agitate the β2m solution and monitor the heat response of fibrillation. To establish supersaturation in the presence of various concentrations of β2m at pH 2.5 in the cell at 37 °C, the NaCl concentration was increased to a final value of 0.1 M by stepwise injections of a small volume of 1.0 M NaCl (Fig. 2*A*, see Methods). After each injection, a sharp endothermic or exothermic spike, which represented the heat (q) of salt dilution, occurred and the heat flow ($= \partial q/\partial t$) returned back to the original reference power level. Notably, a marked exothermic peak with a half width of ~2 h occurred at 0.3 mg ml^{-1} of β2m at ~11 h (Fig. 2*A*). Similar exothermic peaks were observed at other concentrations of β2m. The lag time for the major exothermic peak (Materials and Methods) shortened (Fig. S1*A*) and the exothermic peak became larger with an increase in the protein concentration. When 0.5 mg ml^{-1} of the β2m solution at 0.1 M NaCl was prepared in a test tube, set in the ITC cell, and followed by stirring, a similar exothermic burst with a lag time of 3.7 h was observed (Fig. S2). When I consider the time for titration of salt (3.5 hr, see Fig. 4*A* below), the observed lag time was independent of the methods, although the titration in the ITC cell was much simpler. The results suggested that the titration inside the ITC cell did not bring any additional effects.

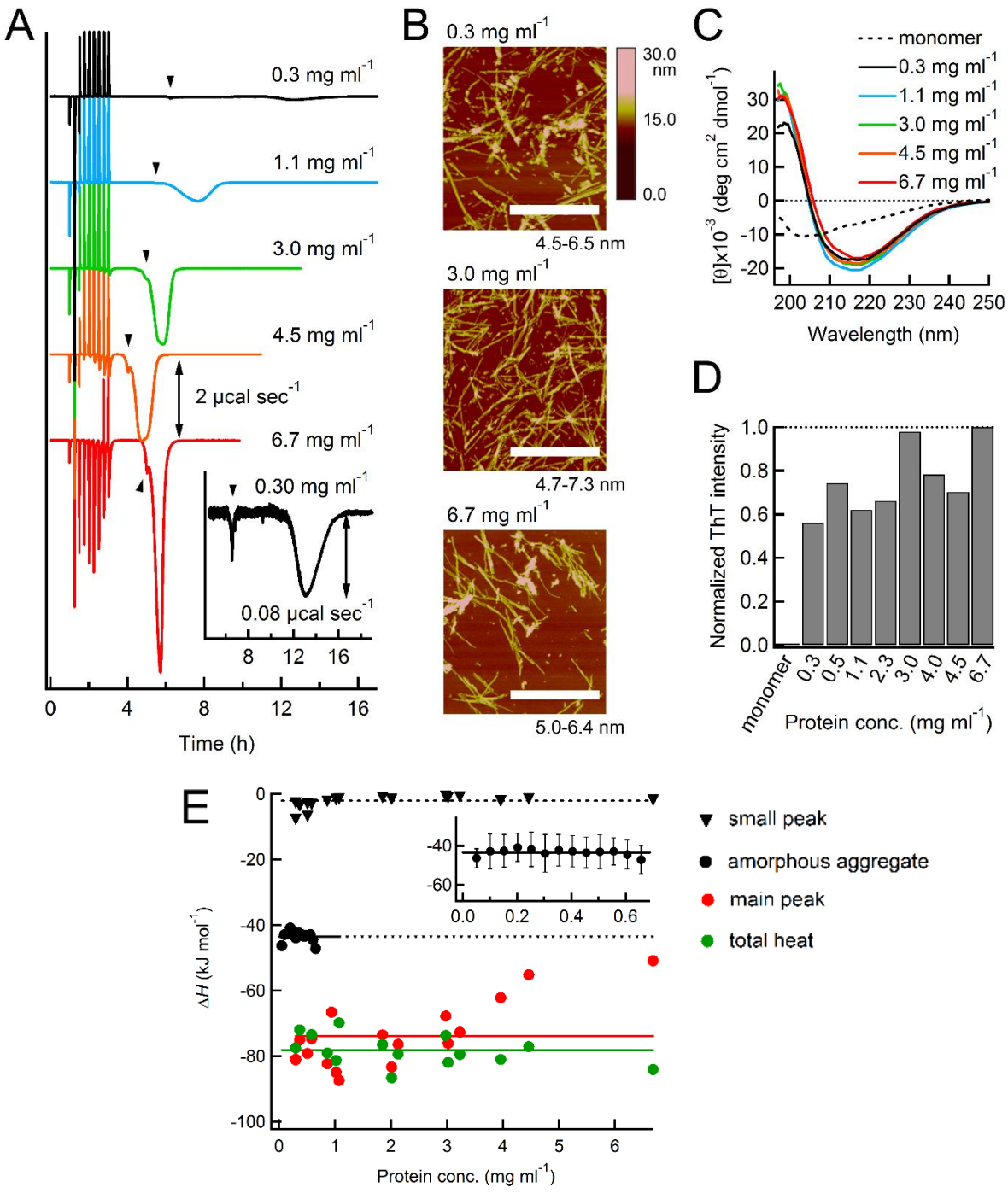

Fig. 2. Calorimetric observation of the amyloid burst of β2m at various protein concentrations at 37 °C. (*A*) Thermograms of the fibril formation of β2m at 0.3–6.7 mg ml^{-1} and pH 2.5 obtained using ITC. The inset shows a close-up view of exothermic heat at 0.3 mg ml^{-1} of β2m. The arrowheads indicate the locations of "small burst". These also apply to the thermograms of Figs. 3, 4, and 6. (*B-D*) Characterization of β2m solutions after incubation in ITC cells by AFM images (*B*), far-UV CD spectra (*C*), and ThT fluorescence intensities (*D*). The scale bars on the AFM images indicate 1 μm and the numbers under images are fibril height. The scale bar on the right represents the height. These also apply to AFM images in Figs. 4-6. (*E*) Dependences of the

observed heat of the small peak (black inverted triangle), main peak (red circles), total heat including rapid heat effect (green circle), and amorphous aggregation (black circles) on the protein concentration. Inset in *C* shows the expansion of the heat of amorphous aggregation. The observed heats were normalized by the β2m concentration to give the ΔH values.

The total heat calculated based on the peak area was normalized by the protein concentration. The normalized heat did not depend significantly on the protein concentration (Fig. 2*E*). Moreover, when the stirring speed was varied in the range of 200-1000 rpm with a fixed protein concentration of 0.5 mg ml^{-1}, the lag time shortened with an increase in the speed (Fig. 3*A* and Fig. S1*B*). However, the total heat was independent of the stirring speed (Fig. 3*B*). These results suggested that the observed heat represented the enthalpy change (ΔH) of the reaction triggered by stirring. Assuming that the observed total heat was ΔH, the ΔH value at 37 °C was estimated to be -77 kJ mol^{-1} from the dependence on stirring speed or -74 kJ mol^{-1} from the dependence on protein concentration. The decrease in magnitude of ΔH at high protein concentrations may have been linked with the partial and transient formation of amorphous aggregates with a smaller ΔH value (see below).

After the exothermic peaks, all β2m solutions exhibited a far-UV CD spectrum with a minimum at approximately 218 nm, an AFM image of fibrils with a height of 4.5-9.0 nm and various lengths up to 1 μm, and strong ThT fluorescence (Fig. 2*B-D*). These results indicated that β2m solutions above 0.3 mg ml^{-1} in 0.1 M NaCl at pH 2.5 were supersaturated (or metastable) and that agitation by stirring broke this supersaturation, resulting in amyloid fibrillation. I consider that the exothermic peak represents the formation of amyloid fibrils (″amyloid burst″) and the observed heat gives its ΔH value. Similar effects were expected for other salts, the effectiveness of which follows the electroselectivity series (79, 157). One experiment with ammonium sulfate was shown in Fig. S3.

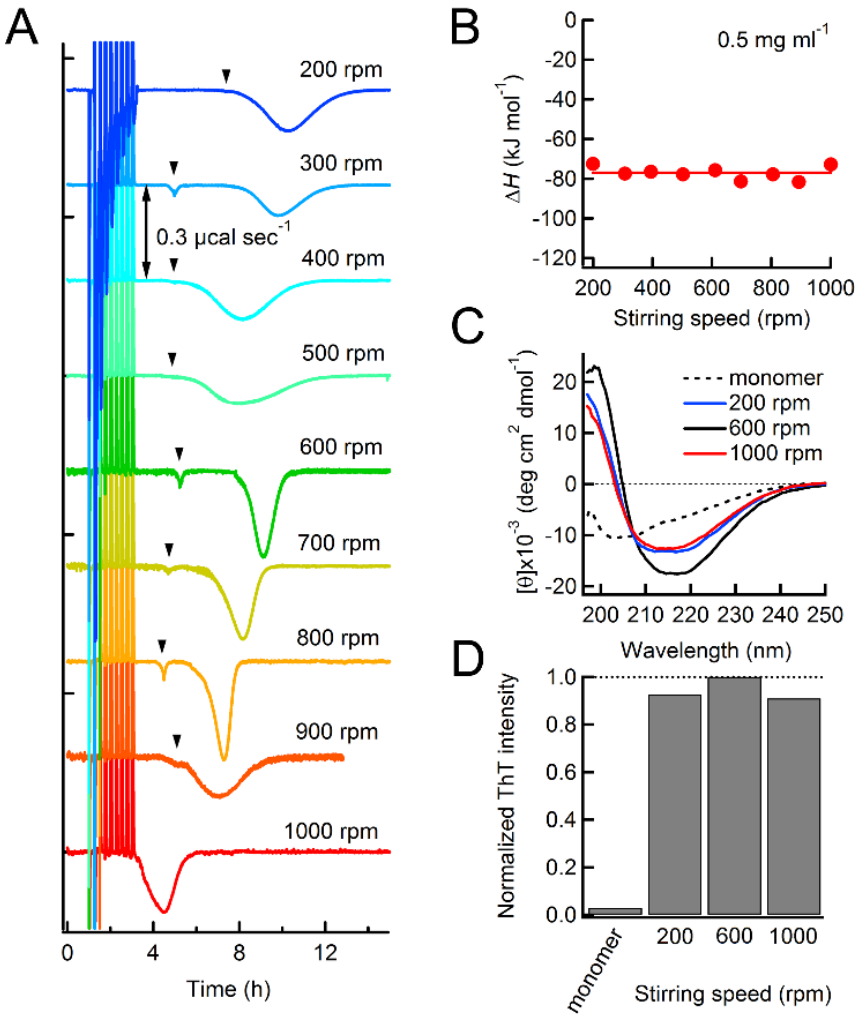

Fig. 3. Dependencies of the observed heat of aggregation on the stirring speed at pH 2.5 and 37 °C. (*A*) Thermograms of the fibril formation of β2m at 0.5 mg ml^{-1} at various stirring speeds. The arrowheads indicate the locations of "small burst". (*B*) Dependence on the stirring speed of the observed heat normalized by the protein concentration. (*C, D*) Characterization of β2m solutions after incubation in ITC cells by far-UV CD spectra (*C*) and ThT fluorescence intensities (*D*).

Small Amyloid Burst and Excess Heat Immediately after Salt-Titration. Careful inspection of the ITC thermograms indicated that, in all the ITC profiles, a small exothermic peak, which I designated ″small amyloid burst″, appeared before the main amyloid burst (Figs. 2*A*, 3*A*, and 6*A*). To clarify the significance of these small peaks, I performed CD and AFM measurements and a ThT assay at several time points during the reaction at 1.0 mg ml^{-1} β2m (Fig. 4*B, C*). Neither the CD spectrum nor the AFM image showed significant changes before and immediately after the salt-injection spikes, which indicated that the dominant molecular species were still monomers. When the small exothermic

peak appeared at the ~5.5 h time point, the AFM image revealed the presence of short and thin fibrils with a height of 2.6-5.3 nm. A slight change in the CD spectrum and small increase in ThT fluorescence were also observed. These results indicated that some fibrillation, possibly the formation of protofibrils, started at the point of the small burst, and subsequent elongation coupled with the breakage of fibrils to make new growing ends (i.e., secondary nucleation) caused the explosive amyloid burst (Fig. 4*B*, and *C*). The exact position and size of the minor peaks were less dependent on the experimental conditions than those of the major peaks (Figs. 2*A*, 3*A*, 6*A* and S1). The total heat accompanying the small exothermic peak was constant (-1.5 kJ mol^{-1}) and independent of the protein concentration (Fig. 2*E*). Although the observed heat contained information on the ΔH value of protofibril formation, its small fraction precludes further analysis.

I also recognized a small excess heat effect immediately after each of the stepwise addition of 1.0 M NaCl (Fig. S4). This small but notable heat effect increased with an increase in the concentration of NaCl and β2m, suggesting that it represents the formation of amorphous aggregates. However, after the completion of major amyloid burst, the formation of amorphous aggregates was evident neither from the CD spectra, ThT intensities, nor AFM images (Fig. 2*B-D*). Thus, it is possible that a small amount of amorphous aggregates formed after the salt injection finally transformed to the fibrils, although the exact kinetics is unknown. If this is a case, a total heat including those of rapid heat effect, small amyloid burst and major amyloid burst should represent the ΔH value for amyloid fibrillation. Indeed, the sum of these heat effects was constant (-78 kJ mol^{-1}) over a wide range of concentration, suggesting the validity of assumption (Fig. 2*E*).

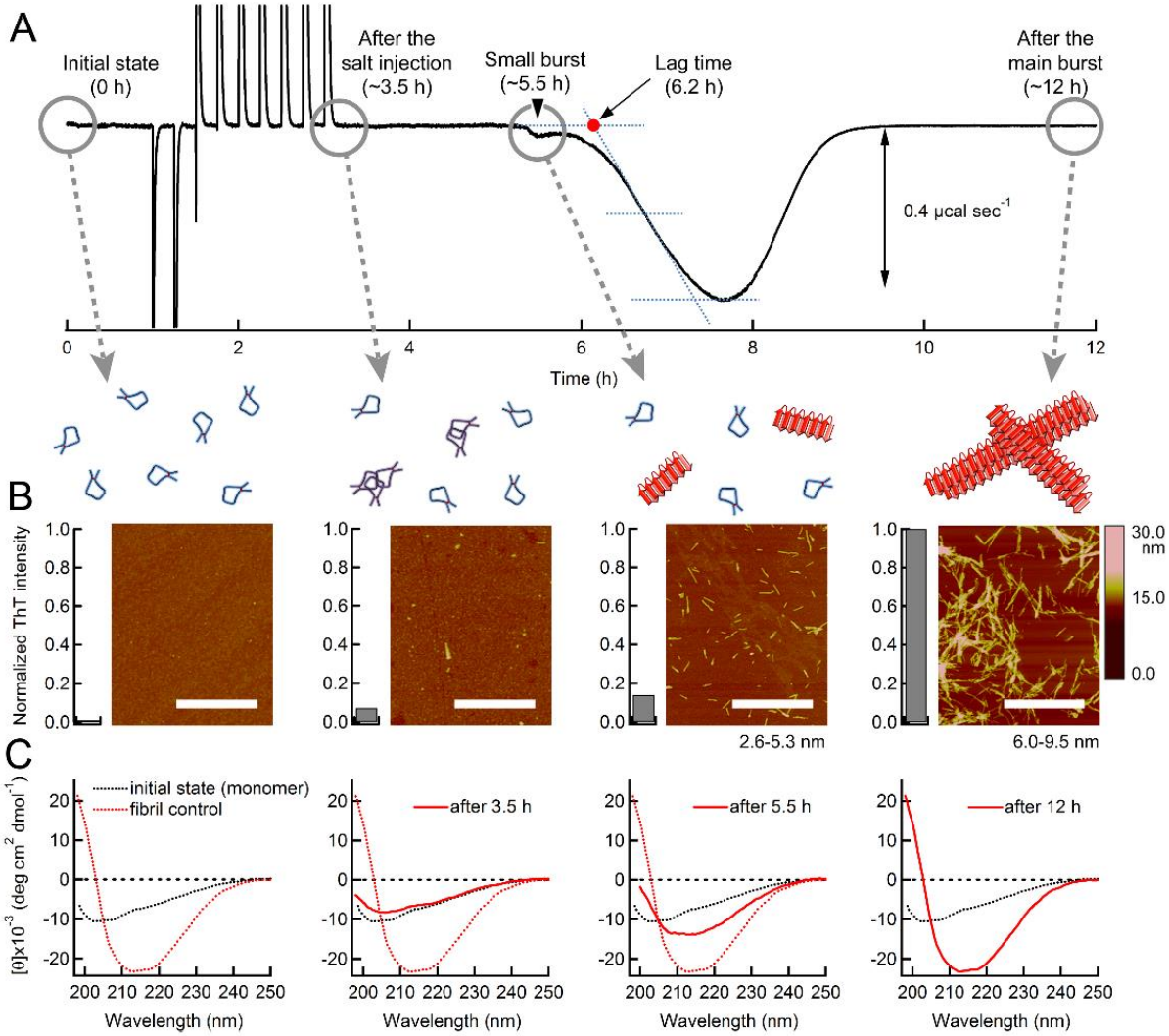

Fig. 4. Monitoring the kinetics of the amyloid burst of β2m using various approaches. (A) ITC profile of 1.1 mg ml^{-1} β2m at pH 2.5 and 37 °C. The lag time (red dot) is determined by a baseline and a tangent line at the middle of the major peak. (*B, C*) Conformational changes in β2m during incubation in an ITC cell characterized using AFM images and ThT fluorescence intensities (*B*) and the far-UV CD spectra (*C*) at the four time points: "Initial state (0 h)", "After salt injection (~3.5 h)", "Small burst (~5.5 h)", and "After main burst (~12 h)". Conformations of β2m based on AFM, ThT fluorescence, and CD are illustrated above the AFM images: monomers (blue curves), oligomers (magenta curves), and fibrils (red rectangles). The CD spectra at the respective time points are shown by red solid curves. The spectra of monomers (black dotted curves) and mature fibrils (red dotted curves) are shown for comparison.

Heat of Amorphous Aggregation. β2m formed amorphous aggregates at very high NaCl concentrations above 0.8 M at pH 2.5 (Fig. 1) (79). In analogy with the crystallization of substances, amyloid fibrils and amorphous aggregates were shown to be similar to crystals and glasses, respectively (79). In Yoshimura *et al*. (79), they showed that, while crystalline amyloid fibrils formed after a lag phase, glassy amorphous aggregates formed without a lag phase. The rapid and partial formation of amorphous aggregates after the salt titration was consistent with this view (Fig. S4).

It was difficult to increase the NaCl concentration in the cell up to approximately 1.0 M by injecting the NaCl solution at a high concentration in the syringe. Thus, I performed an inverse titration: the β2m solution at a high concentration in the syringe was injected into the cell containing 1.0 M NaCl (Fig. 5). On the bases of the low CD signal, amorphous aggregates revealed by the AFM image, and low ThT fluorescence, I confirmed that β2m formed amorphous aggregates. There was no lag phase in amorphous aggregation, which was consistent with previous results (79). Careful subtraction of the heat for the control experiment revealed the heat of amorphous aggregation. At 37 °C, the control heat effect without β2m was ~1,250 μcal, while that of β2 was around ~1,190 μcal, with the excess heat of aggregation around ~5% of the basal heat effects. Again, there was no protein concentration dependence in the range of 0.1-0.7 mg ml^{-1}, which suggested that the heats represented the ΔH of amorphous aggregation (Fig. 5*B*). The ΔH value for amorphous aggregation was estimated to be -43 kJ mol^{-1} at 37 °C and assumed to be independent of the protein concentration as indicated by the dotted line in Fig. 2*E*.

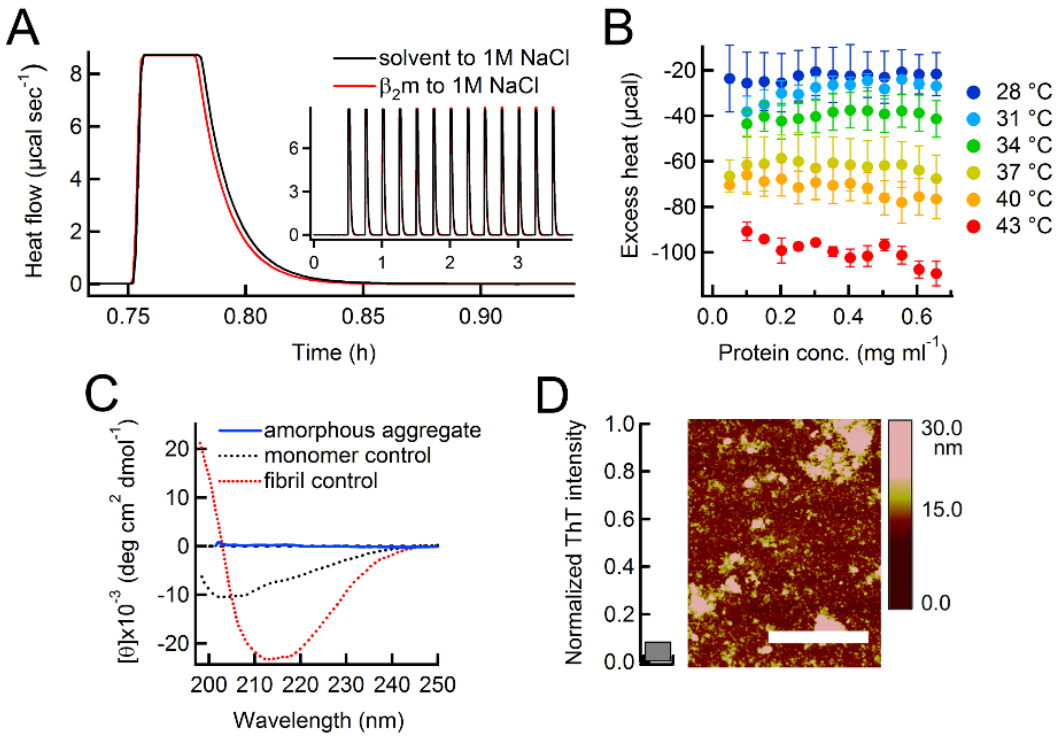

Fig. 5. Calorimetric observation of amorphous aggregation of β2m at 37 °C. (*A*) Thermogram of amorphous aggregation revealed by titrating 1.0 M NaCl in the ITC cell with 3.6 mg ml^{-1} β2m (red) or solvent (black) in the syringe. Titration was repeated 13 times to increase the β2m concentration. The expanded thermogram shows the second titration peak. (*B*) After subtracting the control, the excess heat was plotted against the final β2m concentration. The results of measurements at various temperatures are shown. (*C, D*) CD spectrum, ThT fluorescence intensity, and AFM image of the amorphous aggregates formed in the ITC cell at 1.0 M NaCl. CD spectra of fibrils and monomers are also shown.

Temperature Dependency of Aggregation Heat. ITC measurements of the amyloid burst at 1.0 mg ml^{-1} were performed at various temperatures between 31-43 ºC (Fig. 6*A*). The lag time shortened (Fig. S1*C*) and the exothermic peak became larger with an increase in temperature. The ΔH value increased in magnitude from -41.3 to -101.1 kJ mol^{-1} (Fig. 7*A* and Table S1). I confirmed using far-UV CD, AFM, and ThT assays that the products observed after heat burst at all the temperatures were amyloid fibrils (Fig. 6*B-D*).

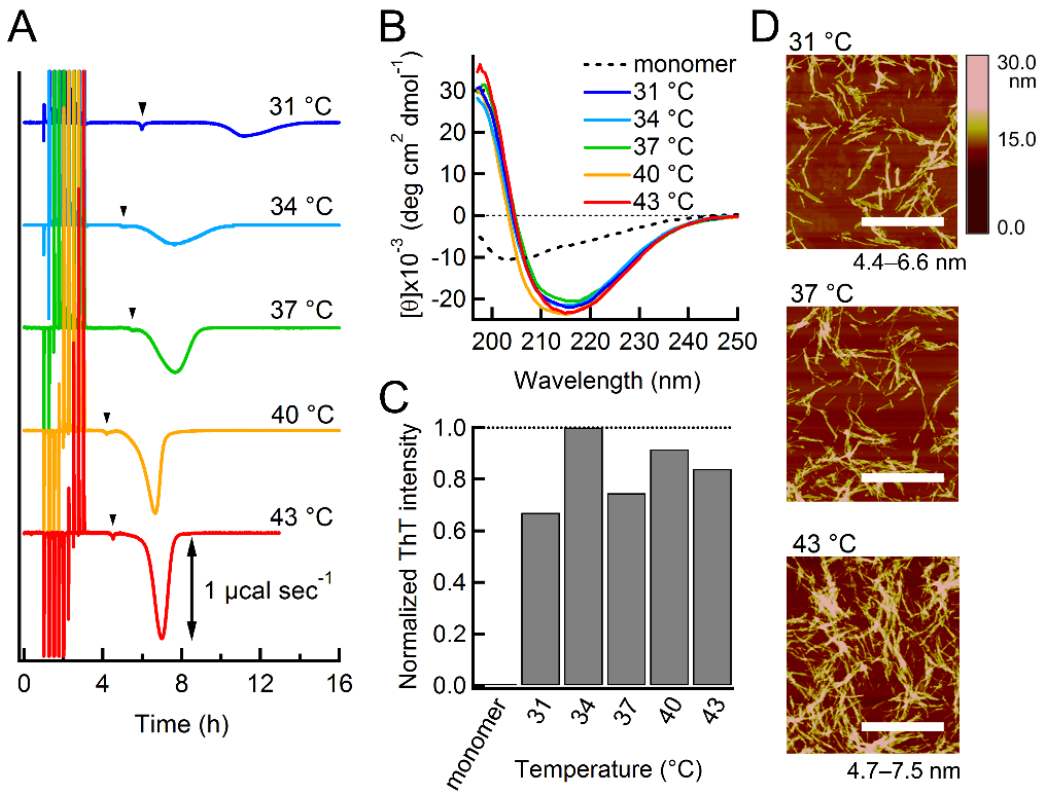

Fig. 6. Temperature-dependence of the amyloid burst of β2m monitored by calorimetry. (*A*) Thermograms at various temperatures between 31 to 43 °C. The arrowheads indicate the locations of "small burst". (*B-D*) Characterization of the β2m solution at 1.1 mg ml^{-1} and 0.1 M NaCl after the heat burst by the far-UV CD (*B*), ThT fluorescence (*C*), and AFM (*D*).

Assuming that the observed heat effect represented ΔH, temperature dependence provided a heat capacity change (ΔC_p) of fibrillation based on the relationship of $\Delta C_p = \partial \Delta H / \partial T$. The plot of ΔH against temperature was linear, providing a ΔC_p value of -5.0 kJ mol^{-1}K^{-1} (Fig. 7*A* and Table S1). Kardos *et al.* previously obtained the ΔH value and temperature dependence for the seed-dependent elongation of amyloid fibrils of β2m monitored by ITC (105) (Fig. 7*A*). Although the ΔH values for the spontaneous fibrillation obtained here were slightly smaller than those of seed-dependent elongation, the current ΔC_p value was similar to that (-4.8 kJ mol^{-1}K^{-1}) of seed-dependent elongation (105).

I also measured temperature dependence of the heat effects of amorphous aggregation (Figs. 5*B*, 7*A* and Table S1). Although the ΔH values for amorphous aggregates at 1.0 M and various temperatures were smaller in intensity than those of mature fibrils, ΔH changed linearly against temperature, providing a ΔC_p value (-3.5 kJ mol^{-1}K^{-1}) that was slightly smaller than that of amyloid fibrils.

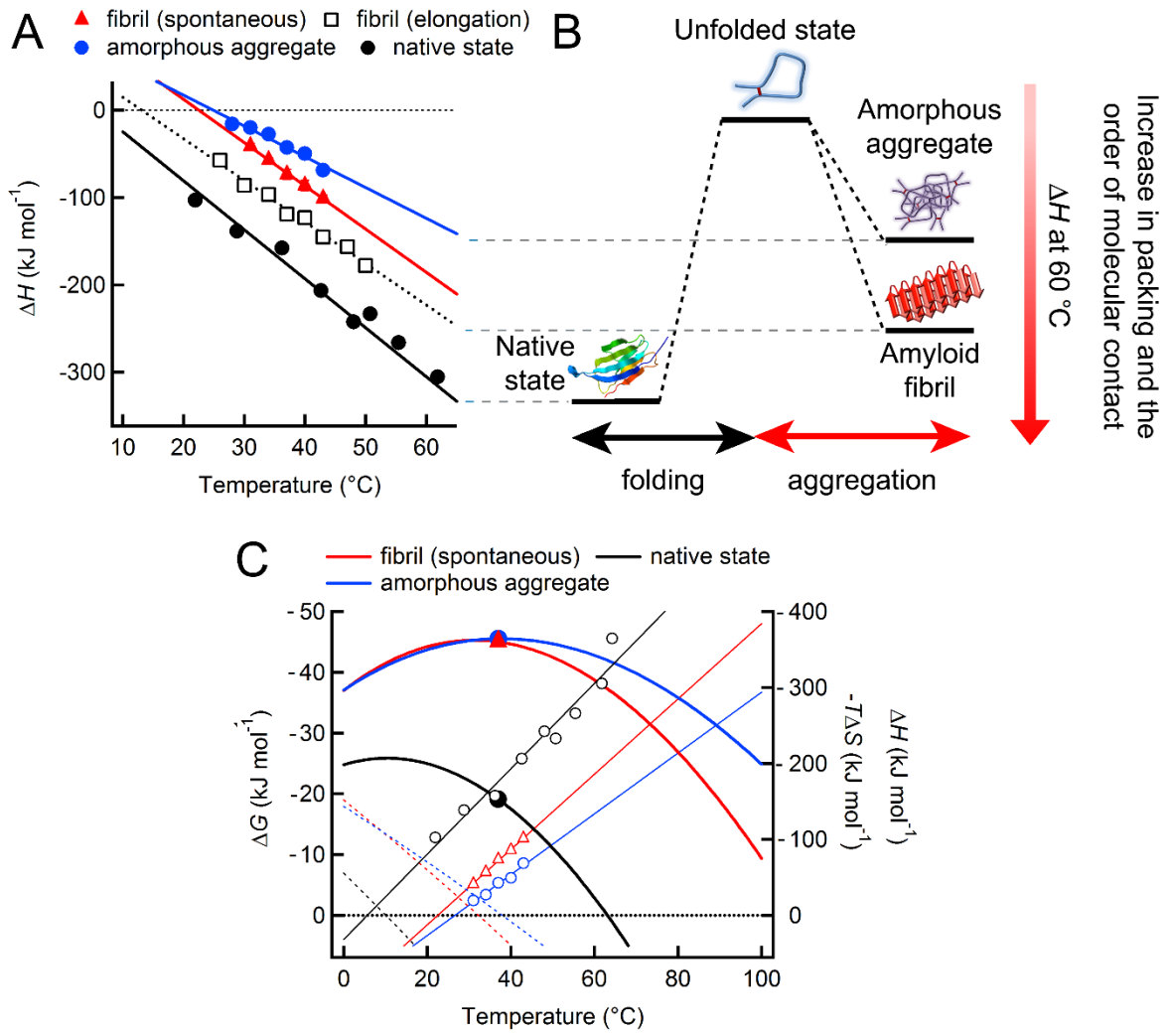

Fig. 7. Thermodynamic characterization of the folding and misfolding of β2m. (*A*) Temperature dependencies of Δ*H* for amorphous aggregation (blue circles), spontaneous (red triangles) and seed-dependent fibrillations (black squares), and folding (black circles). (*B*) The difference in Δ*H* at 60 °C among the different conformational states is illustrated. (*C*) Temperature dependencies of Δ*G* (curves), Δ*H* (solid straight lines), and -*T*Δ*S* (dotted straight lines) for folding to the native state (black lines and circles), spontaneous amyloid fibrillation (red lines and triangles), and amorphous aggregation (blue lines and circles). The Δ*G* values at 37 °C are shown with the closed symbols. The sign of the ordinate is opposite to that in *A* to compare the profiles with the standard profile of protein unfolding.

Evaluation of Thermodynamic Parameters. To comprehensively understand the thermodynamics of aggregation, I have to know the changes in free energy (Δ*G*) and entropy (Δ*S*) in addition to the Δ*H* and ΔC_p terms, which are directly determined by calorimetry (108). Although the detailed mechanical models of fibril formation remain elusive (144), a simplified model will still be valid for describing the

equilibrium between monomers (M) and fibrils (P) (35, 84, 105, 143):

$$(\mathrm{P}) + (\mathrm{M}) \underset{k_{-1}}{\overset{k_1}{\rightleftarrows}} (\mathrm{P}) \qquad (1)$$

where k_1 and k_{-1} are the apparent rate constants for polymerization and depolymerization, respectively. The elongation of fibrils is defined by the equilibrium association constant (K) as:

$$K = \frac{[P]}{[P][M]} = k_1 / k_{-1} \qquad (2)$$

where [P] is the concentration of fibrils and [M] is the concentration of monomers. The equilibrium is clearly independent of [P]. Hence, I obtain the equilibrium monomer concentration $[\mathrm{M}]_e$ as:

$$[\mathrm{M}]_e = k_{-1} / k_1 = 1/K \qquad (3)$$

$[\mathrm{M}]_e$ is referred to as the "critical concentration" (84, 143) because fibrils form when the concentration of monomers exceeds $[\mathrm{M}]_e$. By determining $[\mathrm{M}]_e$, I can calculate the apparent free energy change of fibrillation (ΔG_{app}) by: $\Delta G_{app} = -RT\ln K = RT\ln[\mathrm{M}]_e$, where R and T are the gas constant and temperature, respectively. Combined with the ΔH value directly obtained from the ITC measurements, I can obtain the ΔS value by $\Delta G_{app} = \Delta H - T\Delta S$. Although Mechanism 1 might not be exactly true for amorphous aggregation, I assumed that it is also a reversible process determined by solubility and thus is approximated by Mechanism 1.

I used an enzyme-linked immunosorbent assay (ELISA) (SI Text) to determine the $[\mathrm{M}]_e$ value under various conditions (Table S2). I then estimated the ΔG_{app} and $T\Delta S$ for fibrillation and amorphous aggregation. I also estimated the temperature dependencies of these parameters as well as those of ΔH, in which I used ΔG_{app} values at 37 ºC to link the ΔH and $T\Delta S$ functions. These functions were compared with those for folding to the native state (Fig. 7).

The ΔG_{app} value of fibrillation (-45.0 kJ mol^{-1}) at 37 ºC and pH 2.5 was the same as that of amorphous aggregation (-45.4 kJ mol^{-1}) under the same conditions (Fig. 7*C*). These values were significantly larger in intensity than that (-21.0 kJ mol^{-1}) of the native state at pH 7.0 (105), although distinct pH values preclude a direct comparison. Although a small range of temperatures used for the experiments makes the extrapolation less accurate at this stage, separation of ΔG_{app} into the enthalpy and entropy terms indicated that both amyloid fibrils and amorphous aggregates are stabilized enthalpically above 40 °C,

while they are stabilized entropically below 20 °C.

3-4. Discussion

Amyloid formation occurs in supersaturated solutions via a nucleation-dependent manner (146, 164, 165), analogous to crystallization of substances (145, 166). Under the conditions of persistent metastability, nucleation does not occur in practice (35, 146). However, various kinds of agitations can break supersaturation, leading to the formation of fibrils. I used ITC for stirring the solution and for monitoring the accompanying heat effects. The results showed that I can perform calorimetric measurements of amyloid fibrillation of β2m as well as amorphous aggregation revealing the ΔH and ΔC_p values. By combining these values with ΔG obtained from the solubility of β2m monomers, I can address the thermodynamics of protein aggregation (Fig. 7 and Tables S1 and S2). The methodology is straightforward and can be applied to study various amyloid fibrils as well as amorphous aggregates.

The heat capacity change upon protein unfolding has been primarily determined by the hydration of polar and apolar groups and to a much lesser extent by the disruption of internal noncovalent interactions such as van der Waals interactions, H-bonds, and ionic interactions (108, 148). Considering the morphological difference between the intramolecularly folded native state and intermolecularly associated amyloid fibrils and assuming the same packing densities, the extent of burial should be higher for fibrils assuming the same packing densities. The ΔC_p values for the native, amyloid, and amorphous conformations were -5.6, -5.0, and -3.5 kJ mol^{-1} K^{-1}, respectively (Fig. 7*A* and Table S1). The similar values of ΔC_p upon protein folding and amyloid formation suggest a similar overall burial of surfaces in the two forms. I consider that the tightly packed core regions, as observed in amyloid microcrystals (92, 139), coexist with the less densely packed noncore regions with cavities accessible to bulk water (32), leading to an overall similar extent of burial of surfaces (102). In contrast, the smaller ΔC_p value of amorphous aggregation suggests looser packing, which is consistent with the absence of notable ordered structures.

Two main effects have been shown to be responsible for the ΔH of protein unfolding: the hydration of the buried hydrophobic and polar groups that become exposed in the unfolded state, and the disruption of internal interactions such as van der Waals interactions, and H-bonds (108, 148). The magnitude of the ΔH of amyloid fibrils (normalized by protein concentration) was significantly less than that of the

folding of native β2m (Fig. 7 and Table S1). The Δ*H* values for amorphous aggregation were even smaller in intensity. From the observed similarity of the ΔC_p values, I assumed a similar contribution of the hydration of the buried groups between native and fibril conformations. Therefore, the observed decrease in Δ*H* appeared to be the result of different internal interactions. It is generally accepted that there is a stronger and more persistent backbone H-bond network in the amyloid structure than there is in the globular fold of proteins, leading to an increase in the β-sheet content (32, 91, 102). However, H-bonds should increase the magnitude of the Δ*H* value, which is inconsistent with the results.

Thus, a reasonable explanation for the Δ*H* order in magnitude of "native structure > amyloid fibril > amorphous aggregate" is that it dominantly represents side chain packing in folded or misfolded structures (Fig. 7*B*). The overall side chain packing in the amyloid form cannot be as optimal as that in the native state because the structure is determined by extensively H-bonded β-structured backbones (101, 102). The loss of tight packing may be more serious for amorphous aggregation.

The separation of overall stability of amyloid fibrils (Δ*G*) into the Δ*H* and *T*Δ*S* terms illustrates that the contributions of the two terms vary depending on temperature. Fibrillation is determined by the favorable entropic term at approximately 20 ºC at which Δ*H* is close to zero. Δ*G* is minimal at approximately 35 ºC, at which the fibrils exhibit maximal stability and, thus, Δ*S* is zero because $\Delta S = \partial \Delta G / \partial T$. Fibrillation is then determined by the favorable enthalpy term at 35 ºC. Thus, the temperature dependent enthalpy-entropy interplay determines the stability of amyloid fibrils. To understand this interplay, I have to estimate amyloid-specific factors such as the entropy loss resulting from a rigid H-bonding of backbones and a reduction in the number of monomers as well as the enthalpy gain obtained from numerous molecular contacts.

In conclusion, I showed that quantitative calorimetric analysis with ITC was indeed possible for the supersaturation-limited amyloid fibrillations. Stirring inside the ITC cell can break persistent supersaturation, which triggers fibrillation. Compared with the single crystals of substances, amyloid fibrils retain a thin and linear morphology. Moreover, the shear forces of stirring keep fibrils dispersed in solution and fragment fibrils, which accelerate seed-dependent propagation. These enabled accurate calorimetric measurements of the amyloid burst, making the thermodynamic characterization of fibrillation possible. By carefully adjusting these conditions, I can also monitor the heat of amorphous

aggregation. Accordingly, ITC will become a promising approach for clarifying the thermodynamic properties of protein aggregates.

3-5. Supporting Information

Supplemental Experimental Procedures

Proteins and reagents. Recombinant human β2m protein with an additional methionine residue at the N terminus was expressed in *Escherichia coli* and purified as previously reported (167). The concentration of β2m was determined by measuring absorbance using a molar extinction coefficient of 19,300 M^{-1} cm^{-1} at 280 nm (167). Thioflavin T (ThT) was purchased from Wako Pure Chemical Industries Ltd. (Osaka, Japan). All other reagents were obtained from Nacalai Tesque (Kyoto, Japan).

Fluorescence assay. The formation of β2m fibrils was observed by a fluorometric assay with ThT at 37 °C. Excitation and emission wavelengths were 445 and 485 nm, respectively. Five μl aliquots were taken from the ITC cell after incubation and mixed with 1.0 ml of 5 μM ThT in 50 mM glycine-NaOH buffer (pH 8.5). The individual intensities of ThT fluorescence were normalized using the intensities of 6.7 mg ml^{-1} β2m (Fig. 2*A*), at ~12 h (Fig. 4*A*) or 34 °C (Fig. 5*C*). ThT fluorescence spectra were measured using a F4500 fluorescence spectrophotometer (Hitachi, Japan).

Circular dichroism spectroscopy. Far-UV CD spectra of β2m before and after incubation in the ITC instrument were measured with a J-820 spectropolarimeter (Jasco, Japan) using a cell with a light path of 1 mm. Sample solutions contained 0.1 mg ml^{-1} β2m in 10 mM HCl (pH 2.5) and 100 mM NaCl. CD signals between 195 and 250 nm were expressed as the mean residue ellipticity [θ] (deg cm^2 $dmol^{-1}$). Temperature regulation was performed using a PTC-423L Peltier-unit (Jasco, Japan).

Atomic force microscopy. AFM images were obtained using a Digital Instruments Nanoscope IIIa scanning microscope (Veeco, Santa. Barbara, CA). A 10 μl sample solution of 10 μM β2m was spotted onto freshly cleaved mica and left on the surface for 1 min. The surface was washed twice with 20 μl water and then dried with compressed air. The scanning tip was a Si microcantilever and the scan rate was 1.0 Hz. The average height of the fibrils was estimated based on the peak height values measured.

Enzyme-linked immunosorbent assay to determine the *r*emaining monomer concentrations. According to a model of the supersaturation-dependent formation of fibrils, the remaining monomer concentration after the formation of fibrils is equal to the equilibrium monomer concentration (i.e. critical concentration). This is also true for the formation of amorphous aggregates. In order to quantify the amount of residual *β2m* monomers after *the* formation of amyloid fibrils or amorphous aggregates, immunosorbent analyses using a commercial immunoassay kit (Human β2m ELISA test; MD Bioproducts, North America) were conducted using aggregates produced in ITC as described above. Supernatants of the sample solutions after centrifugation at 40,000 rpm with a CS 120GX ultracentrifuge (Hitachi, Tokyo, Japan) for 30 m at the same temperature as the formation of aggregates were recovered and used for the ELISA assay. A series of diluted samples of the supernatants were assayed using standard β2m solutions as references. The standard solutions confirmed a sensitive and quasi-linear concentration dependence in the 0–200 ng ml^{-1} range.

Supplemental Figures

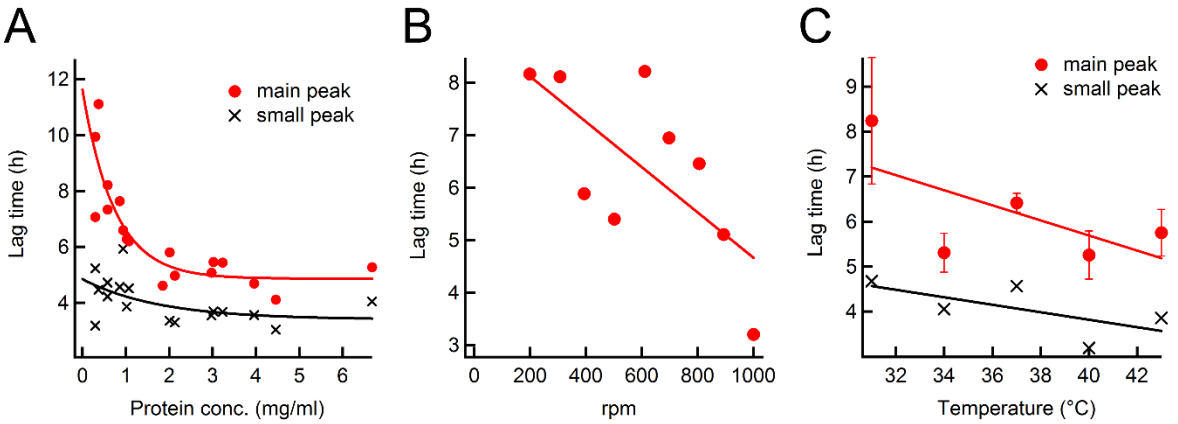

Fig. S1. Dependencies of the observed lag time of heat peaks on the protein concentration or stirring speed at pH 2.5 and 37 °C. (*A*) The lag times of the main and small heat peaks shown in Fig. 2 were plotted against the protein concentration. (*B*) The lag time for the major heat peak observed at 0.5 mg ml^{-1} as shown in Fig. 3 was plotted against the stirring speed. (*C*) The lag times of the main and small heat peaks at 1.1 mg ml^{-1} β2m and 600 rpm at various temperatures shown in Fig. 6 were plotted against the temperature. Solid lines were drawn to guide the eye. It is noted that the lag times indicate the period from the start of heat monitoring (i.e., time zero in the ITC thermogram) and the time of the amyloid burst.

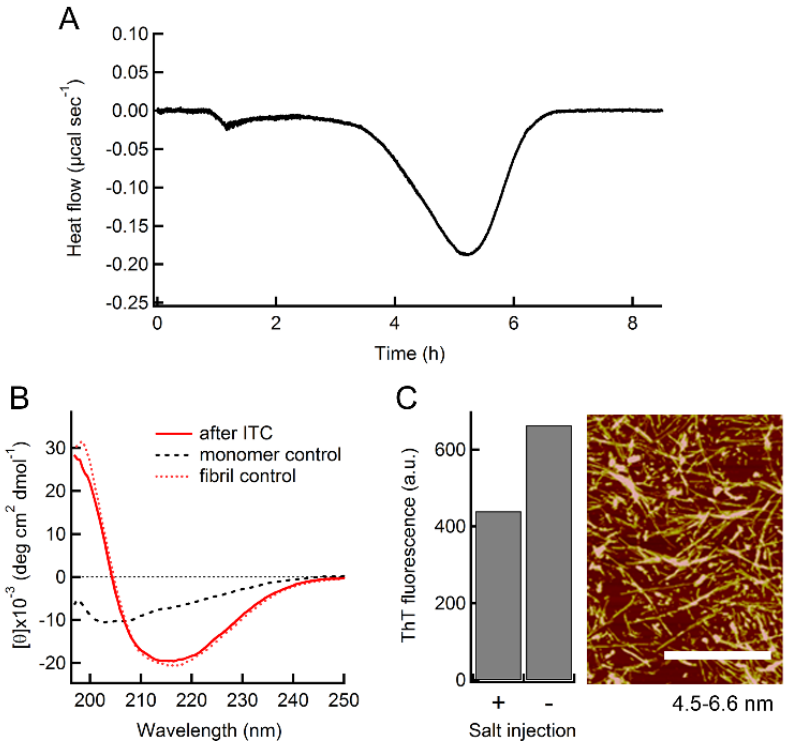

Fig. S2. Amyloid burst of supersaturated β2m prepared outside the ITC cell and then monitored by ITC. (*A*) Thermogram of fibril formation at 0.5 mg ml^{-1}, 0.1 M NaCl, and 37 °C. The stirring speed was 600 rpm. The lag time was 3.7 h with a dead time of 55 min, where the dead time refers to a time between the sample preparation outside the ITC cell and the setup inside the cell with stabilization of the heat capacity signal. The ΔH value of the major peak was 79.8 kJ mol^{-1}. (*B, C*) Characterization of the β2m solution after the heat burst by the far-UV CD (*B*), and ThT fluorescence and AFM (*C*). The normalized ThT intensity after incubation in the ITC cell with (+) and without (-) salt injections is shown. The scale bar on the AFM image indicates 1 μm and the numbers under images are fibril height.

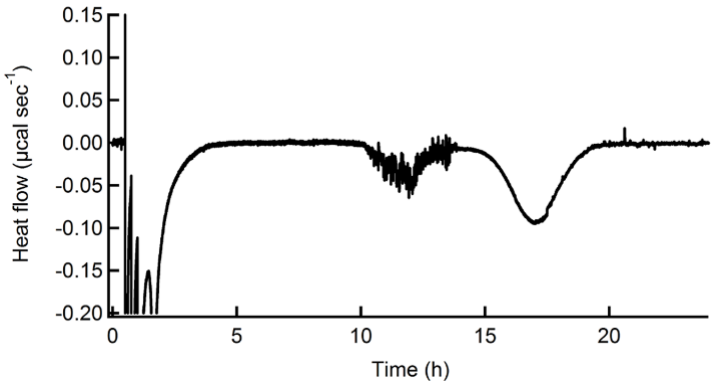

Fig. S3. Thermogram for the formation of amyloid fibrils in the presence of 5 mM sodium sulfate at 37°C. 1.4 ml of β2m at 1.0 mg ml^{-1} was titrated with 300 mM $(NH_4)_2SO_4$ by nine titrations in total with the final concentration of 3 mM. Total heat effects including the peaks at 12 and 17 h were 38.5 kJ mol^{-1}. The value was smaller than the value obtained for the titration with NaCl.

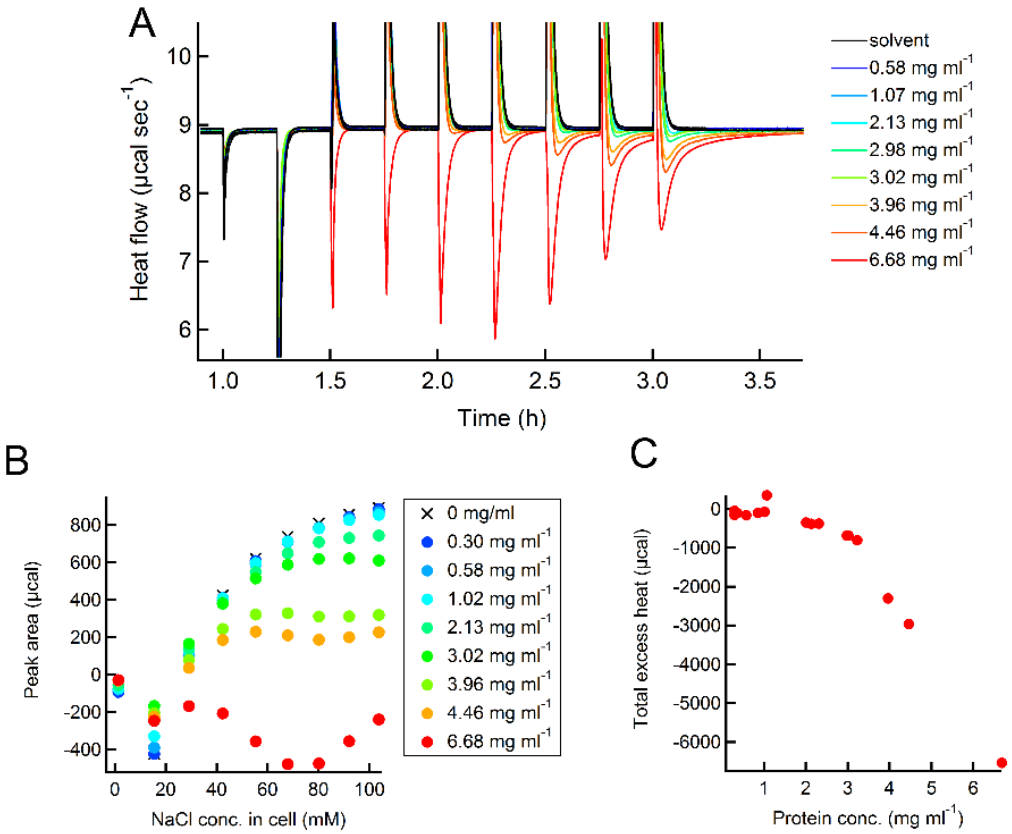

Fig. S4. Amorphous aggregation immediately after the salt titration. (*A*) Expanded thermograms for injection of NaCl at various β2m concentrations. The data are the same as shown in Fig. 1*A*. (*B*) Dependences of the observed heat on the NaCl concentration at various β2m concentrations. Crosses are the observed heat for a reference titration in the absence of protein, representing the heat effects of buffer dilution. (*C*) Dependence on the β2m concentration of the total excess heat where the difference between the peak areas in the presence and absence of β2m were summed up to 0.1 M NaCl. It is noted that the excess heats were not normalized by the β2m concentration. I consider that the excess heats arise from the transient formation of amorphous aggregates (see the text).

SupplementalTables

Table S1. Enthalpy and heat capacity changes with the folding and misfolding of β2m at various temperatures.

Temperature (°C)	$\Delta H_{folding}$* (kJ mol^{-1})	$\Delta H_{amyloid}$ (kJ mol^{-1})		$\Delta H_{amorphous}$ (kJ mol^{-1})
		seeded fibrillation*	spontaneous fibrillation	
31	-142.6	-85.1	-41.3 ± 3.3	-19.8
34	-159.4	-96.7	-56.9 ± 2.2	-27.5
37	-176.3	-119.2	-73.6 ± 5.8	-42.8
40	-193.1	-123.2	-86.0 ± 6.0	-49.6
43	-210.0	-145.2	-101.1 ± 3.9	-68.8
ΔC_p (kJ mol^{-1} K^{-1})	-5.6 ± 0.4	-4.8 ± 0.2	-5.0 ± 0.2	-3.5 ± 0.4

*Data taken from previous study (105).

Table S2. Thermodynamic parameters of the folding and misfolding of β2m obtained by the ELISA assay.

	Temp. (°C)	$[M]_e$* (nM)	K** (μM^{-1})	ΔG_{app}** (kJ mol^{-1})	$-T\Delta S$** (kJ mol^{-1})	ΔH** (kJ mol^{-1})
Amyloid fibrils	31	37.7	26.5	-43.2	-1.9	-41.3 ± 3.3
	37	25.8	38.8	-45.0	28.6	-73.6 ± 5.8
	40	2.4	421.4	-51.7	34.3	-86.0 ± 6.0
	37	15.5 (42.4 μM)	64.5	-46.3	27.7	-74
Amorphous aggregates	31	19.3	51.8	-44.9	-25.1	-19.8
	37	21.4	46.8	-45.5	-2.7	-42.8
	40	17.3	57.8	-46.5	3.1	-49.6
	37	22.7 (42.4 μM)	44.0	-45.4	-2.6	-42.8
	37	29.3 (169.5 μM)	34.1	-44.7	-1.9	-42.8

*The concentrations of the residual monomers determined by the ELISA assay. The initial concentration was 84.7 μM (1.0 mg ml^{-1}), except for those indicated in parentheses.

**The values of K and ΔG_{app} were determined from experimentally determined $[M]_e$ using the relationship: $K = 1/[M]_e$ and $\Delta G_{app} = -RT\ln K$ (see text). The values of $-T\Delta S$ were determined by $\Delta G_{app} = \Delta H - T\Delta S$. ΔH values were obtained directly by ITC (see Table S1).

Chapter 4. General conclusion

I address the general thermodynamic property of amyloid fibrils together with its biological implication and kinetic control based on in-depth examination on thermal stability of various amyloid fibrils. All fibrils examined here showed heat denaturation, which might be caused by increased chain flexibility as shown in thermal unfolding of globular proteins. Interestingly, only α-synuclein amyloid fibrils underwent cold denaturation in the range of 0-20 ºC. Comparison of thermodynamic properties (i.e. positive enthalpy and heat capacity changes) with structural parameters indicate that burial of charged residues to fibril cores is responsible for the cold-denaturation of α-synuclein fibrils.

Therefore, as a general property of soluble and insoluble states of proteins, I speculate that amyloid fibrils of intrinsically disordered proteins which solubility is higher than that of globular proteins due to a large portion of charges and low hydrophobicity might show higher tendency of cold denaturation than other amyloid fibrils formed by globular proteins. In addition, cold denaturation of αSN amyloid fibrils suggested important biological implications including the disaggregation and clearance of protein aggregates. For instance, protein homeostasis of αSN should be better kept than that of at least Aβ, β2m, and insulin. Repeating a cycle of heating and cooling revealed adaptation of amyloid fibrils to cold denaturation, implying smart kinetic controls of amyloid fibrillation in response to changes in ambient conditions. Interestingly, chemical denaturant-assisted cold denaturation of amyloid fibrils demonstrated that cold denaturation of amyloid fibrils is a general thermodynamic property of amyloid fibrils as in the case of globular proteins.

I suggest that although main-chain dominated amyloid fibrillation overwhelms unfavorable burials of charged side-chains to fibril cores, reinforced electrostatic repulsion at low temperature results in promoting cold-denaturation, revealing a unique but general thermodynamic property of amyloid fibrils. A whole picture of thermal stability of amyloid fibrils with the mechanism of cold and heat denaturation is the first example in the field of protein science and biophysics.

In order to obtain further insights into the thermodynamic property of protein aggregation, I performed that ITC-based thermodynamic characterization of amyloid fibrillation and amorphous aggregation is possible by observing directly heat of aggregation. I established the ITC method for observation of heat of seeded and supersaturation-limited spontaneous β2m fibrillation, which was

induced by stirring of ITC, and of amorphous aggregation of β2m at highly condensed salt solution. Precisely observed reaction heat allowed me to produce ΔH. Comparison of ΔH values of native structures, amyloid fibrils, and amorphous aggregates of β2m further gave me valuable information on distinct packing states of each individual β2m structure. ITC analyses in combination to ELISA assay produced a series of thermodynamic parameters, ΔH, ΔS, ΔG, and ΔC_p.

The stability curve of the amyloid fibril and amorphous aggregate of β2m was constructed, demonstrating that the thermodynamic study of protein misfolding and aggregations is indeed possible with just like globular proteins. Toward establishment of thermodynamics of protein misfolding and aggregation, much more case studies should be done and analyzed although I have recently succeeded in observing heat of amyloid formation of $A\beta_{1\text{-}40}$, insulin, and glucagon (data not shown).

I propose that ITC can be used for an assay of amyloid fibrillation and a new method for discovering of effectors for amyloid formation. Finally, I address one more key finding of thermodynamics of protein misfolding and aggregation. Interestingly, the positive sign of ΔC_p of fibril formation of αSN was obtained, which is an opposite sign of ΔC_p for protein folding. I speculate that a distinct sign of ΔC_p may be a unique thermodynamic property of the main-chain-dominated protein misfolding and aggregation which is distinguished from that of side-chain dominated reaction of protein folding. Accordingly, I emphasize that the thermodynamic properties established in protein folding is not always applicable to protein misfolding and aggregation.

References

1. Sipe JD, *et al.* (2012) Amyloid fibril protein nomenclature: 2012 recommendations from the Nomenclature Committee of the International Society of Amyloidosis. *Amyloid* 19(4):167-170.
2. International Asd (2015) The global impact of dementia. *World Alzheimer report*.
3. Jack CR, Jr., *et al.* (2013) Tracking pathophysiological processes in Alzheimer's disease: an updated hypothetical model of dynamic biomarkers. *Lancet Neurol* 12(2):207-216.
4. Zhao LN, Long H, Mu Y, & Chew LY (2012) The toxicity of amyloid beta oligomers. *Int J Mol Sci* 13(6):7303-7327.
5. Prelli F, Castano E, Glenner GG, & Frangione B (1988) Differences between vascular and plaque core amyloid in Alzheimer's disease. *J Neurochem* 51(2):648-651.
6. Shankar GM, *et al.* (2008) Amyloid-beta protein dimers isolated directly from Alzheimer's brains impair synaptic plasticity and memory. *Nat Med* 14(8):837-842.
7. Yang M & Teplow DB (2008) Amyloid beta-protein monomer folding: free-energy surfaces reveal alloform-specific differences. *J Mol Biol* 384(2):450-464.
8. Granata D, *et al.* (2015) The inverted free energy landscape of an intrinsically disordered peptide by simulations and experiments. *Sci Rep* 5:15449.
9. Luhrs T, *et al.* (2005) 3D structure of Alzheimer's amyloid-β(1-42) fibrils. *Proc Natl Acad Sci USA* 102(48):17342-17347.
10. Paravastu AK, Leapman RD, Yau WM, & Tycko R (2008) Molecular structural basis for polymorphism in Alzheimer's β-amyloid fibrils. *Proc Natl Acad Sci USA* 105(47):18349-18354.
11. Zirah S, *et al.* (2006) Structural changes of region 1-16 of the Alzheimer disease amyloid beta-peptide upon zinc binding and in vitro aging. *J Biol Chem* 281(4):2151-2161.
12. Parker MH, *et al.* (2002) Synthesis of (-)-5,8-dihydroxy-3R-methyl-2R-(dipropylamino)-1,2,3,4-tetrahydronaphthalene: an inhibitor of beta-amyloid(1-42) aggregation. *Bioorg Med Chem* 10(11):3565-3569.
13. Lashuel HA, *et al.* (2002) New class of inhibitors of amyloid-beta fibril formation. Implications for the mechanism of pathogenesis in Alzheimer's disease. *J Biol Chem* 277(45):42881-42890.
14. Bellani S, *et al.* (2010) The regulation of synaptic function by alpha-synuclein. *Commun Integr Biol* 3(2):106-109.
15. Spillantini MG, *et al.* (1997) Alpha-synuclein in Lewy bodies. *Nature* 388(6645):839-840.
16. Cookson MR (2005) The biochemistry of Parkinson's disease. *Annu Rev Biochem* 74:29-52.
17. Lansbury PT & Lashuel HA (2006) A century-old debate on protein aggregation and neurodegeneration enters the clinic. *Nature* 443(7113):774-779.
18. Goedert M (2001) Alpha-synuclein and neurodegenerative diseases. *Nat Rev Neurosci* 2(7):492-501.
19. Moore DJ, West AB, Dawson VL, & Dawson TM (2005) Molecular pathophysiology of Parkinson's disease. *Annu Rev Neurosci* 28:57-87.
20. Perrin RJ, Woods WS, Clayton DF, & George JM (2000) Interaction of human alpha-Synuclein

and Parkinson's disease variants with phospholipids. Structural analysis using site-directed mutagenesis. *J Biol Chem* 275(44):34393-34398.

21. Ulmer TS, Bax A, Cole NB, & Nussbaum RL (2005) Structure and dynamics of micelle-bound human alpha-synuclein. *J Biol Chem* 280(10):9595-9603.
22. Ohhashi Y, *et al.* (2002) The intrachain disulfide bond of beta(2)-microglobulin is not essential for the immunoglobulin fold at neutral pH, but is essential for amyloid fibril formation at acidic pH. *J Biochem* 131(1):45-52.
23. McParland VJ, Kalverda AP, Homans SW, & Radford SE (2002) Structural properties of an amyloid precursor of beta(2)-microglobulin. *Nat Struct Biol* 9(5):326-331.
24. Kad NM, Thomson NH, Smith DP, Smith DA, & Radford SE (2001) Beta(2)-microglobulin and its deamidated variant, N17D form amyloid fibrils with a range of morphologies in vitro. *J Mol Biol* 313(3):559-571.
25. Kozhukh GV, *et al.* (2002) Investigation of a peptide responsible for amyloid fibril formation of beta 2-microglobulin by achromobacter protease I. *J Biol Chem* 277(2):1310-1315.
26. Ciryam P, Kundra R, Morimoto RI, Dobson CM, & Vendruscolo M (2015) Supersaturation is a major driving force for protein aggregation in neurodegenerative diseases. *Trends Pharmacol Sci* 36(2):72-77.
27. Knowles TP, Vendruscolo M, & Dobson CM (2014) The amyloid state and its association with protein misfolding diseases. *Nat Rev Mol Cell Biol* 15(6):384-396.
28. Kim YE, Hipp MS, Bracher A, Hayer-Hartl M, & Hartl FU (2013) Molecular chaperone functions in protein folding and proteostasis. *Annu Rev Biochem* 82:323-355.
29. Hipp MS, Park SH, & Hartl FU (2014) Proteostasis impairment in protein-misfolding and -aggregation diseases. *Trends Cell Biol* 24(9):506-514.
30. Gragerov A, *et al.* (1992) Cooperation of GroEL/GroES and DnaK/DnaJ heat shock proteins in preventing protein misfolding in Escherichia coli. *Proc Natl Acad Sci USA* 89(21):10341-10344.
31. Rutherford SL & Lindquist S (1998) Hsp90 as a capacitor for morphological evolution. *Nature* 396(6709):336-342.
32. Hoshino M, *et al.* (2002) Mapping the core of the β_2-microglobulin amyloid fibril by H/D exchange. *Nat Struct Biol* 9(5):332-336.
33. Vendruscolo M & Dobson CM (2013) Structural biology: Protein self-assembly intermediates. *Nat Chem Biol* 9(4):216-217.
34. Kelly JW (1998) The alternative conformations of amyloidogenic proteins and their multi-step assembly pathways. *Curr Opin Struct Biol* 8(1):101-106.
35. Naiki H, *et al.* (1997) Establishment of a kinetic model of dialysis-related amyloid fibril extension *in vitro*. *Amyloid* 4:223-232.
36. Haass C & Selkoe DJ (2007) Soluble protein oligomers in neurodegeneration: lessons from the Alzheimer's amyloid beta-peptide. *Nat Rev Mol Cell Biol* 8(2):101-112.
37. Westermark P, *et al.* (1987) Amyloid fibrils in human insulinoma and islets of Langerhans of

the diabetic cat are derived from a neuropeptide-like protein also present in normal islet cells. *Proc Natl Acad Sci USA* 84(11):3881-3885.

38. Chiti F & Dobson CM (2009) Amyloid formation by globular proteins under native conditions. *Nat Chem Biol* 5(1):15-22.
39. Park SH, *et al.* (2013) PolyQ proteins interfere with nuclear degradation of cytosolic proteins by sequestering the Sis1p chaperone. *Cell* 154(1):134-145.
40. Chacinska A, Koehler CM, Milenkovic D, Lithgow T, & Pfanner N (2009) Importing mitochondrial proteins: machineries and mechanisms. *Cell* 138(4):628-644.
41. Levin A, *et al.* (2014) Ostwald's rule of stages governs structural transitions and morphology of dipeptide supramolecular polymers. *Nature communications* 5:5219.
42. Kahlweit M (1975) Ostwald Ripening of Precipitates. *Adv Colloid Interfac* 5(1):1-35.
43. Lifshitz IM & Slyozov VV (1961) The Kinetics of Precipitation from Supersaturated Solid Solutions. *J Phys Chem Solids* 19(1-2):35-50.
44. Yang HG & Zeng HC (2004) Preparation of hollow anatase TiO2 nanospheres via Ostwald ripening. *Journal of Physical Chemistry B* 108(11):3492-3495.
45. Cremades N, *et al.* (2012) Direct observation of the interconversion of normal and toxic forms of α-synuclein. *Cell* 149(5):1048-1059.
46. Lin Y, Protter DS, Rosen MK, & Parker R (2015) Formation and Maturation of Phase-Separated Liquid Droplets by RNA-Binding Proteins. *Mol Cell* 60(2):208-219.
47. Molliex A, *et al.* (2015) Phase Separation by Low Complexity Domains Promotes Stress Granule Assembly and Drives Pathological Fibrillization. *Cell* 163(1):123-133.
48. Patel A, *et al.* (2015) A Liquid-to-Solid Phase Transition of the ALS Protein FUS Accelerated by Disease Mutation. *Cell* 162(5):1066-1077.
49. Sunde M & Blake C (1997) The structure of amyloid fibrils by electron microscopy and X-ray diffraction. *Adv Protein Chem* 50:123-159.
50. Nelson R, *et al.* (2005) Structure of the cross-beta spine of amyloid-like fibrils. *Nature* 435(7043):773-778.
51. Knowles TP, *et al.* (2007) Role of intermolecular forces in defining material properties of protein nanofibrils. *Science* 318(5858):1900-1903.
52. Meersman F & Dobson CM (2006) Probing the pressure-temperature stability of amyloid fibrils provides new insights into their molecular properties. *Biochim Biophys Acta* 1764(3):452-460.
53. Knowles TP, *et al.* (2009) An analytical solution to the kinetics of breakable filament assembly. *Science* 326(5959):1533-1537.
54. Cohen SI, Vendruscolo M, Dobson CM, & Knowles TP (2012) From macroscopic measurements to microscopic mechanisms of protein aggregation. *J Mol Biol* 421(2-3):160-171.
55. Tanford C (1968) Protein denaturation. *Adv Protein Chem* 23:121-282.
56. Neurath H, Greenstein JP, Putnam FW, & Erickson JO (1944) The chemistry of protein denaturation. *Chem Rev* 34(2):157-265.

57. Anson ML & Mirsky AE (1932) The Effect of Denaturation on the Viscosity of Protein Systems. *J Gen Physiol* 15(3):341-350.
58. Mirsky AE & Pauling L (1936) On the Structure of Native, Denatured, and Coagulated Proteins. *Proc Natl Acad Sci USA* 22(7):439-447.
59. Sakurai K & Goto Y (2007) Principal component analysis of the pH-dependent conformational transitions of bovine beta-lactoglobulin monitored by heteronuclear NMR. *Proc Natl Acad Sci USA* 104(39):15346-15351.
60. Uversky VN (1999) A multiparametric approach to studies of self-organization of globular proteins. *Biochemistry (Mosc)* 64(3):250-266.
61. Ptitsyn OB (1995) Structures of folding intermediates. *Curr Opin Struct Biol* 5(1):74-78.
62. Ptitsyn OB (1995) Molten globule and protein folding. *Adv Protein Chem* 47:83-229.
63. Privalov PL (1979) Stability of proteins: small globular proteins. *Adv Protein Chem* 33:167-241.
64. Akasaka K, Kitahara R, & Kamatari YO (2013) Exploring the folding energy landscape with pressure. *Arch Biochem Biophys* 531(1-2):110-115.
65. Silva JL, *et al.* (2014) High-pressure chemical biology and biotechnology. *Chem Rev* 114(14):7239-7267.
66. Silva JL, Foguel D, & Royer CA (2001) Pressure provides new insights into protein folding, dynamics and structure. *Trends Biochem Sci* 26(10):612-618.
67. Silva JL & Weber G (1993) Pressure stability of proteins. *Annu Rev Phys Chem* 44:89-113.
68. Privalov PL (1990) Cold denaturation of proteins. *Crit Rev Biochem Mol Biol* 25(4):281-305.
69. Privalov PL & Khechinashvili NN (1974) A thermodynamic approach to the problem of stabilization of globular protein structure: a calorimetric study. *J Mol Biol* 86(3):665-684.
70. Wolynes PG, Onuchic JN, & Thirumalai D (1995) Navigating the folding routes. *Science* 267(5204):1619-1620.
71. Dobson CM, Sali A, & Karplus M (1998) Protein folding: A perspective from theory and experiment. *Angew Chem Int Ed* 37(7):868-893.
72. Vendruscolo M, Paci E, Dobson CM, & Karplus M (2001) Three key residues form a critical contact network in a protein folding transition state. *Nature* 409(6820):641-645.
73. Dinner AR, Sali A, Smith LJ, Dobson CM, & Karplus M (2000) Understanding protein folding via free-energy surfaces from theory and experiment. *Trends Biochem Sci* 25(7):331-339.
74. Vendruscolo M, Paci E, Karplus M, & Dobson CM (2003) Structures and relative free energies of partially folded states of proteins. *Proc Natl Acad Sci USA* 100(25):14817-14821.
75. Granata D, Camilloni C, Vendruscolo M, & Laio A (2013) Characterization of the free-energy landscapes of proteins by NMR-guided metadynamics. *Proc Natl Acad Sci USA* 110(17):6817-6822.
76. Kardos J, *et al.* (2011) Reversible heat-induced dissociation of β2-microglobulin amyloid fibrils. *Biochemistry* 50(15):3211-3220.
77. Narimoto T, *et al.* (2004) Conformational stability of amyloid fibrils of β2-microglobulin

probed by guanidine-hydrochloride-induced unfolding. *FEBS Lett* 576(3):313-319.

78. Tartaglia GG, Pechmann S, Dobson CM, & Vendruscolo M (2007) Life on the edge: a link between gene expression levels and aggregation rates of human proteins. *Trends Biochem Sci* 32(5):204-206.
79. Yoshimura Y, *et al.* (2012) Distinguishing crystal-like amyloid fibrils and glass-like amorphous aggregates from their kinetics of formation. *Proc Natl Acad Sci USA* 109(36):14446-14451.
80. Bartels T, Choi JG, & Selkoe DJ (2011) α-Synuclein occurs physiologically as a helically folded tetramer that resists aggregation. *Nature* 477(7362):107-110.
81. Burre J, *et al.* (2013) Properties of native brain α-synuclein. *Nature* 498(7453):E4-6; discussion E6-7.
82. Chiti F & Dobson CM (2006) Protein misfolding, functional amyloid, and human disease. *Annu Rev Biochem* 75:333-366.
83. Fezoui Y & Teplow DB (2002) Kinetic studies of amyloid β-protein fibril assembly. Differential effects of α-helix stabilization. *J Biol Chem* 277(40):36948-36954.
84. Jarrett JT & Lansbury PT, Jr. (1993) Seeding "one-dimensional crystallization" of amyloid: a pathogenic mechanism in Alzheimer's disease and scrapie? *Cell* 73(6):1055-1058.
85. Kim HY, *et al.* (2009) Structural properties of pore-forming oligomers of α-synuclein. *J Am Chem Soc* 131(47):17482-17489.
86. Kim HY, Cho MK, Riedel D, Fernandez CO, & Zweckstetter M (2008) Dissociation of amyloid fibrils of α-synuclein in supercooled water. *Angew Chem Int Ed* 47(27):5046-5048.
87. Mishra R & Winter R (2008) Cold- and pressure-induced dissociation of protein aggregates and amyloid fibrils. *Angew Chem Int Ed* 47(35):6518-6521.
88. Wetzel R, Shivaprasad S, & Williams AD (2007) Plasticity of amyloid fibrils. *Biochemistry* 46(1):1-10.
89. McGlinchey RP, Gruschus JM, Nagy A, & Lee JC (2011) Probing fibril dissolution of the repeat domain of a functional amyloid, Pmel17, on the microscopic and residue level. *Biochemistry* 50(49):10567-10569.
90. Smith JF, Knowles TPJ, Dobson CM, MacPhee CE, & Welland ME (2006) Characterization of the nanoscale properties of individual amyloid fibrils. *Proc Natl Acad Sci USA* 103(43):15806-15811.
91. Lee YH & Goto Y (2012) Kinetic intermediates of amyloid fibrillation studied by hydrogen exchange methods with nuclear magnetic resonance. *Biochim Biophys Acta* 1824(12):1307-1323.
92. Sawaya MR, *et al.* (2007) Atomic structures of amyloid cross-β spines reveal varied steric zippers. *Nature* 447(7143):453-457.
93. Tycko R (2011) Solid-state NMR studies of amyloid fibril structure. *Annu Rev Phys Chem* 62:279-299.
94. Ma B & Nussinov R (2006) Simulations as analytical tools to understand protein aggregation

and predict amyloid conformation. *Curr Opin Chem Biol* 10(5):445-452.

95. Shammas SL, *et al.* (2011) Perturbation of the stability of amyloid fibrils through alteration of electrostatic interactions. *Biophys J* 100(11):2783-2791.
96. Goldschmidt L, Teng PK, Riek R, & Eisenberg D (2010) Identifying the amylome, proteins capable of forming amyloid-like fibrils. *Proc Natl Acad Sci USA* 107(8):3487-3492.
97. Fandrich M, Fletcher MA, & Dobson CM (2001) Amyloid fibrils from muscle myoglobin. *Nature* 410(6825):165-166.
98. Murciano-Calles J, Cobos ES, Mateo PL, Camara-Artigas A, & Martinez JC (2010) An oligomeric equilibrium intermediate as the precursory nucleus of globular and fibrillar supramacromolecular assemblies in a PDZ domain. *Biophys J* 99(1):263-272.
99. Picotti P, *et al.* (2007) Amyloid fibril formation and disaggregation of fragment 1-29 of apomyoglobin: insights into the effect of pH on protein fibrillogenesis. *J Mol Biol* 367(5):1237-1245.
100. Chatani E & Goto Y (2005) Structural stability of amyloid fibrils of β_2-microglobulin in comparison with its native fold. *BBA Proteins Proteom* 1753(1):64-75.
101. Chatani E, Kato M, Kawai T, Naiki H, & Goto Y (2005) Main-chain dominated amyloid structures demonstrated by the effect of high pressure. *J Mol Biol* 352(4):941-951.
102. Lee YH, Chatani E, Sasahara K, Naiki H, & Goto Y (2009) A comprehensive model for packing and hydration for amyloid fibrils of β_2-microglobulin. *J Biol Chem* 284(4):2169-2175.
103. Qi X, Moore RA, & McGuirl MA (2012) Dissociation of recombinant prion protein fibrils into short protofilaments: implications for the endocytic pathway and involvement of the N-terminal domain. *Biochemistry* 51(22):4600-4608.
104. Izawa Y, *et al.* (2012) Role of C-terminal negative charges and tyrosine residues in fibril formation of α-synuclein. *Brain Behav* 2(5):595-605.
105. Kardos J, Yamamoto K, Hasegawa K, Naiki H, & Goto Y (2004) Direct measurement of the thermodynamic parameters of amyloid formation by isothermal titration calorimetry. *J Biol Chem* 279(53):55308-55314.
106. Yagi H, *et al.* (2010) Isolation of short peptide fragments from α-synuclein fibril core identifies a residue important for fibril nucleation: a possible implication for diagnostic applications. *Biochim Biophys Acta* 1804(10):2077-2087.
107. Lee JH, *et al.* (2009) Real-time analysis of amyloid fibril formation of α-synuclein using a fibrillation-state-specific fluorescent probe of JC-1. *Biochem J* 418:311-323.
108. Privalov PL (2007) Thermodynamic problems in structural molecular biology. *Pure and Applied Chemistry* 79(8):1445-1462.
109. Myers JK, Pace CN, & Scholtz JM (1995) Denaturant m values and heat capacity changes: relation to changes in accessible surface areas of protein unfolding. *Protein Sci* 4(10):2138-2148.
110. Baldwin AJ, *et al.* (2011) Metastability of native proteins and the phenomenon of amyloid formation. *J Am Chem Soc* 133(36):14160-14163.

111. Kumar S & Nussinov R (2004) Different roles of electrostatics in heat and in cold: adaptation by citrate synthase. *ChemBioChem* 5(3):280-290.
112. Dias CL, *et al.* (2010) The hydrophobic effect and its role in cold denaturation. *Cryobiology* 60(1):91-99.
113. Measey TJ & Gai F (2012) Light-triggered disassembly of amyloid fibrils. *Langmuir* 28(34):12588-12592.
114. Dill KA, Ozkan SB, Shell MS, & Weikl TR (2008) The protein folding problem. *Annu Rev Biophys* 37:289-316.
115. Kumar S & Nussinov R (2002) Close-range electrostatic interactions in proteins. *ChemBioChem* 3(7):604-617.
116. Prabhu NV & Sharp KA (2005) Heat capacity in proteins. *Annu Rev Phys Chem* 56:521-548.
117. Chen SH, Suzuki CK, & Wu SH (2008) Thermodynamic characterization of specific interactions between the human Lon protease and G-quartet DNA. *Nucleic Acids Res* 36(4):1273-1287.
118. Robblee JP, Cao W, Henn A, Hannemann DE, & De La Cruz EM (2005) Thermodynamics of nucleotide binding to actomyosin V and VI: a positive heat capacity change accompanies strong ADP binding. *Biochemistry* 44(30):10238-10249.
119. Reshetnyak YK, Andreev OA, Segala M, Markin VS, & Engelman DM (2008) Energetics of peptide (pHLIP) binding to and folding across a lipid bilayer membrane. *Proc Natl Acad Sci USA* 105(40):15340-15345.
120. Boncina M, Lah J, Rescic J, & Vlachy V (2010) Thermodynamics of the lysozyme-salt interaction from calorimetric titrations. *J Phys Chem B* 114(12):4313-4319.
121. Matulis D, Rouzina I, & Bloomfield VA (2002) Thermodynamics of cationic lipid binding to DNA and DNA condensation: roles of electrostatics and hydrophobicity. *J Am Chem Soc* 124(25):7331-7342.
122. Jeppesen MD, Hein K, Nissen P, Westh P, & Otzen DE (2010) A thermodynamic analysis of fibrillar polymorphism. *Biophys Chem* 149(1-2):40-46.
123. Kyte J & Doolittle RF (1982) A simple method for displaying the hydropathic character of a protein. *J Mol Biol* 157(1):105-132.
124. Magnan CN, Randall A, & Baldi P (2009) SOLpro: accurate sequence-based prediction of protein solubility. *Bioinformatics* 25(17):2200-2207.
125. Doering DS & Matsudaira P (1996) Cysteine scanning mutagenesis at 40 of 76 positions in villin headpiece maps the F-actin binding site and structural features of the domain. *Biochemistry* 35(39):12677-12685.
126. Del Mar C, Greenbaum EA, Mayne L, Englander SW, & Woods VL, Jr. (2005) Structure and properties of α-synuclein and other amyloids determined at the amino acid level. *Proc Natl Acad Sci USA* 102(43):15477-15482.
127. Vilar M, *et al.* (2008) The fold of α-synuclein fibrils. *Proc Natl Acad Sci USA* 105(25):8637-

8642.

128. Qin Z, Hu D, Han S, Hong DP, & Fink AL (2007) Role of different regions of α-synuclein in the assembly of fibrils. *Biochemistry* 46(46):13322-13330.
129. Heise H, *et al.* (2005) Molecular-level secondary structure, polymorphism, and dynamics of full-length α-synuclein fibrils studied by solid-state NMR. *Proc Natl Acad Sci USA* 102(44):15871-15876.
130. Ami D, *et al.* (2012) Structure, stability, and aggregation of beta-2 microglobulin mutants: insights from a Fourier transform infrared study in solution and in the crystalline state. *Biophys J* 102(7):1676-1684.
131. Comellas G, *et al.* (2011) Structured regions of α-synuclein fibrils include the early-onset Parkinson's disease mutation sites. *J Mol Biol* 411(4):881-895.
132. Lemkau LR, *et al.* (2012) Mutant protein A30P α-synuclein adopts wild-type fibril structure, despite slower fibrillation kinetics. *J Biol Chem* 287(14):11526-11532.
133. Chen M, Margittai M, Chen J, & Langen R (2007) Investigation of α-synuclein fibril structure by site-directed spin labeling. *J Biol Chem* 282(34):24970-24979.
134. Debelouchina GT, Platt GW, Bayro MJ, Radford SE, & Griffin RG (2010) Magic angle spinning NMR analysis of β2-microglobulin amyloid fibrils in two distinct morphologies. *J Am Chem Soc* 132(30):10414-10423.
135. Yamaguchi K, *et al.* (2004) Core and heterogeneity of β2-microglobulin amyloid fibrils as revealed by H/D exchange. *J Mol Biol* 338(3):559-571.
136. Iwata K, *et al.* (2006) 3D structure of amyloid protofilaments of β2-microglobulin fragment probed by solid-state NMR. *Proc Natl Acad Sci USA* 103(48):18119-18124.
137. Jucker M & Walker LC (2013) Self-propagation of pathogenic protein aggregates in neurodegenerative diseases. *Nature* 501(7465):45-51.
138. Bemporad F & Chiti F (2012) Protein misfolded oligomers: experimental approaches, mechanism of formation, and structure-toxicity relationships. *Chem Biol* 19(3):315-327.
139. Eisenberg D & Jucker M (2012) The amyloid state of proteins in human diseases. *Cell* 148(6):1188-1203.
140. Tycko R & Wickner RB (2013) Molecular structures of amyloid and prion fibrils: consensus versus controversy. *Acc Chem Res* 46(7):1487-1496.
141. Laganowsky A, *et al.* (2012) Atomic view of a toxic amyloid small oligomer. *Science* 335(6073):1228-1231.
142. Fandrich M & Dobson CM (2002) The behaviour of polyamino acids reveals an inverse side chain effect in amyloid structure formation. *EMBO J* 21(21):5682-5690.
143. Wetzel R (2006) Kinetics and thermodynamics of amyloid fibril assembly. *Accounts Chem Res* 39(9):671-679.
144. Morris AM, Watzky MA, & Finke RG (2009) Protein aggregation kinetics, mechanism, and curve-fitting: a review of the literature. *Biochim Biophys Acta* 1794(3):375-397.

145. Kitayama H, *et al.* (2013) A common mechanism underlying amyloid fibrillation and protein crystallization revealed by the effects of ultrasonication. *Biochim Biophys Acta* 1834(12):2640-2646.
146. Lin Y, Lee YH, Yoshimura Y, Yagi H, & Goto Y (2013) Solubility and Supersaturation-Dependent Protein Misfolding Revealed by Ultrasonication. *Langmuir* 30(7):1845-1854.
147. Ciryam P, Tartaglia GG, Morimoto RI, Dobson CM, & Vendruscolo M (2013) Widespread aggregation and neurodegenerative diseases are associated with supersaturated proteins. *Cell reports* 5(3):781-790.
148. Makhatadze GI & Privalov PL (1995) Energetics of protein structure. *Adv Protein Chem* 47:307-425.
149. Leavitt S & Freire E (2001) Direct measurement of protein binding energetics by isothermal titration calorimetry. *Curr Opin Struct Biol* 11(5):560-566.
150. Ladbury JE & Williams MA (2004) The extended interface: measuring non-local effects in biomolecular interactions. *Curr Opin Struct Biol* 14(5):562-569.
151. Vermeer AW & Norde W (2000) The thermal stability of immunoglobulin: unfolding and aggregation of a multi-domain protein. *Biophys J* 78(1):394-404.
152. Benjwal S, Verma S, Rohm KH, & Gursky O (2006) Monitoring protein aggregation during thermal unfolding in circular dichroism experiments. *Protein Sci* 15(3):635-639.
153. Dzwolak W, Ravindra R, Lendermann J, & Winter R (2003) Aggregation of bovine insulin probed by DSC/PPC calorimetry and FTIR spectroscopy. *Biochemistry* 42(38):11347-11355.
154. Sasahara K, Naiki H, & Goto Y (2005) Kinetically controlled thermal response of β_2-microglobulin amyloid fibrils. *J Mol Biol* 352(3):700-711.
155. Sasahara K, Yagi H, Naiki H, & Goto Y (2009) Thermal response with exothermic effects of β_2-microglobulin amyloid fibrils and fibrillation. *J Mol Biol* 389(3):584-594.
156. Morel B, Varela L, & Conejero-Lara F (2010) The thermodynamic stability of amyloid fibrils studied by differential scanning calorimetry. *J Phys Chem B* 114(11):4010-4019.
157. Raman B, *et al.* (2005) Critical balance of electrostatic and hydrophobic interactions is required for β_2-microglobulin amyloid fibril growth and stability. *Biochemistry* 44(4):1288-1299.
158. Kad NM, *et al.* (2003) Hierarchical assembly of β_2-microglobulin amyloid in vitro revealed by atomic force microscopy. *J Mol Biol* 330(4):785-797.
159. Giehm L & Otzen DE (2010) Strategies to increase the reproducibility of protein fibrillization in plate reader assays. *Anal Biochem* 400(2):270-281.
160. Ohhashi Y, Kihara M, Naiki H, & Goto Y (2005) Ultrasonication-induced amyloid fibril formation of β_2-microglobulin. *J Biol Chem* 280(38):32843-32848.
161. Chatani E, *et al.* (2009) Ultrasonication-dependent production and breakdown lead to minimum-sized amyloid fibrils. *Proc Natl Acad Sci USA* 106(27):11119-11124.
162. So M, *et al.* (2011) Ultrasonication-dependent acceleration of amyloid fibril formation. *J Mol Biol* 412(4):568-577.

163. Yoshimura Y, So M, Yagi H, & Goto Y (2013) Ultrasonication: an efficient agitation for accelerating the supersaturation-limited amyloid fibrillation of proteins. *Jpn J Appl Phys* 52:07HA01-01-07HA01-08.
164. Come JH, Fraser PE, & Lansbury PT, Jr. (1993) A kinetic model for amyloid formation in the prion diseases: importance of seeding. *Proc Natl Acad Sci USA* 90(13):5959-5963.
165. Cabriolu R, Kashchiev D, & Auer S (2010) Atomistic theory of amyloid fibril nucleation. *J Chem Phys* 133(22):225101.
166. Durbin SD & Feher G (1996) Protein crystallization. *Annu Rev Phys Chem* 47:171-204.
167. Chiba T, *et al.* (2003) Amyloid fibril formation in the context of full-length protein: effects of proline mutations on the amyloid fibril formation of β_2-microglobulin. *J Biol Chem* 278(47):47016-47024.

List of Publication

1) **Tatsuya Ikenoue**[1], Young-Ho Lee[1], József Kardos, Miyu Saiki, Hisashi Yagi, Yasushi Kawata, Yuji Goto

[1]T. Ikenoue and Y.-H.L. contributed equally to this work.

"Cold Denaturation of Alpha-Synuclein Amyloid Fibrils"

Angew. Chem. Int. Ed., 2014, 53, 7799-7804

Impact factor: 11.261 (2014)

2) **Tatsuya Ikenoue**[1], Young-Ho Lee[1], József Kardos, Hisashi Yagi, Takahisa Ikegami, Hironobu Naiki, Yuji Goto

[1]T. Ikenoue and Y.-H.L. contributed equally to this work.

"Heat of Supersaturation-limited Amyloid Burst Directly Monitored by Isothermal Titration Calorimetry"

Proc. Natl. Acad. Sci. U.S.A., 2014, 111, 6654-6659

Impact factor: 9.674 (2014)

3) Aiko Mizuno, Masatomo So, Miki Hirano, Masayuki Adachi, Yoko Akazawa-Ogawa, Yoshihisa Hagihara, **Tatsuya Ikenoue**, Young-Ho Lee, Yasushi Kawata; Yuji Goto

"Ultrasonication-dependent Formation and Degradation of Alpha-synuclein Amyloid Fibrils"

Biochim. Biophys. Acta., 2015, 1854, 209-217.

Impact factor: 2.747 (2014)